CFD modeling of the heat and mass transfer in a refrigerated truck trailer equipped with eutectic plates

Jihyuk Jeong

▶ **To cite this version:**

Jihyuk Jeong. CFD modeling of the heat and mass transfer in a refrigerated truck trailer equipped with eutectic plates. Thermics [physics.class-ph]. INSA de Lyon; Université de Sherbrooke (Québec, Canada), 2024. English. NNT : 2024ISAL0034 . tel-04819424

HAL Id: tel-04819424

https://theses.hal.science/tel-04819424v1

Submitted on 4 Dec 2024

HAL is a multi-disciplinary open access archive for the deposit and dissemination of scientific research documents, whether they are published or not. The documents may come from teaching and research institutions in France or abroad, or from public or private research centers.

L'archive ouverte pluridisciplinaire **HAL**, est destinée au dépôt et à la diffusion de documents scientifiques de niveau recherche, publiés ou non, émanant des établissements d'enseignement et de recherche français ou étrangers, des laboratoires publics ou privés.

N°d'ordre NNT : 2024ISAL0034

THÈSE de DOCTORAT DE L'INSA LYON, membre de l'UNIVERSITÉ DE LYON

délivré en partenariat international avec
UNIVERSITÉ DE SHERBROOKE

École Doctorale N° 162
MÉCANIQUE, ÉNERGETIQUE, GÉNIE CIVIL, ACOUSTIQUE

Spécialité / discipline de doctorat :
Thermique-Énergétique

Soutenue publiquement, le 24/04/2024 par :
Jihyuk Jeong

Modélisation CFD du transfert de chaleur et de masse dans une remorque de camion réfrigérée équipée de plaques eutectiques

CFD Modeling of the Heat and Mass Transfer in a Refrigerated Truck Trailer Equipped with Eutectic Plates

---

Devant le jury composé de :
FOURNAISON, Laurence, Directrice de Recherche, INRAE, Présidente
SAFDARI SHADLOO, Mostafa, Maître de Conférences HDR, INSA Rouen, Rapporteur
GOSSELIN, Louis, Professeur, Université Laval (Québec), Rapporteur
FERTEL, Camille, Docteure, Tecnea Canada, Examinatrice
MICHEL, Benoît, Maître de Conférences, INSA Lyon, Examinateur
BONJOUR, Jocelyn, Professeur des Universités, INSA Lyon, Directeur de thèse
PONCET, Sébastien, Professeur, Université de Sherbrooke, Co-directeur de thèse

Thèse accessible à l'adresse : https://theses.insa-lyon.fr/publication/2024ISAL0034/these.pdf © [J. Jeong], [2024], INSA Lyon, tous droits réservés

Thèse accessible à l'adresse : https://theses.insa-lyon.fr/publication/2024ISAL0034/these.pdf © [J. Jeong], [2024], INSA Lyon, tous droits réservés

INSTITUT NATIONAL DES SCIENCES APPLIQUÉES LYON

Département de la Formation par la Recherche et des Études Doctorales (**FEDORA**)

Bâtiment INSA direction, 1er étage
37, av. J. Capelle
69621 Villeurbanne Cédex
fedora@insa-lyon.fr

Référence : TH1093_JEONG Jihyuk

L'INSA Lyon a mis en place une procédure de contrôle systématique via un outil de détection de similitudes (logiciel Compilatio). Après le dépôt du manuscrit de thèse, celui-ci est analysé par l'outil. Pour tout taux de similarité supérieur à 10%, le manuscrit est vérifié par l'équipe de FEDORA. Il s'agit notamment d'exclure les auto-citations, à condition qu'elles soient correctement référencées avec citation expresse dans le manuscrit.

Par ce document, il est attesté que ce manuscrit, dans la forme communiquée par la personne doctorante à l'INSA Lyon, satisfait aux exigences de l'Etablissement concernant le taux maximal de similitude admissible.

INSA LYON
Campus LyonTech La Doua
20, avenue Albert Einstein - 69621 Villeurbanne cedex - France
Tél. +33 (0)4 72 43 83 83 - Fax +33 (0)4 72 43 85 00
www.insa-lyon.fr

membre de UNIVERSITÉ DE LYON

Thèse accessible à l'adresse : https://theses.insa-lyon.fr/publication/2024ISAL0034/these.pdf © [J. Jeong], [2024], INSA Lyon, tous droits réservés

Thèse accessible à l'adresse : https://theses.insa-lyon.fr/publication/2024ISAL0034/these.pdf © [J. Jeong], [2024], INSA Lyon, tous droits réservés

Département FEDORA – INSA Lyon - Ecoles Doctorales

SIGLE	ECOLE DOCTORALE	NOM ET COORDONNEES DU RESPONSABLE
ED 206 CHIMIE	**CHIMIE DE LYON** https://www.edchimie-lyon.fr Sec. : Renée EL MELHEM Bât. Blaise PASCAL, 3e étage secretariat@edchimie-lyon.fr	**M. Stéphane DANIELE** C2P2-CPE LYON-UMR 5265 Bâtiment F308, BP 2077 43 Boulevard du 11 novembre 1918 69616 Villeurbanne directeur@edchimie-lyon.fr
ED 341 E2M2	**ÉVOLUTION, ÉCOSYSTÈME, MICROBIOLOGIE, MODÉLISATION** http://e2m2.universite-lyon.fr Sec. : Bénédicte LANZA Bât. Atrium, UCB Lyon 1 Tél : 04.72.44.83.62 secretariat.e2m2@univ-lyon1.fr	**Mme Sandrine CHARLES** Université Claude Bernard Lyon 1 UFR Biosciences Bâtiment Mendel 43, boulevard du 11 Novembre 1918 69622 Villeurbanne CEDEX e2m2.codir@listes.univ-lyon1.fr
ED 205 EDISS	**INTERDISCIPLINAIRE SCIENCES-SANTÉ** http://ediss.universite-lyon.fr Sec. : Bénédicte LANZA Bât. Atrium, UCB Lyon 1 Tél : 04.72.44.83.62 secretariat.ediss@univ-lyon1.fr	**Mme Sylvie RICARD-BLUM** Laboratoire ICBMS - UMR 5246 CNRS - Université Lyon 1 Bâtiment Raulin - 2ème étage Nord 43 Boulevard du 11 novembre 1918 69622 Villeurbanne Cedex Tél : +33(0)4 72 44 82 32 sylvie.ricard-blum@univ-lyon1.fr
ED 34 EDML	**MATÉRIAUX DE LYON** http://ed34.universite-lyon.fr Sec. : Yann DE ORDENANA Tél : 04.72.18.62.44 yann.de-ordenana@ec-lyon.fr	**M. Stéphane BENAYOUN** Ecole Centrale de Lyon Laboratoire LTDS 36 avenue Guy de Collongue 69134 Ecully CEDEX Tél : 04.72.18.64.37 stephane.benayoun@ec-lyon.fr
ED 160 EEA	**ÉLECTRONIQUE, ÉLECTROTECHNIQUE, AUTOMATIQUE** https://edeea.universite-lyon.fr Sec. : Philomène TRECOURT Bâtiment Direction INSA Lyon Tél : 04.72.43.71.70 secretariat.edeea@insa-lyon.fr	**M. Philippe DELACHARTRE** INSA LYON Laboratoire CREATIS Bâtiment Blaise Pascal, 7 avenue Jean Capelle 69621 Villeurbanne CEDEX Tél : 04.72.43.88.63 philippe.delachartre@insa-lyon.fr
ED 512 INFOMATHS	**INFORMATIQUE ET MATHÉMATIQUES** http://edinfomaths.universite-lyon.fr Sec. : Renée EL MELHEM Bât. Blaise PASCAL, 3e étage Tél : 04.72.43.80.46 infomaths@univ-lyon1.fr	**M. Hamamache KHEDDOUCI** Université Claude Bernard Lyon 1 Bât. Nautibus 43, Boulevard du 11 novembre 1918 69 622 Villeurbanne Cedex France Tél : 04.72.44.83.69 direction.infomaths@listes.univ-lyon1.fr
ED 162 MEGA	**MÉCANIQUE, ÉNERGÉTIQUE, GÉNIE CIVIL, ACOUSTIQUE** http://edmega.universite-lyon.fr Sec. : Philomène TRECOURT Tél : 04.72.43.71.70 Bâtiment Direction INSA Lyon mega@insa-lyon.fr	**M. Etienne PARIZET** INSA Lyon Laboratoire LVA Bâtiment St. Exupéry 25 bis av. Jean Capelle 69621 Villeurbanne CEDEX etienne.parizet@insa-lyon.fr
ED 483 ScSo	**ScSo**[1] https://edsciencessociales.universite-lyon.fr Sec. : Mélina FAVETON Tél : 04.78.69.77.79 melina.faveton@univ-lyon2.fr	**M. Bruno MILLY** (INSA : J.Y. TOUSSAINT) Univ. Lyon 2 Campus Berges du Rhône 18, quai Claude Bernard 69365 LYON CEDEX 07 Bureau BEL 319 bruno.milly@univ-lyon2.fr

Thèse ~~accessible à l'adresse : https://theses.in~~sa-lyon.fr/publication/2024ISAL0034/these.pdf © [J. Jeong], [2024], INSA Lyon, tous droits réservés

[1] ScSo : Histoire, Géographie, Aménagement, Urbanisme, Archéologie, Science politique, Sociologie, Anthropologie

Thèse accessible à l'adresse : https://theses.insa-lyon.fr/publication/2024ISAL0034/these.pdf © [J. Jeong], [2024], INSA Lyon, tous droits réservés

Résumé

Le système de refroidissement par plaques eutectiques (matériau à changement de phase, MCP) est une possible alternative aux systèmes conventionnels de réfrigération alimentés par des combustibles fossiles pour le transport de produits alimentaires surgelés ou réfrigérés dans des remorques de camions. Des modèles numériques ont été développés pour évaluer sa faisabilité et ont été validés avec succès par rapport à des résultats numériques et expérimentaux issus de la littérature.

Initialement, un modèle d'infiltration d'air dans la remorque a été développé utilisant un modèle de turbulence $k-\omega$ SST pour prédire le comportement thermoaéraulique de l'air pendant les périodes d'ouverture des portes. Différentes configurations des plaques eutectiques et des ventilateurs ont été analysées. Sans cargaison, les plaques disposées en série le long du plafond de la remorque ont montré un temps de renouvellement plus élevé que celles disposées en parallèle à l'arrière, en raison des zones de recirculation. Cependant, une fois la cargaison introduite, les deux configurations offrent des performances similaires car les zones de recirculation n'ont pas pu se former.

Par ailleurs, un modèle multiphasique granulaire eulérien-eulérien a été développé pour prédire la formation et la croissance du givre sur les plaques eutectiques. Le modèle de turbulence $k-\omega$ SST a été intégré pour étendre l'applicabilité du modèle de givre à une gamme plus large de vitesses d'air. Un modèle de solidification et de fusion a également été implémenté et couplé aux modèles précédents. Avec ce modèle combiné, les performances d'un système eutectique ont été étudiées pour des conditions estivales typiques à Montréal, Canada. Environ 2.3 % du MCP change effectivement de phase au cours des 120 premières secondes. Globalement, le système eutectique offre une alternative viable au système conventionnel, bénéficiant des mécanismes de prévention des infiltrations ou de dégivrage.

Mots-clés : Réfrigération, Matériau à changement de phase, Transfert de chaleur et de masse, Dynamique des fluides numérique.

Thèse accessible à l'adresse : https://theses.insa-lyon.fr/publication/2024ISAL0034/these.pdf © [J. Jeong], [2024], INSA Lyon, tous droits réservés

Thèse accessible à l'adresse : https://theses.insa-lyon.fr/publication/2024ISAL0034/these.pdf © [J. Jeong], [2024], INSA Lyon, tous droits réservés

Abstract

An eutectic refrigeration system is proposed to replace conventional refrigeration systems powered by fossil fuel consumption for transporting frozen food products via refrigerated truck trailers. To study the feasibility of the eutectic system, numerical models have been first developed and favorably validated against published numerical and experimental results. The consolidated model has then been used to accurately predict the performance of the eutectic plates, while being compared to new measurements on a lab scale system.

Initially, an infiltration model was developed using a $k - \omega$ SST turbulence model to predict the thermoaerolic behavior of air during door-opening periods. Two fan modes and different configurations of eutectic plates were analyzed. Without any cargo, plates placed in series along the truck trailer's roof had a higher renewal time than those placed in parallel at the rear due to recirculation zones created by the pre-existing flow. However, as cargo is introduced into the system, both configurations behaved similarly as recirculation zones couldn't form.

Furthermore, a granular multiphase Eulerian-Eulerian model was developed to predict frost formation on top of a cold plate. The $k - \omega$ SST turbulence model was incorporated into the frost model to extend its applicability to a wider range of inlet velocities. Finally, the solidification and melting models were consolidated into the model as a user-defined function (UDF). With the consolidated model, the performance of a eutectic system was studied for typical summer conditions in Montreal, Canada. The analysis showed that approximately 2.3% of the phase change material undergoes a phase change within the first 120 seconds. Overall, the performance of the eutectic system can be considered a viable replacement for the conventional system. Moreover, the system will be greatly enhanced through infiltration prevention and frost removal mechanisms.

Keywords: Refrigeration, Phase Change Materials, Heat and Mass Transfer, Computational Fluid Dynamics.

Thèse accessible à l'adresse : https://theses.insa-lyon.fr/publication/2024ISAL0034/these.pdf © [J. Jeong], [2024], INSA Lyon, tous droits réservés

Thèse accessible à l'adresse : https://theses.insa-lyon.fr/publication/2024ISAL0034/these.pdf © [J. Jeong], [2024], INSA Lyon, tous droits réservés

Acknowledgement

I am immensely grateful to the many individuals and organizations whose unwavering support and guidance have paved the way for my doctoral journey.

First and foremost, I want to express my heartfelt appreciation to my supervisors, Professor Sébastien Poncet and Professor Jocelyn Bonjour. Their expertise, encouragement, and unwavering support have been the foundation of my research efforts. Their insightful feedback, constructive criticism, and infinite patience have greatly influenced the direction and quality of my dissertation.

I would also like to express my gratitude to my dissertation committee member, Dr. Benoit Michel for his invaluable guidance, scholarly insights, and thoughtful critique throughout the various stages of my research. Additionally, I would like to express my gratitude to Professor Hachimi Fellouah for his guidance during my experiments.

This project has been funded by the NSERC chair on industrial energy efficiency, established in 2019 at Université de Sherbrooke, with the support of Hydro-Québec (laboratoire des technologies de l'énergie), Natural Resources Canada (CanmetEnergy-Varennes) and Copeland Canada Inc. All calculations have been done using the HPC facilities of the Digital Research Alliance of Canada. They are all here grateful acknowledged.

I extend my deepest gratitude to my family for their unwavering love, unshakeable belief in my abilities, and constant encouragement during this challenging journey. Their sacrifices and unwavering support have been a constant source of inspiration and motivation.

Thèse accessible à l'adresse : https://theses.insa-lyon.fr/publication/2024ISAL0034/these.pdf © [J. Jeong], [2024], INSA Lyon, tous droits réservés

Thèse accessible à l'adresse : https://theses.insa-lyon.fr/publication/2024ISAL0034/these.pdf © [J. Jeong], [2024], INSA Lyon, tous droits réservés

Contents

Thèse accessible à l'adresse : https://theses.insa-lyon.fr/publication/2024ISAL0034/these.pdf © [J. Jeong], [2024], INSA Lyon, tous droits réservés

Thèse accessible à l'adresse : https://theses.insa-lyon.fr/publication/2024ISAL0034/these.pdf © [J. Jeong], [2024], INSA Lyon, tous droits réservés

Chapter 1

Introduction

1.1 Context

Around 2 % of the total greenhouse gas emissions in developed countries are due to food transportation, including motive power and refrigeration [1]. For road transport vehicles, different types of refrigeration units are employed mainly depending on the size of the vehicle and its load: vapour compression system with a vehicle or an auxiliary alternator unit, a direct belt drive or an auxiliary diesel unit. For temperature-controlled vehicles, legislations such as Agreement on the International Carriage of Perishable Foodstuffs and on the Special Equipment to be used for such Carriage (ATP) [2] exist and provide common standards and certifications. Road transport refrigeration equipment needs to operate reliably in harsher environments and its operating conditions required to preserve the cold chain, constraints due to available space, noise and weight makes them less efficient than stationary systems. For medium to large road transport vehicles, refrigeration units are primarily powered by a self-contained diesel engine. To guarantee -20 °C within the trailer, the fuel consumption is typically up to 4 liters per hour for a semi-truck trailer with an inside volume of $78.79\,\mathrm{m}^3$ [1].

Eutectic systems typically consist of tubes, beams or plates filled with a Phase Change Material (PCM) and appear as an alternative to reduce or annihilate this fuel consumption. An example of eutectic refrigeration system inside a refrigerated truck trailer is shown in Figure 1.1. During the typical delivery cycle, the eutectic plates absorb heat infiltrated into the trailer as latent heat and produce cooling to ensure the desired regulated temperature inside the trailer. However, heat losses through frequent door openings are a major concern for a medium sized truck trailers with day-deliveries, especially in humid climates. Frequent door openings account for the majority of the heat infiltration during delivery and induce condensation and formation of ice along the plates [3; 4]. Thick condensed frost layers developed on the eutectic plates may interfere with the heat transfer with the surrounding air and reduce its effects.

1.2 Objectives

The main objective of this manuscript is to analyze the feasibility of the eutectic refrigeration system to replace the conventional refrigeration system powered by fossil fuels for the transport of frozen foodstuff. To analyze the feasibility of the eutectic system, overall performance of the system has to be accurately predicted. For the prediction of the overall system performance, the following analyses are required:

Thèse accessible à l'adresse : https://theses.insa-lyon.fr/publication/2024ISAL0034/these.pdf © [J. Jeong], [2024], INSA Lyon, tous droits réservés

Figure 1.1: Example of an eutectic refrigeration system inside a refrigerated truck trailer. Courtesy of FrygyCube.

- Analysis of the thermoaeraulic behavior of the air during the door opening period for a refrigerated truck trailer equipped with eutectic plates. Parameters such as the renewal time, temperature distribution of the truck trailer, and the maximum temperature observed by the cargo are few key parameters of the analysis.
- Prediction of the frost development on top of a cold plate under a wide range of initial and boundary conditions. As the infiltrating hot atmospheric air comes in contact with the cold plate, frost development is inevitable. However, most published numerical models has only been validated for very specific ranges of initial and boundary conditions. Therefore, a more generalized numerical model is required for a wider range of initial and boundary conditions.
- Prediction of the solidification and melting of the PCM. The eutectic refrigeration system is subjected to the heat infiltrated during the door opening periods of the refrigerated truck trailer. During the door opening period, eutectic mixture inside the eutectic refrigeration system will undergo a phase change. As the heat is not uniformly distributed throughout the eutectic refrigeration system, there will be an inhomogeneous phase change of the eutectic mixture. Therefore, a numerical model is required to predict the solidification and melting of the eutectic mixture during the door opening periods.

1.3 Novelty

One original aspect of this work lies with the choice of identifying the feasibility of the sub-zero eutectic system with a substantially low phase change temperature of $T = -29\,^{\circ}\mathrm{C}$ for the transport of frozen foodstuff. Due to the phase change temperature of the eutectic system, frost development occurs during the door opening period as the hot humid air comes in contact. Frost formed on top of the eutectic system interferes with the heat transfer between the eutectic mixture and the surrounding air. Additionally, as the frost

Thèse accessible à l'adresse : https://theses.insa-lyon.fr/publication/2024ISAL0034/these.pdf © [J. Jeong], [2024], INSA Lyon, tous droits réservés

formation is an exothermic process, it will release heat to the eutectic system and attribute towards the phase change of the system.

Furthermore, the analysis of the thermoaeraulic behavior of the air during the door opening of a refrigeration truck trailer equipped with eutectic plates includes two different fan operating modes and configurations of the eutectic plates. Presence of the cargo is also introduced to the system to analyze the temperature distribution of the cargo during the infiltration period to confirm it meets the regulatory temperature imposed by the ATP [2]. Additionally, the complete analysis of the frost development, solidification and melting of the PCM, and the thermoaeraulic behavior of the air for a refrigerated eutectic system has never been studied experimentally nor numerically in detail.

1.4 Structure of the manuscript

To achieve the objectives listed in Section 1.2, this manuscript is organized as follows:

1. Literature Review (Chapter 2): summarization of the state of the art of the researches related to the current objectives of the manuscript.

2. Infiltration model (Chapter 3): a model developed to accurately predict the infiltration behavior of the air during the door opening period of a refrigerated truck trailer equipped with eutectic plates.

3. Frost model (Chapter 4): an extended model of the works of Wu et *al.* [5] to predict the formation of the frost developed on top of a cold plate with its interaction with the air flow above the frost.

4. Consolidated model (Chapter 5): a model consolidating the aforementioned infiltration and frost model with the solidification and melting model to predict the overall performance of the eutectic plate system.

5. Conclusions and Future Works and Challenges (Chapters 6 in English and 7 in French): summarization of the objectives achieved within this manuscript. It contains also the possible future works that could be performed and the challenges associated with the current and future works.

Thèse accessible à l'adresse : https://theses.insa-lyon.fr/publication/2024ISAL0034/these.pdf © [J. Jeong], [2024], INSA Lyon, tous droits réservés

Thèse accessible à l'adresse : https://theses.insa-lyon.fr/publication/2024ISAL0034/these.pdf © [J. Jeong], [2024], INSA Lyon, tous droits réservés

Chapter 2

Literature Review

This chapter presents the results and methodologies employed by the researchers to investigate the key components (infiltration, frost development, solidification and melting) required to develop the comprehensive Computational Fluid Dynamics (CFD) model for a refrigerated truck trailer equipped with eutectic plates. Refrigeration systems currently employed for a refrigerated truck trailer are described in Section 2.1. Then the infiltration dynamics during the door opening for a refrigerated chamber and a refrigerated truck trailer are presented in Section 2.4. Finally, the physical phenomena involved with the eutectic refrigeration systems, frosting and solidification and melting of the PCM, are presented in Section 2.2.

2.1 Refrigeration Systems

2.1.1 Vapour Compression Systems

The majority of refrigeration systems currently employed for a refrigerated truck trailer are the vapour compression systems [3]. Depending on the factors such as weight, noise, maintenance, environmental concerns, and regulation, an appropriate vapour compression system is selected. Nevertheless, the Coefficient of Performance (COP) of the refrigeration systems for a truck trailer is relatively low. The value of COP typically ranges from 0.5 for $-20\,^{\circ}\mathrm{C}$ inner temperature and $1.5 \sim 1.75$ for $3\,^{\circ}\mathrm{C}$ inner temperature with the ambient temperature of $30\,^{\circ}\mathrm{C}$ [3]. Four vapour compression systems most commonly employed for a refrigerated transport are [3; 4]: vehicle alternator unit, direct belt drive, auxiliary alternator unit, and auxiliary diesel unit (Figure 2.1).

Vehicle alternator unit is commonly employed for a small delivery vans. The vehicle engine crankshaft is used to drive an upgraded single alternator. Then, the alternator charges the battery and powers the refrigeration system. Direct belt drive is mostly used for a van-sized vehicles. The vehicle engine directly drives the compressor of the refrigeration unit through a belt. Auxiliary alternator unit uses the main traction engine to drive a dedicated large alternator by a belt. The power generated from the main engine is used to drive the electric motor in the refrigeration unit. Auxiliary diesel unit is a system with a diesel engine incorporated into the refrigeration unit. This system is employed in the majority of the medium to large refrigerated vehicles [3; 1].

The vehicle alternator unit, direct belt drive, and auxiliary alternator unit provide limited power to the refrigeration system as the main source of power is from the main engine. Also the power losses through mechanical transmission by a crankshaft or a

Thèse accessible à l'adresse : https://theses.insa-lyon.fr/publication/2024ISAL0034/these.pdf © [J. Jeong], [2024], INSA Lyon, tous droits réservés

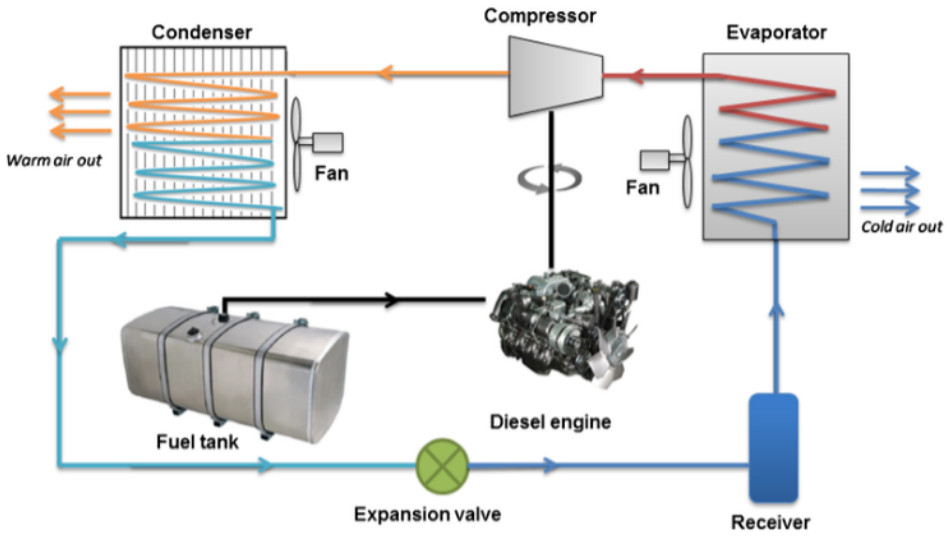

Figure 2.1: Schematic diagram of vapour compression transport refrigeration unit driven by a diesel engine [6].

belt contributes to their limited usage to a small to medium sized transport vehicle. Also, to meet the requirements of the ATP agreement [2] and operate over wide range of conditions, vapour compression refrigeration systems needs to be oversized by up to 1.75 time its calculated load [3]. Therefore, auxiliary diesel engines accounts for approximately 90 % of the market for the transport refrigeration system [6].

While the auxiliary diesel engine is capable of reliably providing power for a medium to large sized transport vehicle refrigeration system, it can also account up to 40 % of the environmental impact of the vehicle engine [3]. To reduce the environmental impact of the transport refrigeration systems, eutectic refrigeration systems are employed.

2.1.2 Eutectic Systems

Eutectic systems consists of tubes, beams or plates filled with a Phase Change Material (PCM) to store energy as latent heat and provide a cooling effect to maintain the desired temperature inside a transport vehicle (Figure 1.1). The main difference to the conventional system (vapour compression) is that the cold source is provided by the phase change of the material rather than the direct expansion of the refrigerant gas [3]. The eutectic systems operate silently and provide cooling for a specific duration before the PCM is completely melt. Also, static eutectic refrigeration units are capable of charging the PCM by a connector, eliminating the need to have its own condensing unit and leading to a decrease in the overall cost of the system [3].

However, for a medium-sized vehicle with multiple day-deliveries, heat losses through frequent door openings is a major concern. The majority of the heat infiltration during delivery is due to door openings and it can also induce frost and ice along the eutectic system [3; 4]. Frost and ice formed on the eutectic system could interfere with the heat transfer between the system and the surrounding air. Also, depending on the length of the delivery, frequency of the door openings, and time period, PCM inside the eutectic systems could also completely melt before the end of its delivery cycle. Therefore, more thorough analysis of the eutectic transport refrigeration system is required.

Thèse accessible à l'adresse : https://theses.insa-lyon.fr/publication/2024ISAL0034/these.pdf © [J. Jeong], [2024], INSA Lyon, tous droits réservés

2.1.3 Cryogenic Cooling System

Alternative to the eutectic refrigeration system, total loss systems using cryogenic fluids can also be employed. The cryogenic fluids are stored in tanks and connected to a spraying system through the length of the vehicle [3]. Then, it is released into the vehicle and vaporises to reduce the temperature inside. Cryogenic cooling system is capable of rapidly decreasing the temperature inside the vehicle with very low noise emissions. However, it is rather expensive to operate.

2.2 Phase Change Material

Latent heat storage provided by the PCMs is one of the most efficient methods to store thermal energy [7]. PCM takes advantage of the material's phase transition to store or release energy due to the enthalpy change caused by the phase change. Due to the phase change, the thermal energy storage operate almost isothermally at the phase change temperature of the material [7]. Initially, as the temperature increases or decreases, energy is stored or released by the temperature change of the storage material, acting as the sensible heat storage [7; 8]. The amount of sensible thermal energy stored is defined as:

$$Q_{sens} = m \int_{T_1}^{T_2} C_p \, \Delta T \tag{2.1}$$

where m is the mass of the storage material, C_p its specific heat, T_1 and T_2 are the initial and final temperatures, respectively.

As the temperature reaches the phase change temperature of the substance, the material consumes significant quantities of energy as latent heat. The amount of latent thermal energy stored is defined as:

$$Q_L = m\Delta h_L \tag{2.2}$$

with Δh_L the phase change enthalpy (Latent heat of fusion/solidification).

After the complete phase change of the substance, the energy is stored once again in sensible fashion as shown in Figure 2.2.

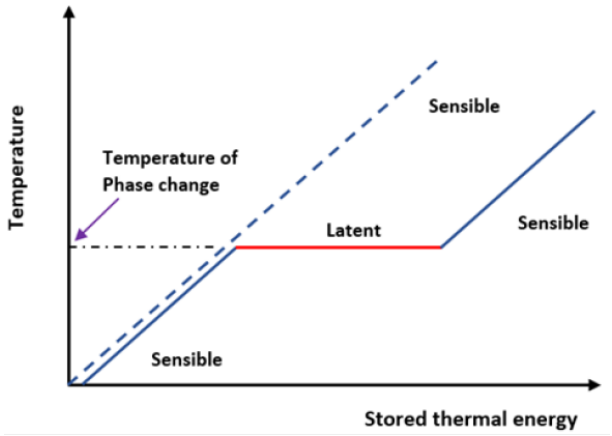

Figure 2.2: A schematic of sensible and latent heat storage principle [7].

Typically, PCM classifications are divided into four categories: solid-solid, solid-liquid, solid-gas, and liquid-gas [7; 8; 9; 10]. From these four types of PCMs, solid-liquid PCMs

Thèse accessible à l'adresse : https://theses.insa-lyon.fr/publication/2024ISAL0034/these.pdf © [J. Jeong], [2024], INSA Lyon, tous droits réservés

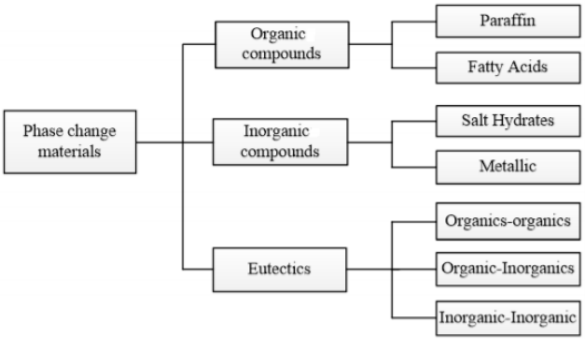

Figure 2.3: Overview of PCMs [10].

are the most suitable for thermal energy storage, and they are further classified as organic, inorganic and eutectic as shown in Figure 2.3.

Paraffin is typically composed of long straight chain of alkanes and the melting point depends on the length of the chain [7]. It has reasonably high heat of fusion and can be used over a wide range of temperature [10]. Fatty acid typically has higher heat of fusion compared to the paraffin wax with the ability to reproduce melting and freezing with little to no supercooling [10]. However, fatty acids can cost up to 2.0 to 2.5 times more than the cost of paraffin wax [10]. Salt hydrates are one of the most extensively studied PCM due to their moderately high thermal conductivity, cost and safety [7]. However, the salt hydrates exhibits incongruent melting when the salts are insoluble to its associated water, leaving the salt solution supersaturated after the phase transition [7]. Metallic PCMs have not been seriously considered due to their heaviness [10], but have gained some attraction recently due to some of their favourable characteristics such as high thermal conductivity, heat of fusion per unit volume and small volume change associated with phase change [7].

2.2.1 Solidification and Melting Model

For the latent heat storage systems such as PCMs, melting and solidification are the two processes generally involved. Heat is transferred to a solid PCM and the melting occurs as the latent heat is stored. Reversely, when the latent heat is released, solidification occurs and the heat is transferred from the PCM. Therefore, the PCM transition involves a solid, a mushy, and then a liquid state. The heat transfer associated can be either by conduction or convection (mostly by natural convection) [11].

The solidification and melting model based on the enthalpy porosity method of Brent et *al*. [12] is already readily available and well established in ANSYS FLUENT [13]. Zarajabad and Ahmadi [14] numerically investigated the effective PCM volume to be employed for a cold storage by the solidification and melting model. Zarajabad and Ahmadi [14] employed an eutectic solution of $NaCl - H_2O$ as the PCM with $-21°C$ melting temperature. Gou et *al*. [15] numerically simulated the cold energy release process of a cold storage plate in a container for temperature control by employing the Volume of Fluid (VOF) multiphase flow model and the solidification and melting model in ANSYS FLUENT. The impacts of the inlet velocity of $1.8\,\mathrm{m\,s^{-1}}$ to $4.2\,\mathrm{m\,s^{-1}}$ and the spacing of the cold storage plates of $10, 20$ and $30\,\mathrm{mm}$ on the release of the cold energy were investigated. Calati et *al*. [16] employed the solidification melting model in ANSYS FLUENT to numerically investigate the effects of the PCM system for food transportation with the

Thèse accessible à l'adresse : https://theses.insa-lyon.fr/publication/2024ISAL0034/these.pdf © [J. Jeong], [2024], INSA Lyon, tous droits réservés

melting range of PCM being between 1 to 3 °C.

The enthalpy-porosity approach proposed by Voller et *al.* [17] and Brent et *al.* [12] has been shown to adequately describe the natural convection effect in the melting region. It is capable of accurately predicting the transient position and shape of the melt front. In this model, the fraction of the cell volume that is in liquid form is computed at each iteration based on an enthalpy balance. Liquid fraction of 0 indicating a completely solid state and 1 indicating a completely liquid state. The mushy zone is modelled as a porous medium where the porosity decrease from 1 to 0 as the solidification occurs. As the solidification process complete, the porosity becomes zero and so does the velocities.

The enthalpy-porosity model based on the energy equation is described below [17; 12]:

$$\frac{\partial}{\partial t}(\rho h) + \nabla \cdot (\rho v h) = \nabla \cdot (\lambda \nabla T) + S \tag{2.3}$$

with h the enthalpy, ρ the density, v the fluid velocity, λ the thermal conductivity and S the source term.

$$h = h_{ref} + \int_{T_{ref}}^{T} C_p \, dT + \phi \Delta h_l \tag{2.4}$$

Enthalpy considers both the sum of sensible enthalpy and the latent heat of fusion (h_l), with ϕ the liquid fraction. The liquid fraction is identified by:

$$\phi = \begin{cases} 0, & T < T_s \\ \frac{T - T_s}{T_l - T_s}, & T_s < T < T_l \\ 0, & T > T_l \end{cases} \tag{2.5}$$

with T_s and T_l the solidus and liquidus temperatures.

The momentum sink is also applied for the reduced porosity in the mushy zone as following:

$$S_u = \frac{(1-\phi)^2}{\phi^3 + \chi} A_{mush} v \tag{2.6}$$

where χ is a small number (default value of 0.001) to prevent division by zero, A_{mush} the mushy zone constant, v the fluid velocity and subscript u refers to the momentum.

The solidification and melting model based on the enthalpy-porosity approach has been employed by the researchers for the PCM phase changes in various applications. The described models in Table 2.1 focuses on the rectangular geometry, to be applied for the eutectic plates inside a refrigerated truck trailer.

All of the aforementioned models were able to accurately predict the solidification and melting of the PCM using the existing "Solidification and Melting" model in FLUENT. However, the obtained results depended heavily on the value of the mush zone parameter, A_{mush}. The mushy zone parameter (A_{mush}) is set to the default value of 10^5 with the recommended operating range between 10^3 and 10^8. The mushy zone parameter determines the amplitude of the damping, the higher the value, the faster the velocity of the material becomes zero as it solidifies. Furthermore, the mushy zone significantly influences the heat transfer and flow characteristics during the solidification and melting process. Fadl and Eames [11] investigated the effect of the value of the mushy zone parameters and compared the results against the experimental results of Shokouhmand and Kamkari [22].

In Figure 2.4, predicted melt front locations with different values of A_{mush} obtained by Fadl and Eames [11] is presented. From the obtained results, resulting shape of the solid PCM for $A_{mush} = 5 \times 10^5$ presented with the most agreeable results against the

Thèse accessible à l'adresse : https://theses.insa-lyon.fr/publication/2024ISAL0034/these.pdf © [J. Jeong], [2024], INSA Lyon, tous droits réservés

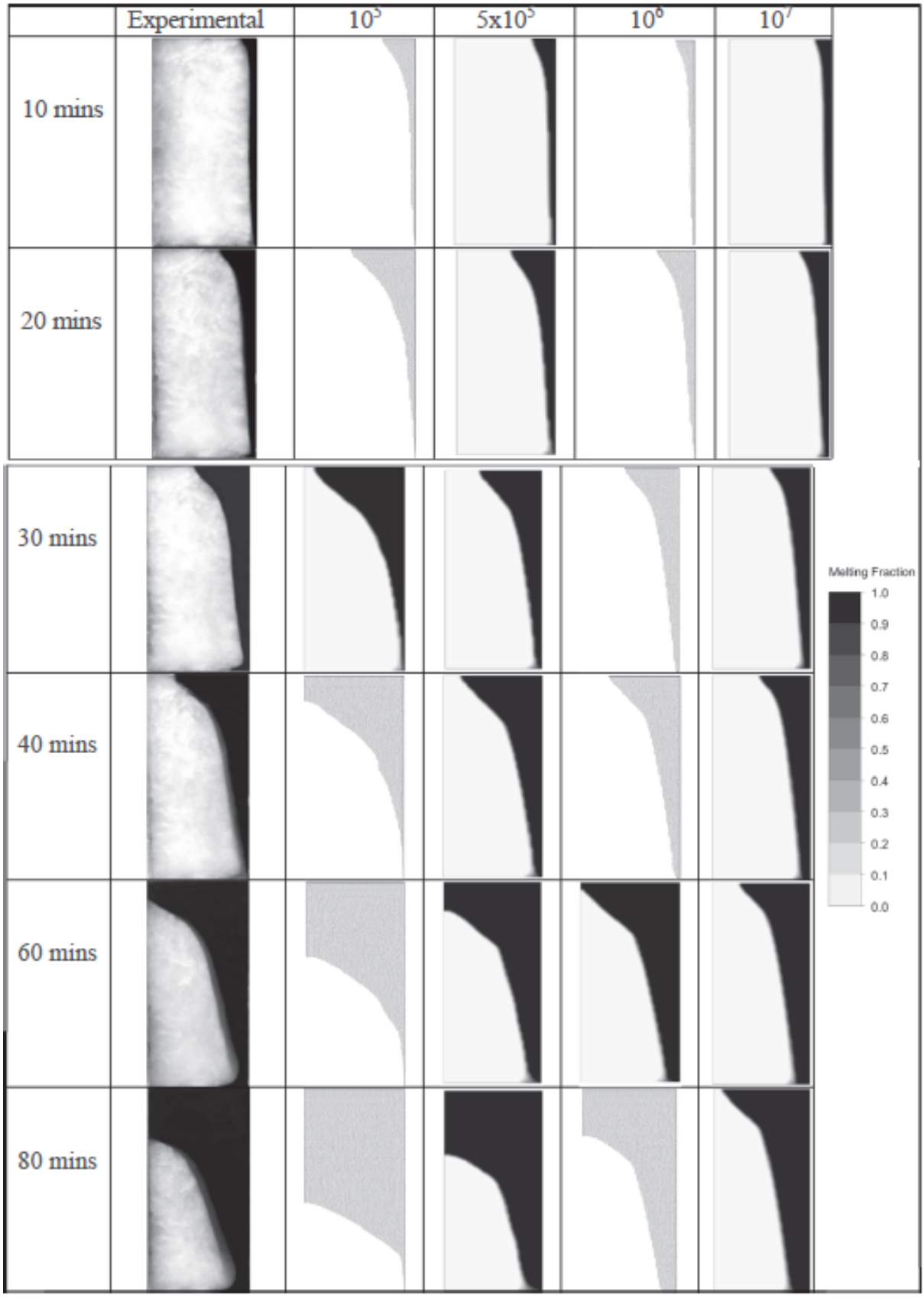

Figure 2.4: Experimental and predicted melt front locations with time for different values of A_{mush} indicated on the top [11].

Thèse accessible à l'adresse : https://theses.insa-lyon.fr/publication/2024ISAL0034/these.pdf © [J. Jeong], [2024], INSA Lyon, tous droits réservés

Author(s)	PCM	Mesh	Time step	Material Property
Vogel et $al.$ [18]	Eutectic mixture	Non-uniform wall refinement	$0.0125\,\mathrm{s}$	Boussinesq (Constant)
Kim et $al.$ [19]	Gallium	Not Available	Not Available	Temperature-Varying
Fadl and Eames [11]	Lauric acid	Uniform $1\,\mathrm{mm} \times 1\,\mathrm{mm}$	$0.2\,\mathrm{s}$	Not Specified
Oliveski et $al.$ [20]	Lauric acid	Non-uniform $A_{cell} \approx 1.45\,\mathrm{mm}^2$	$0.1\,\mathrm{s}$	Temperature-Varying
Abdulmunem et $al.$ [21]	Paraffin wax	Uniform $0.0625\,\mathrm{mm} \times 0.25\,\mathrm{mm}$	$0.5\,\mathrm{s}$	Temperature-Varying
Zarajabad and Ahamdi [14]	$NaCl - H_2O$	Quad element	$0.1\,\mathrm{s}$	Boussinesq (Constant)
Gou et $al.$ [15]	Water	Rectangular mesh 8.3×10^5 elements	Not Available	Boussinesq

Table 2.1: Summary of recent investigations on rectangular PCM solidification and melting problems.

experimental results. However, as the value of A_{mush} increased, the numerical predictions of the melt front lagged behind the experimental results and had a sharper curvature along the melt interface. On the contrary, as the value of A_{mush} decreased, the melt front exceed that of the experimental results and overpredicted the melting process. However, Fadl and Eames [11] noted that the extent of correlation between the values of A_{mush} and the material properties are unknown and an approach to identify the optimal value of the mush parameter does not exists as of yet.

2.2.2 PU-PCM Truck Trailer Walls

In the recent years, application of PCMs for the walls of refrigerated vehicles have been proposed and investigated by the researchers [3; 1; 23; 24; 25]. Tinti et $al.$ [23] investigated the characteristics of rigid polyurethane (PU) foams typically used as refrigerated truck trailer walls, containing MicroPCM. They found that with increasing PCM content, the thermo-regulating and thermal energy capabilities of PU-PCM foams increased. Copertaro et $al.$ [24] and Michel et $al.$ [25] investigated the thermal performance of a sandwich structured PU-PCM insulation walls for the refrigerated vehicles. The effect of the design of the PU-PCM walls (PU/PCM layer thickness, PCM mixture, ...) on their thermal performances over 24 hours was analyzed. However, none of the aforementioned studies analyzed the heat transfer inside the refrigerated vehicle. Most recently, Calati et $al.$ [26] numerically investigated the performance of the PU-PCM walls for a refrigerated truck trailer, considering the solar radiation from 6 AM to 4 PM of a typical summer day in Vicenza (Italy). They simulated the solidification and melting of the PCM by using the existing package in FLUENT. While the heat transfer inside a refrigerated vehicle was considered, the analysis was carried out for a closed configuration.

Thèse accessible à l'adresse : https://theses.insa-lyon.fr/publication/2024ISAL0034/these.pdf © [J. Jeong], [2024], INSA Lyon, tous droits réservés

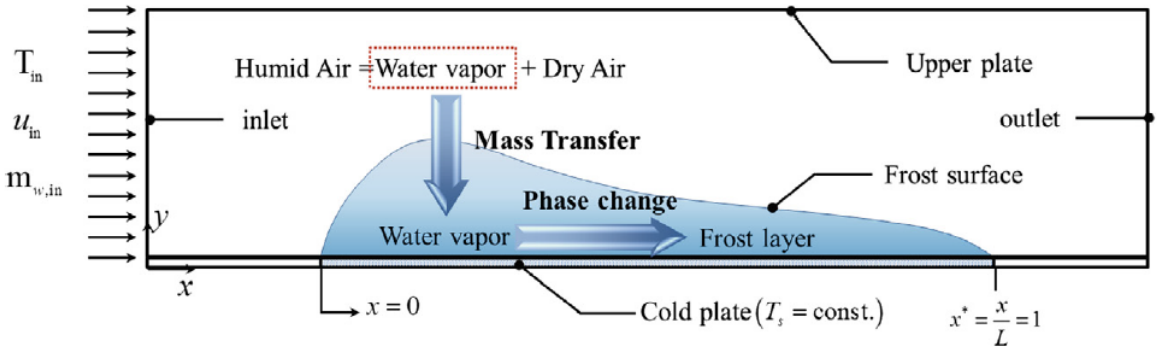

Figure 2.5: Schematic diagram of the physical processed involved in frost development [29].

2.3 Frost Model

To the best of the author's knowledge, there has yet to be an investigation on the frost development on the PCM. Berdja et *al.* [27] experimentally and analytically investigated the characteristics and thickness effect of PCM and frost for a conventional refrigerator. However, their analytical model did not consider the formation of frost on top of the PCM. But, rather incorporated the thermal resistance of the frost to the overall heat transfer coefficient and investigated the influence of the frost on the heat transfer depending on the varying thickness. Therefore, comprehensive models capable of simulating the development of frost on the PCMs (eutectic plates) as well as the solidification and melting of the PCMs (described in Section 5.1.4) are required.

Frost is a thin layer of ice formed on top of a solid surface with a below freezing temperature when the water vapor in an above-freezing condition comes in contact. Figure 2.5 presents generalized schematic of the frost formation on a cold plate. Hayashi et *al.* [28] divided the frost formation into three steps: the crystal growth period, the frost layer growth period and the frost layer full growth period (densification). The frost formation steps are detailed below [28]:

1. Crystal growth period: initially, a thin layer of frost covers the surface. Then the frost crystals located relatively far apart from each generate on the thin frost surface and grow in vertical direction at an approximately same rate. This crystal growth is approximately characterized by a growth in a linear direction.

2. Frost layer growth period: Rough frost (cluster of rod type crystals) changes in shape by generating branches around the top of a crystal or by the interaction of each crystal. Then it grows gradually into a meshed and progressively more uniform structure until the frost surface becomes nearly flat. During this period, density of the frost increases with the frost layer growth.

3. Frost layer full growth period: the shape of the frost layer does not change until the surface temperature becomes 0 °C due to its increased thermal resistance. Then the melted water from the frost surface soaks into the frost layer and freezes. This phenomenon increases the frost layer density and the frost deposition occurs again. This cycle continues periodically until the equilibrium condition of the heat transfer is reached and the frost formation stops.

In the last decades, there has been extensive research on the development of frost, both experimentally and theoretically. Hayashi et *al.* [28] and Tao et *al.* [30] modeled the

Thèse accessible à l'adresse : https://theses.insa-lyon.fr/publication/2024ISAL0034/these.pdf © [J. Jeong], [2024], INSA Lyon, tous droits réservés

fully developed growth period as a homogeneous porous medium with diffusion leading to the frost growth and densification. Jones and Parker [31] developed a model based on the mass and energy balances and diffusion of the water vapour molecules at the frost interface. O'Neal and Tree [32] calculated the mass transfer by modeling the diffusion of molecules in porous media and proposed frost thickness correlation based on their experimental results. Then, Na and Webb [33], Lee et *al.* [34], and Yao et *al.* [35] further improved upon the model of O'Neal and Tree. The interested readers are referred to the work of Léoni et *al.* [36] for further details on the empirical and theoretical models for the frost formation developed over the years.

Frost formation models can be classified into three different categories.

1. Frost formation without the consideration of the influence of the air flow [33; 31; 37; 38; 39]: the heat and mass transfers were calculated using the empirical correlation for the diffusion on the air side. Na and Webb [33; 37] assumed the humid air to be supersaturated, while Barron et *al.* [39], Jones and Parker [31], and Lee et *al.* [38] assumed that the humid air was saturated near the frost surface.

2. Frost formation with consideration of both the frost region and the humid air region. The interface condition was employed to connect the two regions [34; 40; 41; 42]. Lee et *al.* [34], Yang and Lee [41], and Yang et *al.* [42] calculated the frost growth on a cold plate with laminar and turbulent flow with this model.

3. Frost formation modeled by considering the mass transfer between the water vapour within the humid air to the ice. Multi-phase flow methods are employed to solve the governing equations for the humid air and the ice phases. Frosting processes were simulated by adding the mass transfer source terms to the governing equations. Cui et *al.* [43; 44] proposed a frosting mass transfer source term based on the nucleation theory to model the frost formation on the flat plate and the fin-and-tube heat exchanger surfaces. Zhaung et *al.* [45] implemented the mass transfer source term model to simulate the condensing droplet formation. Wu et *al.* [5; 46] proposed a frosting mass transfer source term by assuming the phase change driving force from the water vapour to the ice as the difference between the water vapour partial pressure in the humid air and the water vapour saturation pressure based on the frost surface temperature. Wu et *al.* [5; 46] used the model to simulate the frost formation on a flat plate with a local cooling and fin-and-tube heat exchanger surfaces and obtained good agreement with the experimental results. Afrasiabian et *al.* [47] later extended the model of Wu et *al.* [46] by separating the velocity and the water vapour concentration parameters of the frosting condition to simulate the frost growth on one channel of a plate-fin evaporator.

However, the models belonging to the first and the second categories determine the thickness and the weight of the frost without considering the interaction between the humid air flow field change and the frost growth [46]. The frosting model based on the mass transfer source terms can simulate the interaction between the humid air flow field change and the frost growth, predicting the localized frost and humid air flow characteristics (Figure 2.6). Therefore, among the three categories of frost formation models, the ones with the mass transfer during the frost formation contributing to the increase in both the frost thickness and density showed best agreement with the experimental frost data [5; 46].

Thèse accessible à l'adresse : https://theses.insa-lyon.fr/publication/2024ISAL0034/these.pdf © [J. Jeong], [2024], INSA Lyon, tous droits réservés

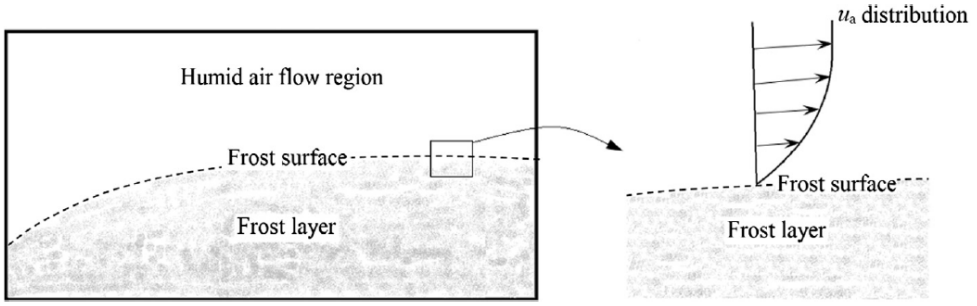

Figure 2.6: Schematic diagram for the computing domain in the frosting process [46].

Cui et *al.* [43; 44], Wu et *al.* [5; 46], and Afrasiabian et *al.* [47] employed a Eulerian-Eulerian multiphase model with the mass transfer source terms between the primary phase of humid air and the secondary phase of ice. Based on the mass transfer, the momentum and energy transfers from water vapor to ice can occur and are reflected as the momentum and energy source terms of the governing equations. Also a source term is included in the species conservation equation for the water vapour diffusion driven by the concentration gradient from the humid air to the frost layer. Therefore, two sets of conservation equations for mass (Equation 2.7, 2.8), momentum (Equation 2.9, 2.10), energy (Equation 2.11, 2.12), and a species conservation equation (Equation 2.13) were solved:

$$\frac{\partial}{\partial t}(\alpha_c \rho_c) + \nabla \cdot (\alpha_c \rho_c u_c) = S_{mc} \tag{2.7}$$

$$\frac{\partial}{\partial t}(\alpha_a \rho_a) + \nabla \cdot (\alpha_a \rho_a u_a) = S_{ma} \tag{2.8}$$

$$\frac{\partial}{\partial t}(\alpha_c \rho_c u_c) + \nabla \cdot (\alpha_c \rho_c u_c u_c) = K_{ac}(u_a - u_c) - \alpha_c \nabla P + \nabla \cdot \bar{\tau}_c + \alpha_c \rho_c g + S_{uc} \tag{2.9}$$

$$\frac{\partial}{\partial t}(\alpha_a \rho_a u_a) + \nabla \cdot (\alpha_a \rho_a u_a u_a) = K_{ca}(u_c - u_a) - \alpha_a \nabla P + \nabla \cdot \bar{\tau}_a + \alpha_a \rho_a g + S_{ua} \tag{2.10}$$

$$\frac{\partial}{\partial t}(\alpha_c \rho_c h_c) + \nabla \cdot (\alpha_c \rho_c u_c h_c) = \bar{Q}_{ac} + \alpha_c \frac{\partial p_c}{\partial t} + \bar{\tau}_c : \nabla u_c - \nabla \cdot \vec{q_c} + S_{hc} \tag{2.11}$$

$$\frac{\partial}{\partial t}(\alpha_a \rho_a h_a) + \nabla \cdot (\alpha_a \rho_a u_a h_a) = \bar{Q}_{ca} + \alpha_a \frac{\partial p_a}{\partial t} + \bar{\tau}_a : \nabla u_a - \nabla \cdot \vec{q_a} + S_{ha} \tag{2.12}$$

$$\frac{\partial}{\partial t}(\alpha_a \rho_a w_v) + \nabla \cdot (\alpha_a \rho_a w_v u_a) = \nabla \cdot (\rho_a D_{H_2O} \nabla w_v) + S_{va} \tag{2.13}$$

with α the volume fraction, ρ the density, u the velocity, K the momentum transfer coefficient, g the gravity, $\bar{\tau}$ the stress-strain tensor, $\bar{Q}$ the interphase heat transfer, $\vec{q}$ the heat flux, w the mass fraction, and D_{H_2O} the diffusivity of the water vapour.

The mass (Equations 2.14, 2.15), momentum (Equations 2.16, 2.17), energy (Equations 2.19, 2.18) and species(Equations 2.20) sources employed for the defined mass transfer rate ($\dot{m}_{ac}$) are listed below:

$$S_{mc} = \dot{m}_{ac} - \dot{m}_{ca} = \dot{m}_{ac} \tag{2.14}$$

$$S_{ma} = -\dot{m}_{ac} \tag{2.15}$$

$$S_{uc} = \dot{m}_{ac} u_c \tag{2.16}$$

$$S_{ua} = -\dot{m}_{ac} u_c \tag{2.17}$$

Thèse accessible à l'adresse : https://theses.insa-lyon.fr/publication/2024ISAL0034/these.pdf © [J. Jeong], [2024], INSA Lyon, tous droits réservés

$$S_{ha} = \dot{m}_{ac} h_{va} \tag{2.18}$$

$$S_{hc} = \dot{m}_{ac}(h_{va} + \Delta h_{L,va}) \tag{2.19}$$

$$S_{va} = -\dot{m}_{ac} \tag{2.20}$$

Author(s)	Mesh	Time step	Method	Simulation parameters
Cui et *al.* [43; 44]	Non-uniform, wall refinement $n_x \times n_y = 300 \times 30$	1 s	Nucleation	$0.6 \leq u_{in} \leq 2.5\,\mathrm{m\,s^{-1}}$ $T_{in} = 19.8$℃ $T_{plate} = -20.5$℃ $RH = 58\%$
Wu et *al.* [5]	Uniform, $1\,\mathrm{mm} \times 0.05\,\mathrm{mm}$	1.0 s	Phase change driving force	$u_{in} = 1.5\,\mathrm{m\,s^{-1}}$ $T_{in} = 2\,^{\circ}\mathrm{C}$ $T_{plate} = -9\,^{\circ}\mathrm{C}$ $RH = 83$ %
Wu et *al.* [46]	Uniform, $0.1\,\mathrm{mm} \times 0.05\,\mathrm{mm}$	1 s	Phase change driving force	$0.31 \leq u_{in} \leq 0.92\,\mathrm{m\,s^{-1}}$ $-5 \leq T_{in} \leq 21.4\,^{\circ}\mathrm{C}$ $-20 \leq T_{plate} \leq -5\,^{\circ}\mathrm{C}$ $38 \leq RH \leq 85$ %
Afrasiabian et *al.* [47]	Not Available	1 s	Phase change driving force	$u_{in} = 0.7\,\mathrm{m\,s^{-1}}$ $1.7 \leq T_{in} \leq 22\,^{\circ}\mathrm{C}$ $-16 \leq T_{plate} \leq -4\,^{\circ}\mathrm{C}$ $80 \leq RH \leq 85$ %

Table 2.2: Summary of the frost model based on the mass transfer rate.

Cui et *al.* [43; 44] defined the mass transfer rate, $\dot{m}_{ac}$, based on the classical homogeneous nucleation theory as:

$$\dot{m}_{ac} = \frac{4}{3}\pi\rho_c I {r^*}^3 + 4\pi\rho_c\eta\bar{r}^2\frac{\delta\bar{r}}{\delta t} \tag{2.21}$$

with I the rate of nucleation per unit volume, ρ_i the density of ice, r^* the Kelvin-Helmholtz critical radius, η number of droplets per unit volume, $\bar{r}$ droplet radius, $\frac{\delta\bar{r}}{\delta t}$ the nucleation growth rate.

Wu et *al.* [5] defined the mass transfer rate based on the phase change driving force as:

$$\dot{m}_{ac} = \begin{cases} \tau_v \alpha_a \rho_a (w_{va} - w_{vs}), & w_{va} - w_{vs} > B u_a \\ 0, & \text{otherwise} \end{cases} \tag{2.22}$$

Where, τ_v is the time relaxation coefficient, α_a the volume fraction of humid air, ρ_a the density of humid air, w_{va} mass fraction of water vapour, and w_{vs} saturated water vapour mass fraction.

Then Wu *al.* [46] modified the correlation by replacing the phase change driving force $(w_{va} - w_{vs})$ with $w_{va}\frac{w_{va}-w_{vs}}{w_{vs}}$ as following:

$$\dot{m}_{ac} = \begin{cases} \tau_v \alpha_a \rho_a w_{va} \frac{w_{va}-w_{vs}}{w_{vs}}, & \frac{w_{va}-w_{vs}}{w_{vs}} \geq B\frac{u_a}{u_{in}} \\ 0, & \text{otherwise} \end{cases} \tag{2.23}$$

Thèse accessible à l'adresse : https://theses.insa-lyon.fr/publication/2024ISAL0034/these.pdf © [J. Jeong], [2024], INSA Lyon, tous droits réservés

Finally, Afrasiabian et *al*. [47] modified the frosting criteria by separating the velocity component from the water vapour concentration:

$$\dot{m}_{ac} = \begin{cases} \tau_v \alpha_a \rho_a w_{va} \frac{w_{va} - w_{vs}}{w_{vs}}, & w_{va} - w_{vs} > 0 \; and \; \frac{u_a}{u_{in}} \leq B \\ 0, & \text{otherwise} \end{cases} \tag{2.24}$$

Afrasiabian et *al*. [47] reported a reduced sensitivity of the mass transfer to the value of the non-dimensional frosting coefficient, B.

Compared to the experimental results of Lenic et *al*. [40], numerical results of Cui et *al*. [43] showed a satisfactory agreement with a maximum error of approximately 13 % for the frost layer thickness. The results of Afrasiabian et *al*. [47] demonstrated a maximum difference of 7 % against the experimental data of Sommmer et *al*. [48] after 30minutes for the average frost thickness and density. However, the frosting criteria parameter, B, is not defined by Afrasiabian et *al*. [47]. While the non-dimensional coefficient, B, from Table 2.2 is developed only for the simulation conditions of the cooling surface temperature between $-20\,^{\circ}\mathrm{C}$ and $-5\,^{\circ}\mathrm{C}$, air velocity between 0.31 and $0.92\,\mathrm{m\,s^{-1}}$, and the water vapour mass fraction between 0.002 and 0.006 by Wu et *al*. [46]. Cui et *al*. [43; 44], Wu et *al*. [5; 46], and Afrasiabian et *al*. [47] performed their simulations using FLUENT with the User Defined Function (UDF) DEFINE_MASS_TRANSFER to define the mass transfer source term. Table 2.2 presents the simulation parameters employed for the frost models based on the mass transfer rate.

2.4 Infiltration

2.4.1 Refrigerated Chamber

The heat and mass transfers inside a refrigerated truck trailers exhibit some similarities with those in a refrigerated chamber. However, the heat and mass transfers inside a refrigerated chamber have received significantly more attention by the researchers. Therefore, infiltration dynamic for a refrigerated chamber is firstly introduced in this section. During the door opening period for a refrigerated chamber, numerically, infiltration does not present with constant infiltration with time. Rather, infiltration can be split into three separate stages as shown in Figure 2.7: lag, steady state, and tail off stages [49]. Lag stage corresponds to the initial few seconds after the door opening when the flow takes some time to fully develop. It is then proceeded by the steady-state stage where there is a constant flow rate through the entrance. Then finally, tail off stage where the temperature difference (driving force) between the cold store and the surroundings is reduced.

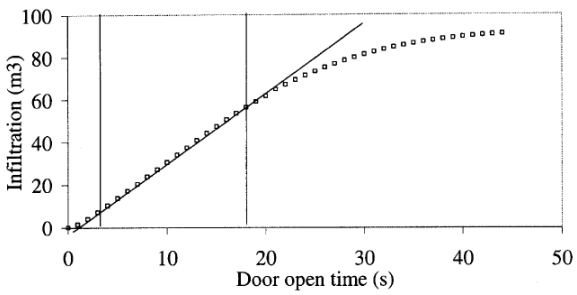

Figure 2.7: Predicted infiltration for the $2.3\,\mathrm{m}$ wide entrance for different door opening times [49].

Thèse accessible à l'adresse : https://theses.insa-lyon.fr/publication/2024ISAL0034/these.pdf © [J. Jeong], [2024], INSA Lyon, tous droits réservés

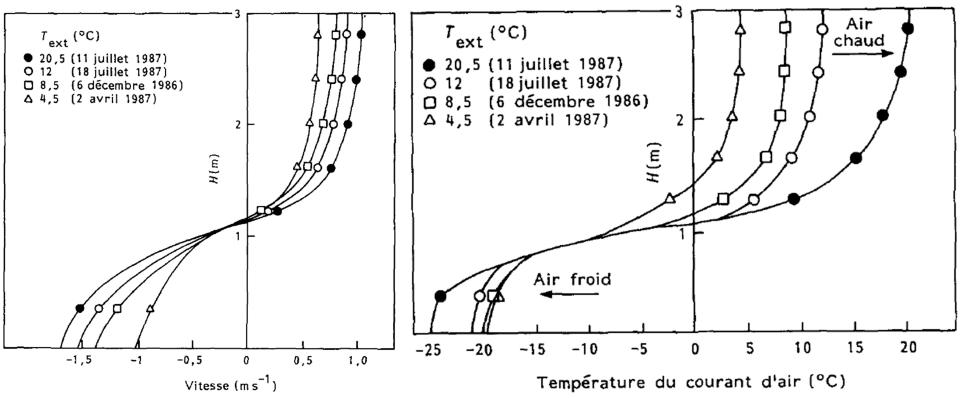

Figure 2.8: Deformation of temperature (left) and velocity (right) profiles with respect to the exterior temperature [50].

For the velocity and temperature profiles during the door opening period at the doorway vertical centerline, there exists a "neutral point" where the internal and external potential pressure are equal and the mean velocity between the infiltration and exfiltration is null [50]. This point is typically situated approximately at the location $y \approx H/3$ (Figure 2.8). Where H corresponds to the height of the doorway. In the region near the neutral point, there is a continuous mixing and swirling of the cold and the hot air present. But as the velocity magnitude in this region is minute, it is challenging to identify the directions of the movement of the air in this region.

In the region above the neutral point, hot exterior air enters into the chamber with a velocity that increases when y increases from the neutral point. Similarly, cold air from the chamber exits through the zone below the neutral point with a velocity that increases when y decreases from the neutral point. The velocity of the air strongly correlates to the temperature difference between the hot atmospheric air and the cold air inside the chamber. Another main flow characteristic is that the flow variables vary mainly in the vertical direction, but exhibits small to negligible differences horizontally [50]. This behaviour is used for the justification of a 2D model to accurately simulate the infiltration during the door opening period by Croquer et *al.* [4], and Bonaventure et *al.* [51].

Azzouz et *al.* [50] experimentally determined the cold losses caused by the door openings for a refrigerated chamber with an inner volume of approximately $13\,000\,\mathrm{m}^3$ with four identical doors of 3 m in height and 2.8 m in length. The speed of air during the door opening period varied between 0 to $1.5\,\mathrm{m\,s}^{-1}$ with the temperature ranging between -25 and $25\,^{\circ}\mathrm{C}$. The velocity field reached steady state 3.0 s after the door opening, while the temperature field reached steady state more than 13.0 s after the door opening.

Foster et *al.* [49] experimentally and numerically investigated the heat and mass transfers between a refrigerated store with an inner volume of approximately $106\,\mathrm{m}^3$ with a large single opening of $7.36\,\mathrm{m}^2$. Temperature inside the refrigerated store was set at $-20\,^{\circ}\mathrm{C}$ with the external temperature of $20\,^{\circ}\mathrm{C}$. Before the door opening period, the evaporator fans were switched off to allow for the air movement to settle for 30 s. Then the infiltration was measured for the door opening times of $10, 20, 30$, and 40 s. The infiltration rate increased linearly with the opening time until reaching an asymptotic value corresponding approximately to 90 % of the inside store volume at $t \approx 18\,\mathrm{s}$. Foster et *al.* [49] calculated infiltration rate based on the concentration of CO_2 before the door opening and after closing the door.

Furthermore, many expressions for the steady-state heat infiltration rate based on the

Thèse accessible à l'adresse : https://theses.insa-lyon.fr/publication/2024ISAL0034/these.pdf © [J. Jeong], [2024], INSA Lyon, tous droits réservés

ideal flow theory for natural convection of fluids at different densities through openings have been developed over the years [52; 53; 54; 55; 56; 57].

Author(s)	Infiltration Expression [m^3]
Brown and Solvason [53]	$I = 0.343A(gH)^{0.5}[\frac{\rho_i-\rho_o}{\rho_{avg}}]^{0.5}[(1-0.498)\frac{b}{H}]$
Tamm [54]	$I = 0.333A(gH)^{0.5}[\frac{\rho_i-\rho_o}{\rho_i}]^{0.5}[\frac{2}{1+(\rho_o/\rho_i)^{0.333}}]^{1.5}$
Fritzsche and Lilienblum [55]	$I = I_{Tamm}K_{f,L},\ K_{f,L} = 0.48 + 0.004(T_o - T_i)$
Gosney and Olama [56]	$I = 0.221A(gH)^{0.5}[\frac{\rho_i-\rho_o}{\rho_i}]^{0.5}[\frac{2}{1+(\rho_i/\rho_o)^{0.333}}]^{1.5}$
Pham and Oliver [57]	$I = 0.226A(gH)^{0.5}[\frac{\rho_i-\rho_o}{\rho_i}]^{0.5}[\frac{2}{1+(\rho_o/\rho_i)^{0.333}}]^{1.5}$

Table 2.3: Comparison of the expressions for the infiltration rate used in various analytical models.

In Table 2.3, various expressions for the infiltration through a doorway by natural convection are summarized. Brown and Solvason [53] assumed that the height of the neutral level is half the height of the doorway, attributing to the substantial over-prediction (52.1 to 122.7 %) of the infiltration rate compared to the experimental results of Foster et *al*. [49]. Whereas Tamm [54] improved upon the model by calculating the height of the neutral level and replacing ρ_{avg} with ρ_i and resulted in better prediction of the infiltration rate [49]. Fritsche and Lilienblum [55] added a correction factor ($K_{f,L}$) accounting for the contraction of the flow, friction and thermal effects based on the experiments performed using vane anemometers. It assumed that the infiltration volume flow rate is equal to the exfiltration volume flow rate. However, this is only if the air entering into the refrigerated chamber does not cool. Therefore, Gosney and Olama [56] instead provided an equation for the constant mass flow rate (as the mass of air inside refrigerated chamber remains constant) by replacing the term (ρ_o/ρ_i) with (ρ_i/ρ_o). Finally, Pham and Oliver [57] modified Tamm's equation based on their experiments.

However, it was identified that these analytical models based on the ideal flow theory generally over-predicts the experimental results [58; 59]. Foster et *al*. [49] observed that the Gosney model was the best analytical model from Table 2.3, with the model accurately predicting the infiltration within the experimental error for two of their experiments. Interestingly, their CFD predictions showed significant improvement in accuracy over the fundamental analytical equations of Brown and Tamm, but less accurate to those of Gosney and Fritzsche. The authors suggested that a more detailed CFD model would likely yield a better results, but it could not be done due to limited computing resources.

2.4.2 Refrigerated Truck Trailer

While the heat and mass transfer inside a refrigerated truck trailer exhibit some similarities with those in a refrigerated chamber, it is not possible to simply apply the analytical models for the chambers mentioned in Section 2.4.1 such as the Gosney model directly to the refrigerated truck trailer. The main cause is due to the significant difference of the opening area to enclosure volume ratio between the refrigerated truck trailer and the refrigerated chamber. Therefore, heat and mass transfer inside a refrigerated truck trailer requires separate analysis from the refrigerated chamber. However, as there has not been as much attention to the refrigerated truck trailers than for the refrigerated chambers, it is still a topic of interest for the researchers.

Thèse accessible à l'adresse : https://theses.insa-lyon.fr/publication/2024ISAL0034/these.pdf © [J. Jeong], [2024], INSA Lyon, tous droits réservés

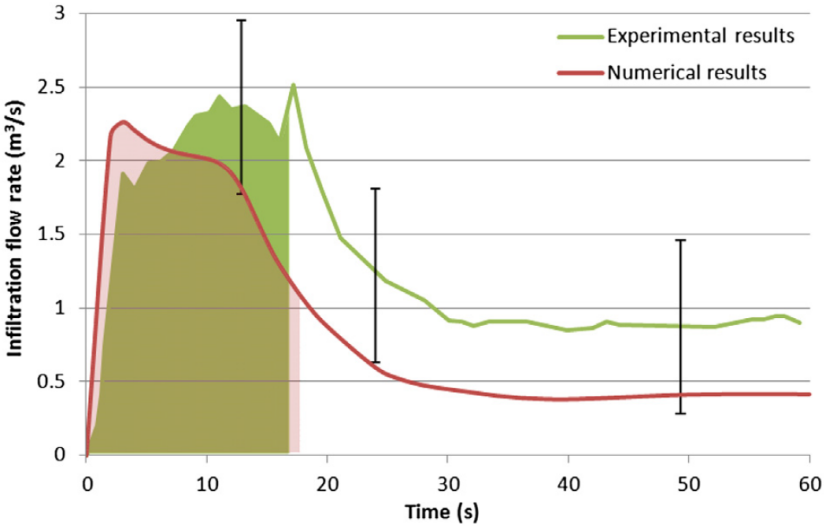

Figure 2.9: Evolution of the infiltration flow rate for the baseline case [60].

For the refrigerated chamber, infiltration is solely driven by the temperature difference between the cold storage and the surrounding air. However, Lafaye de Micheaux et *al.* [60] observed that during the door opening period for a truck trailer, two different mechanisms were observed for the heat and mass exchanges (Figure 2.9):

1. The volume flow rate increases progressively while the flow pattern develops over the doorway. Then, an unsteady mass exchange ("buoyancy-driven flow" [60]) occurs driven by the density differences between the inner and external air volumes. The volume flow rate reaches its peak value then quickly decreases as the temperature of the inner volume increases, effectively reducing the driving force for the unsteady mass exchange.

2. Heat exchange between the outside air and the inner walls ("boundary layer flow" [60]). As the inner volume is filled with the atmospheric air, natural convection over the cold walls of the container drives the flow inside the trailer. This phenomena was observed roughly when the inside air has reached a ceiling temperature of a few kelvins below the external temperature. Afterwards, quasi-steady state heat transfer was observed until the doors were closed.

Lafaye de Micheaux et *al.* [60] and Croquer et *al.* [4] have calculated infiltration rate as:

$$\dot{I} = \iint v_n \, \mathrm{d}A_{door,infiltration} \tag{2.25}$$

where v_n is the velocity component normal to the doorway, ρ_{da} the density of dry air, h_{da} the enthalpy of dry air, ρ_{va} the density of water vapour, and h_{va} the enthalpy of water vapour.

At $t = 10\,\mathrm{s}$ after the door opening (Figure 2.10), flat temperature profiles are observed for the upper part ($y/H \approx 0.4$ to $y/H = 1$) and the lower part ($y/H = 0$ to $y/H \approx 0.4$) of the doorway [4; 60]. At approximately $y = \frac{H}{3}$, transition between the profiles is sudden, representing the "neutral level" observed for the refrigerated chamber [50]. Also for the velocity profile, the two peaks of velocity magnitudes are observed at the ceiling and the floor of the trailer with minimum obtained at the neutral level [60; 4].

Thèse accessible à l'adresse : https://theses.insa-lyon.fr/publication/2024ISAL0034/these.pdf © [J. Jeong], [2024], INSA Lyon, tous droits réservés

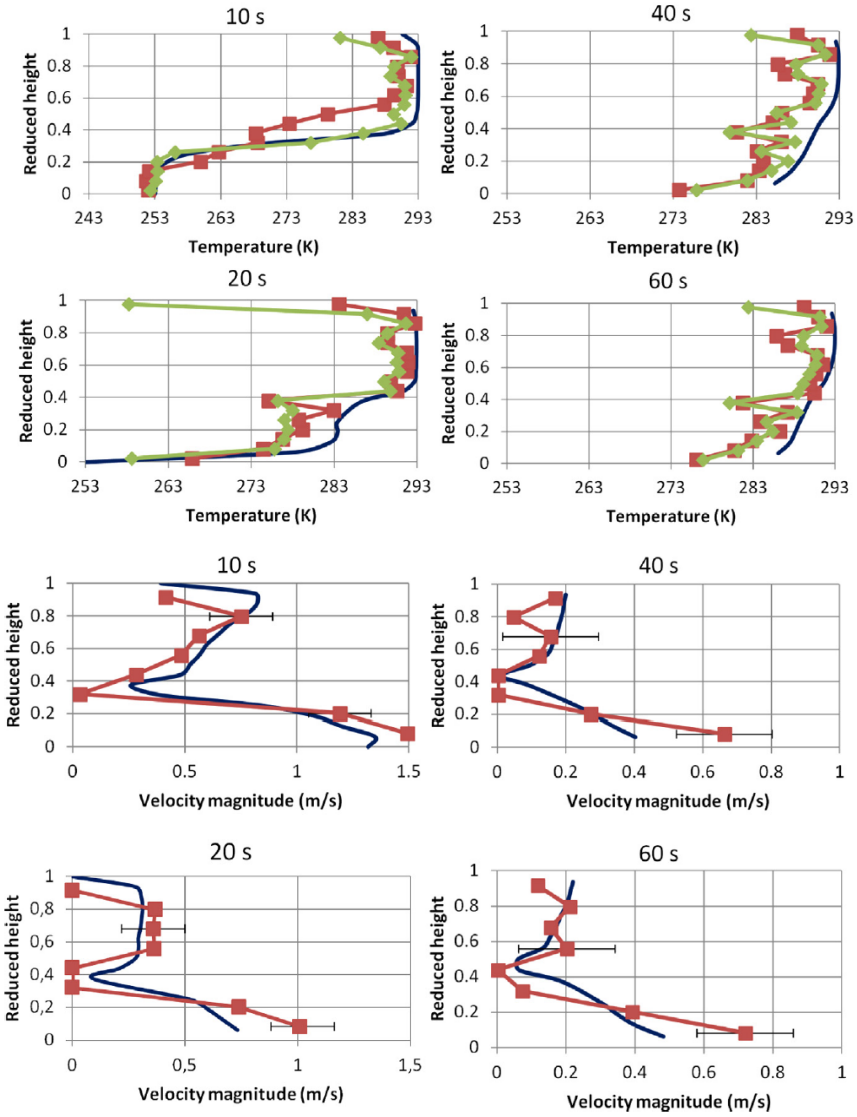

Figure 2.10: The temperature and velocity profiles at the truck trailer door vertical centerline [60].

At $t = 20\,\mathrm{s}$, temperature profiles remain the same above the neutral level. Below the neutral level, temperature has increased but maintains its flat profile while the region close to the floor keeps its initial temperature. This temperature change occurs as the outside air mixes with the inside air that stays in the truck. For the velocity profile, upper region shows a flat profile while the lower region retain its profile. The magnitude of the velocity decreased throughout the doorway and the neutral point remains at the same height. The change in the profile of the upper region may be due to the outside air being sucked into the truck trailer after the renewal of the inside air [60]

At $t = 40\,\mathrm{s}$, temperature profile no longer exhibits distinguishable neutral level and an increasing profile along the door opening from the floor to the ceiling can be observed (Figure 2.9). Generally decreased velocity magnitudes and increased temperatures are observed along the doorway. Finally, at $t = 60\,\mathrm{s}$, the temperature and velocity profiles are almost identical to the ones at 40 s, indicating quasi-state has been reached.

Importantly, both Lafaye de Micheaux et *al.* [60] and Croquer et *al.* [4] numerically demonstrated that the 3D features of the flow does not significantly influence the tempera-

Thèse accessible à l'adresse : https://theses.insa-lyon.fr/publication/2024ISAL0034/these.pdf © [J. Jeong], [2024], INSA Lyon, tous droits réservés

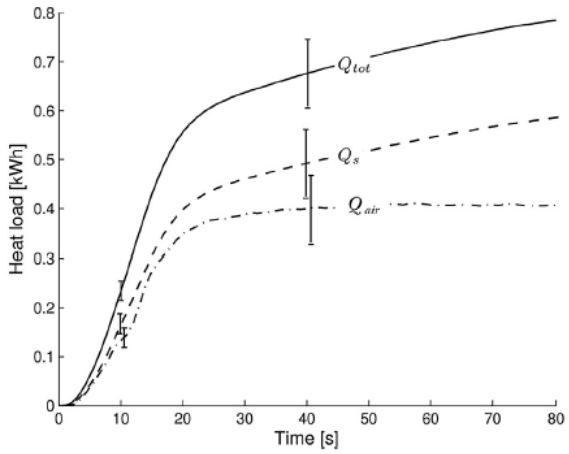

Figure 2.11: Total and sensible infiltration heat loads compared to energy received by the internal air volume [60].

ture and velocity distributions at the midplane of the doorway as presented in Figure 2.10 and Figure 2.9. The greatest difference for the 3D model is attained at the $t = 11\,\mathrm{s}$ to $22\,\mathrm{s}$ period, coinciding with the passing of a large eddy across the door. This is not properly observed from the experimental results of Lafaye de Micheaux et *al.* [60] as the values are averaged over the door centerline, while the 3D results comprise a full integration over the door surface. However, while the 3D model shows in general a better agreement with the experimental data, it does not bring a significant improvement over the results of the 2D models [4].

During the door opening period, the sensible heat load related to the mass interchange is mainly responsible for the temperature increase of the internal air volume [60]. The sensible infiltration load ($\dot{Q_{sens}}$) and the total heat load ($\dot{Q_{total}}$) are obtained by:

$$\dot{Q_{sens}} = \iint v_n \rho_{da} h_{da} \, \mathrm{d}A_{door} \tag{2.26}$$

$$\dot{Q}_{total} = \iint v_n \rho_{da} h_{da} + \frac{v_n + |v_n|}{2} \rho_{va} h_{va} \, \mathrm{d}A_{door} \tag{2.27}$$

where v_n is the velocity normal to the doorway, ρ_{da} the density of dry air, h_{da} the enthalpy of dry air, ρ_{va} the density of water vapour, and h_{va} the enthalpy of water vapour.

From Figure 2.11, the discrepancies between $\dot{Q}_{total}$ and $\dot{Q_{sens}}$ were deemed insignificant as the uncertainty ranges overlap [60]. Therefore, latent heat load analysis and predictions were not considered by Lafaye de Micheaux et *al.* [60].

In recent years, various researchers experimentally and numerically investigated the heat and mass transfers inside a refrigerated truck trailer. Table 2.4 presents the summary of the recent studies investigating the performance of refrigerated vehicles, focusing on the experimental and CFD approaches.

For the experimental approaches, heat and mass transfers inside a truck trailer with deployment of air curtains and varying aperture door openings were investigated by the researchers [61; 62; 60]. Tso et *al.* [61] experimentally investigated the influence of air, fan and plastic strip air curtains for a $7.2\,\mathrm{m}^3$ refrigerated truck body with an opening of $0.9\,\mathrm{m}^2$, subjected to the typical conditions encountered in Singapore. The deployment of an air curtain saved up to 40 % and 11 % of energy compared to cases without an air

Thèse accessible à l'adresse : https://theses.insa-lyon.fr/publication/2024ISAL0034/these.pdf © [J. Jeong], [2024], INSA Lyon, tous droits réservés

Author(s)	Cargo	Turbulence Model	Door	Mesh & Volume	Wall function
Tso et $al.$ [61]		Experimental	*	$V = 7.2\,\mathrm{m}^3$	
Clavier et $al.$ [62]		Experimental	*		
Moureh et $al.$ [63]	*	Experimental & RSM		$V = 81.8\,\mathrm{m}^3$ $749,632$ cells	High $y+$, Log-law
Moureh et $al.$ [64]	*	RSM		$V = 81.8\,\mathrm{m}^3$ $749,632$ cells	High $y+$, Log-law
Lafaye de Micheaux et $al.$ [60]		Experimental, Realizable $k-\epsilon$	*	Unstructured polyhedral $V = 32.4\,\mathrm{m}^3$ $21,000$ cells	High $y+$, Log-law
Rai et $al.$ [65; 66]	*	SST $k-\epsilon$	*	Structured hexagonal $V = 44.2\,\mathrm{m}^3$ 6.1 million cells 4.6 million cells	Standard
Getahun et $al.$ [67]	*	SST $k-\omega$		$V = 86.3\,\mathrm{m}^3$ 16 million cells	Low $y+$, Low-Re
Jara et $al.$ [68]		SST $k-\omega$		Triangular $V = 8.2\,\mathrm{m}^3$ $222,463$ cells	Low $y+$, Low-Re
Croquer et $al.$ [4]		SST $k-\omega$	*	Unstructured triangular $A = 19.2\,\mathrm{m}^2$ $903,084$ cells	Low $y+$, Low-Re
Bonaventure et $al.$ [51]	*	SST $k-\omega$	*	Unstructured triangular $A = 19.2\,\mathrm{m}^2$ $903,084$ cells	Low $y+$, Low-Re

Table 2.4: Summary of recent studies focusing on the performance of refrigerated vehicles. Symbol: * Cargo present/Door openings.

Thèse accessible à l'adresse : https://theses.insa-lyon.fr/publication/2024ISAL0034/these.pdf © [J. Jeong], [2024], INSA Lyon, tous droits réservés

curtain and with a plastic strip curtain, respectively. Clavier et *al.* [62] experimentally investigated the infiltration through the doorway for a medium-size refrigerated truck trailer placed in a wind tunnel and compared the heat load with and without two types of air curtain. They observed an average infiltration heat load of approximately 5.7 kW for an unprotected door with an opening time of 18 min. Lafaye de Micheaux et *al.* [60] numerically and experimentally investigated the velocity and temperature distributions in a truck trailer with an inner volume of 32 m^3 for full, 2/3 lateral, 1/3 lateral and 1/3 central aperture door openings. Their findings are presented in Section 2.4.2.

For the numerical approaches, many researchers investigated the heat and mass transfer inside a refrigerated truck trailer with CFD to overcome many restrictions in experiments, such as manpower, material and time requirements [63; 64; 65; 66; 60; 67; 68; 4; 51]. Moureh et *al.* [63; 64], Getahun et *al.* [67] and Jara et *al.* [68] numerically investigated the airflow patterns and temperature distributions inside a refrigerated vehicle with and without cargo for the closed configuration. Moureh et *al.* [63; 64] developed the model by using FLUENT and second-moment closure with the Reynolds Stress Model (RSM) for a truck trailer with an inner volume of 81.795 m^3 containing 32 polystyrene slotted boxes (1.728 m^3) treated as a porous medium. By deploying air ducts on airflow above the load, better diffusion of injected air along the container was observed. As the recirculating structure located in the inlet area was split into three distinct structures with less intensity by the air ducts, better aerodynamic deployment for each inlet jet, thus more homogeneity of ventilation within the entire trailer was observed. Getahun et *al.* [67] modeled a reefer with an inner volume of 86.3 m^3 containing 20 pallets each holding 768 kg of apple fruit by using FLUENT and calculating the turbulence by using $k-\omega$ Shear Stress Transport (SST) model. They observed monotonous decrease in the airflow from the inlet side to the door side, dropping by 50 % between the first pallet to the middle of the trailer and by 42 % between the middle of the trailer and the last pallet located near the doorway. Jara et *al.* [68] investigated the internal temperature distribution and the airflow patterns without any load with an inner volume of 8.16 m^3 by using CFX with $k-\omega$ SST model to solve for the turbulence. The maximum temperature deviation of 0.43 °C at the air outlet of the system was observed compared to the experimental results.

For the open configuration, Lafaye de Micheaux et *al.* [60], Rai et *al.* [65; 66], Croquer et *al.* [4] and Bonaventure et *al.* [51] investigated the heat and mass transfer across the doorway. Lafaye de Micheaux et *al.* [60] numerically investigated the velocity and temperature distributions in a truck trailer with an inner volume of 32 m^3 with full, 2/3 lateral, 1/3 lateral and 1/3 central aperture door opening areas. They used STAR CCM+ with realizable $k-\epsilon$ SST turbulence model. Rai et *al.* [65; 66] investigated the performance of an air curtain for a 44.2 m^3 refrigerated truck trailer using FLUENT with a 3D standard $k-\epsilon$ SST model. They considered door opening period of 15 min and trailer configurations with and without cargo. Similar to Lafaye de Micheaux et *al.* [60], natural infiltration was found to be the main cause of cold air flowing out from the lower part of the door. An air curtain at an optimum averaged velocity of 3.1 $m\,s^{-1}$ placed inside the trailer resulted in the reduction of energy consumption by 48 %. Croquer et *al.* [4] developed a preliminary CFD model using CFX with $k-\omega$ SST model for a truck trailer equipped with three eutectic plates placed in parallel at the back of the trailer. Their $k-\omega$ turbulence model demonstrated slight improvement to the predictions of the realizable $k-\epsilon$ model of Lafaye de Micheaux et *al.* [60]. They also optimized the interplate distance of the eutectic plates and the geometry of the separating wall. For the loading region of the trailer, an interplate distance of 0.06 m resulted in the lowest average

Thèse accessible à l'adresse : https://theses.insa-lyon.fr/publication/2024ISAL0034/these.pdf © [J. Jeong], [2024], INSA Lyon, tous droits réservés

temperature over the cargo loading region compared to cases with an interplate distance of 0.036 m and 0.10 m. Their work was extended later by Bonaventure et *al.* [51] for the cases with the plates placed in series at the roof of the trailer and for a configuration with cargo.

2.5 Conclusion

The literature review encompasses the latest knowledge, methods, and techniques related to the various aspects of the research. It explores the potential of PCM systems to replace conventional refrigeration units on a refrigerated truck trailer that rely on fossil fuels. Moreover, it discusses the physical phenomena associated with sub-zero eutectic systems, such as the solidification and melting of PCM and the formation of frost on the eutectic system. Advanced numerical models in this field are also presented. Finally, considering the manuscript's focus on the application of eutectic systems in refrigerated truck trailers, the thermoaeraulic behavior of the air during the door opening period is examined and discussed.

Thèse accessible à l'adresse : https://theses.insa-lyon.fr/publication/2024ISAL0034/these.pdf © [J. Jeong], [2024], INSA Lyon, tous droits réservés

Chapter 3

Infiltration Model

To investigate the feasibility of the eutectic system for a refrigerated food transport system, it is foremost important to accurately predict the thermoaeraulic behavior of the air during the infiltration (door-opening) period. This chapter presents the obtained results submitted in *Applied Thermal Engineering* and presented during the 18^{th} *International Refrigeration and Air Conditioning Conference* held at Purdue University, Lafayette, United States.

3.1 Numerical modeling

In the following section, the geometrical configuration is first described in detail. The numerical methodology (algorithms, numerical schemes) as well as the numerical parameters, including the mesh grid and the boundary conditions are then presented.

3.1.1 Geometrical modeling

The computational domain is a truck trailer of length 7.13 m and height 2.62 m. The refrigeration system includes three eutectic plates of thickness 0.054 m and height/length 1.76 m and fans, which maintain the air circulation through the plates and the container when the doors are closed. Figure 3.1a displays the two configurations assessed here: plates placed vertically in parallel at the back of the trailer (Configuration A) and plates in series located at the roof (Configuration B). For each configuration, two air circulation modes are employed, namely the blowing and suction modes. For the blowing mode, air is blown out from the plate region to the trailer and for the suction mode, air is sucked into the plate region. The truck trailer is placed in a wind tunnel of length 31 m and height 5.43 m maintained at 293 K with a zero velocity field (Fig.3.1b). The wind tunnel is large enough that its impact on the infiltration behavior is negligible. However, some interactions between the doorway of the truck trailer and the floor of the wind tunnel are expected.

The plates are maintained at 244 K, which corresponds to the melting point of a typical sodium-chloride mixture as phase change material (PCM). The plates have been designed such that the system can operate during a whole working day of 8 hours. During this time, the PCM is not fully melted. The assumption of a constant temperature for the plates is assumed to be valid as it is a mixture of solid and liquid in thermal equilibrium. The wall that separates the eutectic plates from the loading area of the trailer is 1.81 m in length and 0.01 m in thickness for Configuration A and 5.45 m in length and 0.01 m in

Thèse accessible à l'adresse : https://theses.insa-lyon.fr/publication/2024ISAL0034/these.pdf © [J. Jeong], [2024], INSA Lyon, tous droits réservés

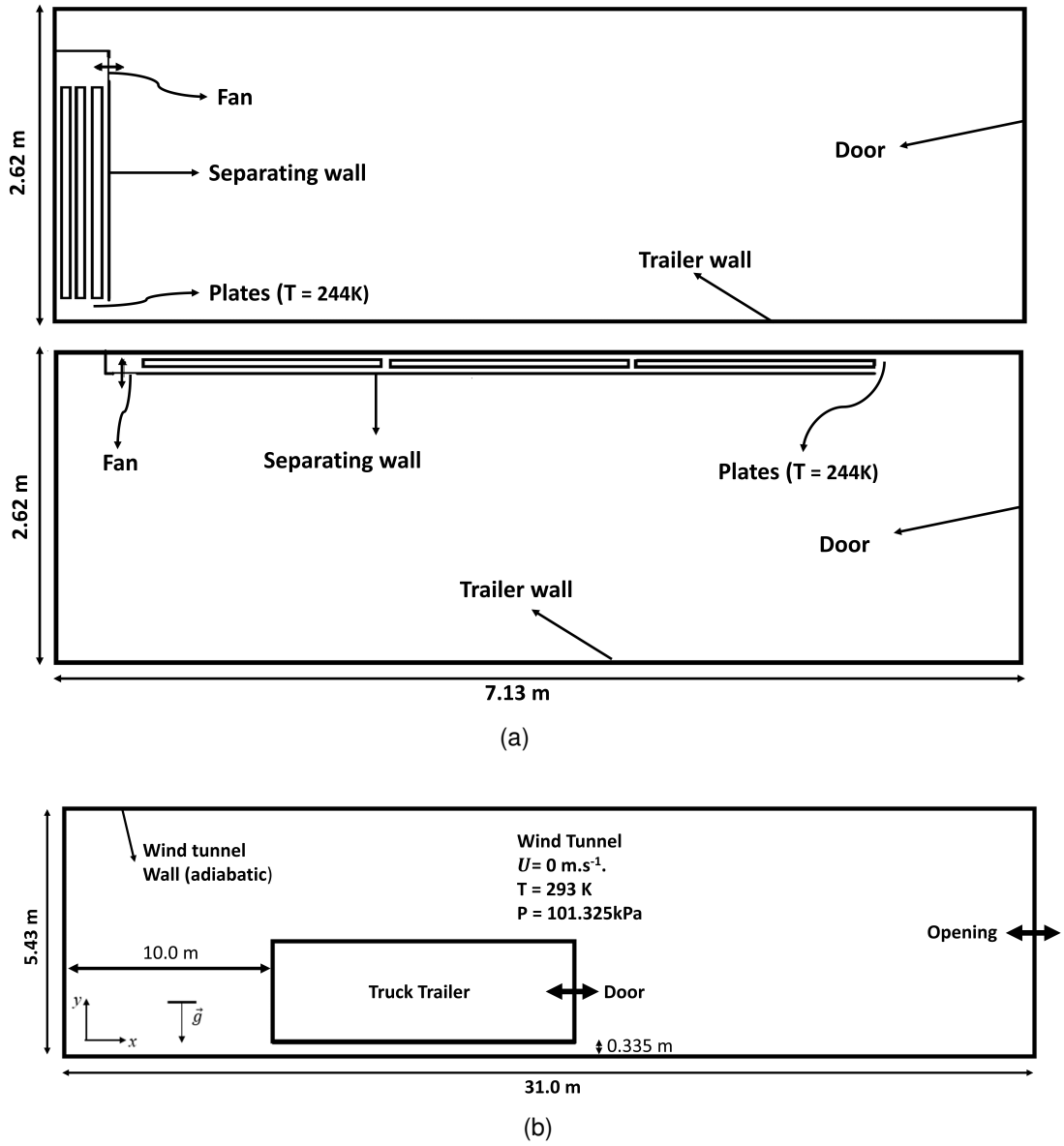

Figure 3.1: (a) Trailer diagram with the position of the eutectic plates for Configuration A (top) and Configuration B (bottom); (b) General schematics of the computational domain with the relevant boundary conditions.

thickness for Configuration B. For both configurations, a distance of 0.06 m is maintained between the wall and the plates based on the former results of Croquer et *al*. [4].

Figure 3.2 shows the details of the optimized plate system design obtained by Croquer et *al*. [4]. The dimensions, which are based on commercially available plates and truck container models, are summarized in Table 3.1. The inter plate spacing is set to 0.06 m as for the distance between the plates and the walls.

3.1.2 Numerical method

The conservation equations for mass, momentum and energy are solved using the finite-volume method. Second-order upwind and centered schemes are preferred respectively for the spatial discretization of the advection and diffusion terms, while a second-order

Thèse accessible à l'adresse : https://theses.insa-lyon.fr/publication/2024ISAL0034/these.pdf © [J. Jeong], [2024], INSA Lyon, tous droits réservés

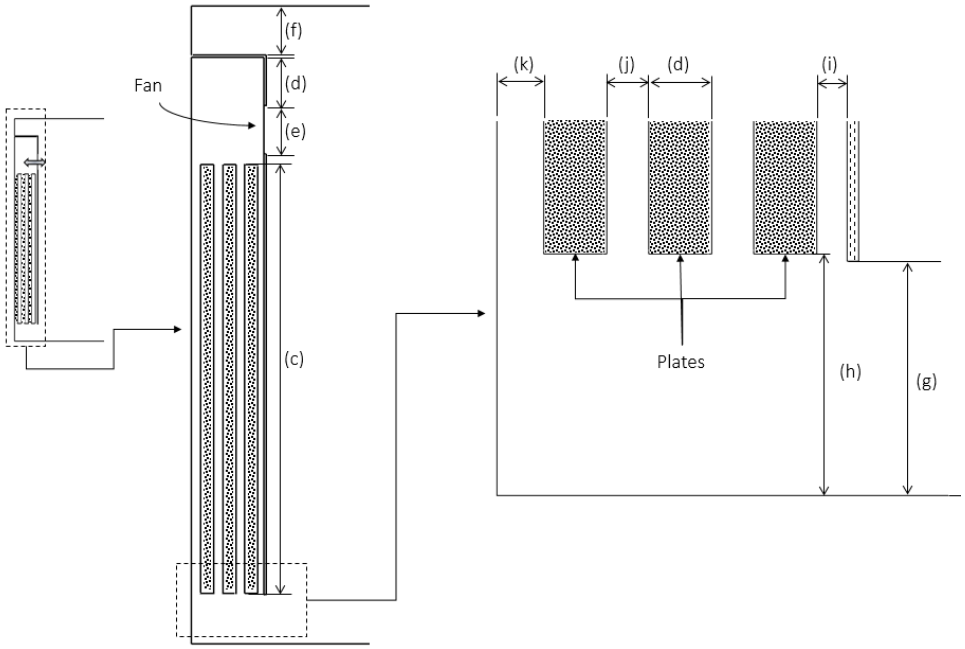

Figure 3.2: Details and dimensions of the eutectic plates.

Feature	**Distance [m]**
Container length (a)	7.13
Container height (b)	2.62
Plate thickness (c)	0.054
Plate height (d)	1.76
(e), (f), (g), (h)	0.2, 0.345, 0.2, 0.206
(i), (j), (k)	0.06, 0.06, 0.06

Table 3.1: Container and eutectic plate dimensions.

Backward-Euler scheme with implicit time-stepping is used for the temporal discretization. The pressure-velocity coupling is overcome using a Rhie-Chow fourth-order algorithm.

The flow field is modeled by solving the (un)steady-state Reynolds Averaged Navier-Stokes equations (URANS) including the thermal energy equation, as the kinetic energy effects are negligible. Buoyancy air-driven flows with a maximum temperature difference of 29 K are expected, therefore air may be assumed to behave as an ideal gas with variable density and constant transport properties and the Boussinesq model accounts for the density change [69]. Turbulence effects are modeled using the Shear Stress Transport k-ω model developed by Menter [70] with production terms representing buoyancy contributions to the turbulent field. The k-ω SST model applies the robust k-ϵ formulation in the free turbulence regions and the more near-wall accurate k-ω model within the boundary layers, depending on a wall-distance weighted function. All calculations are performed using the commercial software *CFX ANSYS.v19*.

Thèse accessible à l'adresse : https://theses.insa-lyon.fr/publication/2024ISAL0034/these.pdf © [J. Jeong], [2024], INSA Lyon, tous droits réservés

3.1.3 Numerical parameters

Unstructured meshes of triangular (resp. tetrahedral) elements are generated for the spatial discretization of the 2D (resp. 3D) domain, with a minimum of 10 prismatic layers close to all solid boundaries with a growth rate set to 1.1 as well as local refinement in the door interface region. To perform 2D simulations on *CFX ANSYS.v19*, the 2D mesh was extruded in the normal direction by two elements for a total thickness of 0.02 m. Translational periodic boundary conditions are imposed on both faces of the extrusion. A mesh-sensitivity analysis was carried out in the 2D configuration to determine the minimum element size. A mesh grid composed of about $\sim 9.0 \times 10^5$ elements has proven to provide grid-independent results while guaranteeing a maximum dimensionless wall coordinate y^+ always lower than 1, a prerequisite for the use of a low-Reynolds number approach. Details of these mesh grids are displayed in Figure 3.3. A symmetry condition is imposed at the mid-plane of the 3D case to reduce the computational cost. For 3D cases, the mesh grid is composed of $\sim 1.3 \times 10^7$ elements.

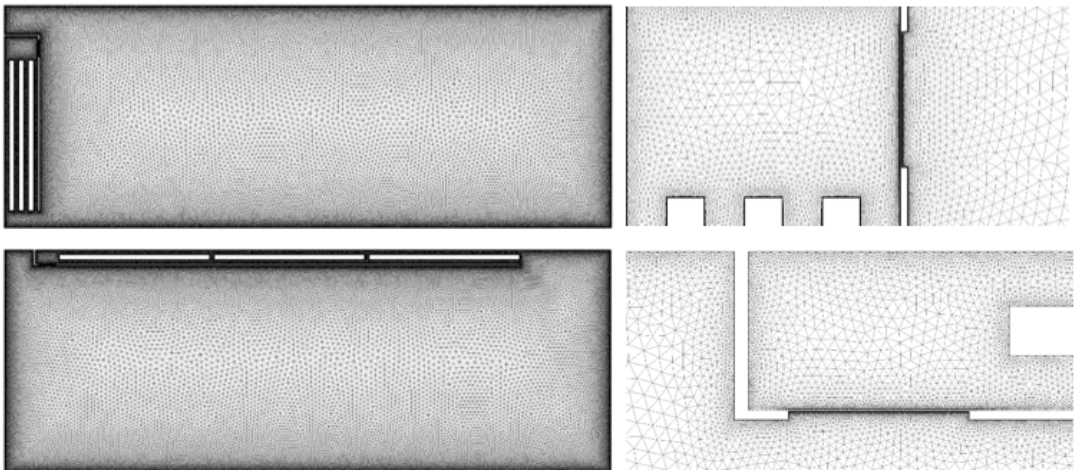

Figure 3.3: Overview of the mesh grids for Configuration A (top) and Configuration B (bottom) with a focus on the fan and the plate regions on the right.

Steady-state calculations are performed on a 2D domain as shown in Figure 3.3. An overall external heat transfer coefficient $E = 0.4\,\mathrm{W\,m^{-2}K^{-1}}$ corresponding to a heavily insulated equipment is imposed on the external walls [51], with an outside atmospheric temperature of 293 K to model thermal resistance of the walls and the air outside trailer computational domain. The separating wall is made of polypropylene with a thermal conductivity of $1.4 \times 10^{-4}\,\mathrm{W\,m^{-1}K^{-1}}$ and a specific heat of $1800\,\mathrm{J\,kg^{-1}K^{-1}}$. Regarding the ventilation system, the need for accurately modeling the fans is avoided by inserting a source term in the momentum equation over a surface representing the fan diameter of 0.2 m , such that the air passing through the fans is accelerated to an averaged horizontal velocity of $8.4\,\mathrm{m\,s^{-1}}$ in a prescribed direction. Hoang et *al.* [71] modeled also the fans through a source term in the momentum equation but based on a quadratic law giving the pressure losses overcome by the fan as a function of the superficial velocity. The steady-state calculations are initialized with a constant pressure of 101.325 kPa, an initial temperature of 253 K and a zero-velocity field ($\vec{V_0} = \vec{0}\ \mathrm{m\,s^{-1}}$).

For the transient simulations during the door opening period, the truck trailer is placed inside the wind tunnel displayed in Figure 3.1. All wind tunnel walls are assumed to be adiabatic with an opening boundary condition in CFX imposed on the rightmost

Thèse accessible à l'adresse : https://theses.insa-lyon.fr/publication/2024ISAL0034/these.pdf © [J. Jeong], [2024], INSA Lyon, tous droits réservés

surface, with $T_{opening} = 293$ K and $P_{opening} = 101.325\ kPa$. The direction of the flow is specified to be normal to the boundary condition and the magnitude of the velocity is solved as a part of the solution. The trailer is located 10.0 m away from the leftmost wind tunnel wall and 0.335 m above the floor of the wind tunnel. A wall equivalent thermal resistance of $1.84\,\mathrm{m^2\,K\,W^{-1}}$ is used to model the heat flux through the trailer walls. The initial conditions of the wind tunnel are fixed to be 101.325 kPa, 293 K and $0\,\mathrm{ms^{-1}}$ at $t = 0$ s. For the transient simulations, results from the steady-state simulations with the corresponding operating mode and configuration are used to initialize the flow field inside the trailer. Instantaneous door opening is assumed at $t = 0$ s and the fans are turned off. An adaptive time-step approach is adopted with 3 to 5 target inner-loop iterations and initial and maximum time steps equal to of 10^{-7} and 10^{-2} s, respectively. The convergence criteria for mass, momentum and energy RMS residual levelss RMS are fixed under 10^{-4}. This results in a typical time step of about 5×10^{-3} s. Simulations are performed using the HPC facilities of Calcul Québec using 20 to 40 CPU nodes with 12 *AMD Opteron 6172* cores 32 GB RAM per node.

3.2 Validation of the numerical model

In order to determine the optimal numerical setup offering good accuracy at the lowest computational cost, a preliminary benchmark is carried out involving two aspects: (i) 3D domain vs. 2D domain and (ii) heat conducting vs. adiabatic container walls. The present numerical model is validated against the experimental and numerical data of Lafaye de Micheaux et *al.* [60], which provided temperature and velocity profiles of the air flow inside an empty truck trailer without the eutectic plates. The configuration is shown in Figure 3.1. Its inner dimensions are $2.35 \times 2.5 \times 5.51$ m. It is placed midway in a tunnel of $5.43 \times 5.5 \times 31$ m at a distance of 0.35 m from the floor. In the baseline experiment, the container and wind tunnel initial temperatures were respectively 253 K and 293 K. At $t = 0$ s, the container door was fully opened, and velocity and temperature measurements inside the container and at the door were logged for about 60 s and compared to the results obtained by the model of Lafaye de Micheaux et *al.* [60].

Unstructured meshes of triangular (resp.tetrahedral) elements are generated as described in Section 3.1.3. It results in mesh grids composed $\sim 1.46 \times 10^5$ and $\sim 1.34 \times 10^7$ elements for the 2D and 3D configurations, respectively. The boundary conditions are similar to the case with the eutectic plates (Fig.3.1b). The container walls are assumed to be either adiabatic or allowing for heat conduction with a wall equivalent thermal resistance of $1.84\,\mathrm{m^2\,K\,W^{-1}}$, value based on typical refrigerated container insulation layers [4]. Thus one could compare the results against the regulatory requirements [2]. A general-connection interface is set at the container door to connect the meshes across the doorway and allow for the air to enter and exit through the interface and a symmetry condition is imposed at the mid-plane of the 3D case to reduce the computational cost.

For the benchmark study, three numerical configurations are considered: (i) 3D domain without heat transfer, (ii) 2D domain with heat conduction through the container walls and (iii) 2D domain with adiabatic walls. A comparison of the door velocity profiles at $t = 10$ s, 20 s, 40 s and 60 s after the door opening is shown in Figure 3.4. A good general agreement is observed in terms of both the instantaneous shape profiles and their temporal evolution. The 3D numerical setup seems to better fit the experimental data, in particular at $t = 10$ s and $t = 40$ s, nonetheless both 2D approaches show good accuracy and even a better capture of the velocity profile at $t = 60$ s.

Thèse accessible à l'adresse : https://theses.insa-lyon.fr/publication/2024ISAL0034/these.pdf © [J. Jeong], [2024], INSA Lyon, tous droits réservés

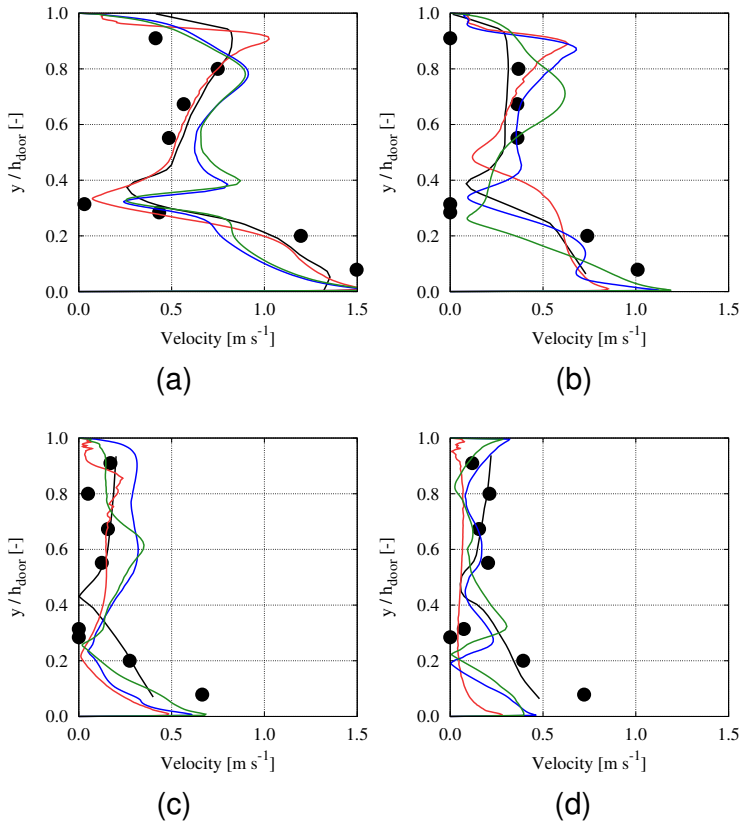

Figure 3.4: Comparison of the velocity magnitude profiles at the container door vertical centerline between the present simulations and the published data of Lafaye de Micheaux et $al.$ [60] at (a) $t = 10\,\mathrm{s}$, (b) $20\,\mathrm{s}$, (c) $40\,\mathrm{s}$ and (d) $60\,\mathrm{s}$. Legend: • Experiment - Lafaye de Micheaux et $al.$ [60], — CFD - Lafaye de Micheaux et $al.$ [60], — CFD 3D, — CFD 2D with no heat transfer, — CFD 2D with heat transfer.

Figure 3.5 compares the door temperature profiles for the same conditions described above. At $t = 10$ s, the air flow is yet in an early stage not far from the initial step profile, therefore no conclusive differences are seen. Nonetheless as the time passes, the profiles evolve into a curved shape with a maximum temperature of about 289 K, which all numerical approaches seem to over predict by about 1 K. At $t = 20$ s and $t = 40$ s, both 2D setups fail to fully replicate the experimental profile at the lower section ($y/H_{door} \sim 0.2$), this is particularly noticeable in the adiabatic walls setup at $t = 20$ s. Nonetheless the differences are of the same range as the dispersion of the experimental data. Deviations are also observed in the near-wall regions, particularly for $y/H_{door} \to 1$, where the numerical models predict a constant wall temperature of 293 K whereas the experimental data reveal an important temperature gradient. The temperature gradient at the bottom is well captured, specially by the 2D models.

The numerical results showed a recirculation located at the door region which leads to turbulent fluctuations. The instantaneous profiles of Figures 3.4 and 3.5 show differences between the numerical and experimental results. This scattering might be attributed to the natural turbulent fluctuations, thus implying that the three numerical models are quite capable of capturing the main flow features across the door.

Further validation is shown in Figure 3.6 in terms of the infiltration rate. It is defined as the volume flow rate into the trailer across the doorway as follows:

Thèse accessible à l'adresse : https://theses.insa-lyon.fr/publication/2024ISAL0034/these.pdf © [J. Jeong], [2024], INSA Lyon, tous droits réservés

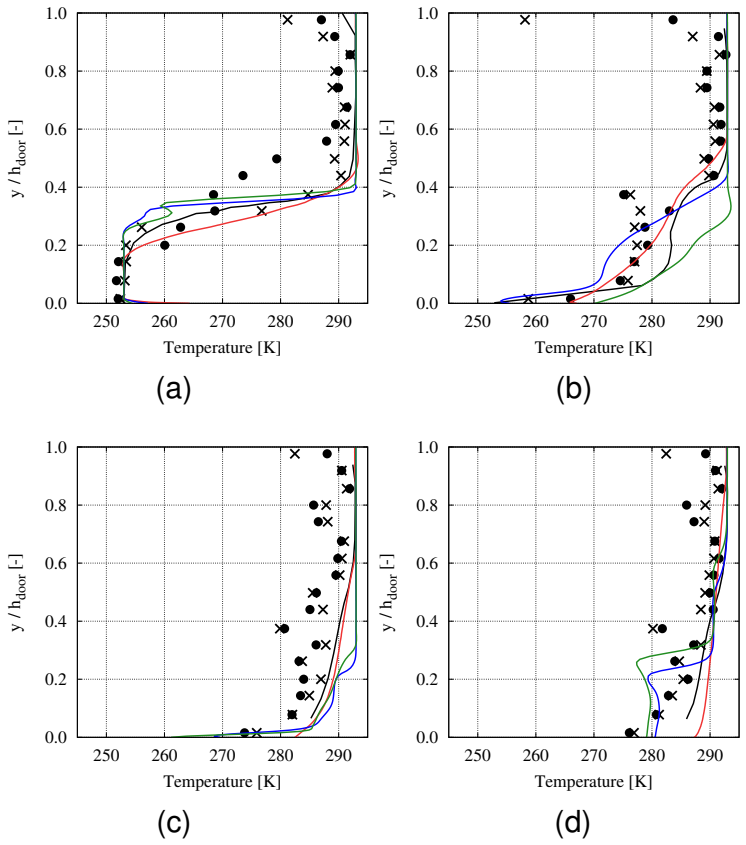

Figure 3.5: Comparison of the temperature profiles at the container door vertical centerline between the present simulations and the published data of Lafaye de Micheaux et $al.$ [60] at (a) $t = 10\,\mathrm{s}$, (b) $20\,\mathrm{s}$, (c) $40\,\mathrm{s}$ and (d) $60\,\mathrm{s}$. Legend: • Experiment 1 - Lafaye de Micheaux et $al.$ [60], Experiment 2 - Lafaye de Micheaux et $al.$ [60], — CFD - Lafaye de Micheaux et $al.$ [60], — CFD 3D, — CFD 2D with no heat transfer, — CFD 2D with heat transfer.

$$\dot{I} = \iint v_n \, \mathrm{d}A_{door,infiltration} \tag{3.1}$$

with v_n the velocity normal to the doorway with the positive direction towards the trailer, and $A_{door,infiltration}$ the area of the doorway occupied by the air infiltrating into the trailer of the doorway. .

In Figure 3.6, the three numerical setups are able to properly capture the main features of the experimental results, in particular the initial flow acceleration and the time needed for reaching the steady state. The greatest difference is attained by the 3D model in the $t = 11\,\mathrm{s}$ to $22\,\mathrm{s}$ period, which coincides with the passing of a large eddy across the door, implying recirculation and thus negative infiltration values for a short period. It is unclear if the experimental procedure properly reports these structures as the reported values are averaged over the door centerline, whereas the 3D results comprise a full integration over the door surface. This would also explain the better fit of the 2D models, which essentially represent the flow across the door vertical centerline.

In conclusion, although the 3D approach shows in general a better agreement with the experimental data, both in terms of velocity and temperature profiles across the door, it does not bring a significant improvement over the results obtained with the 2D models. Inclusion of the heat conduction across the container walls introduces additional complications to the model. However, it has non-negligible effects during an entire delivery

Thèse accessible à l'adresse : https://theses.insa-lyon.fr/publication/2024ISAL0034/these.pdf © [J. Jeong], [2024], INSA Lyon, tous droits réservés

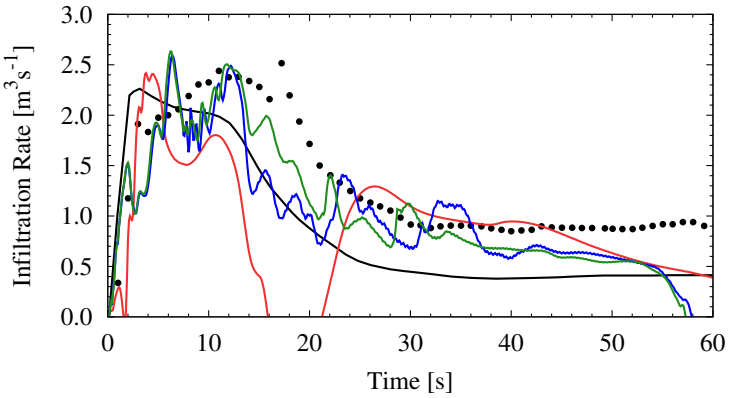

Figure 3.6: Comparison in terms of the infiltration rate at the container door between the present simulations and the experimental and numerical data of Lafaye de Micheaux et $al.$ [60]. Legend: • Experiment 1 - Lafaye de Micheaux et $al.$ [60], — CFD - Lafaye de Micheaux et $al.$ [60], — CFD 3D, — CFD 2D with no heat transfer, — CFD 2D with heat transfer.

cycle and is specified by regulatory bodies [2]. Therefore the 2D model with the heat conduction across the container walls was chosen for modeling the refrigerated container with the eutectic plates.

3.3 Results and discussion

Results are analyzed in this section for the truck container with the eutectic plates described in Section 4.2. Steady-state calculations are initially performed for the two configurations with the plates located at the back (Configuration A) and the roof of the trailer (Configuration B) with two operating modes (Blowing and Suction). The aforementioned configurations are compared without and with a given cargo load. Afterwards, results obtained from the steady-state simulations are imposed as the initial values inside the trailer before the door opening for the transient calculations to investigate the interaction between the developed fluid flow inside the trailer and the outside-infiltrating atmospheric air.

3.3.1 Configurations without cargo

Configurations A and B - suction and blowing modes are first compared for an empty trailer.

Closed trailer without cargo

From the results obtained from the steady-state simulations of Configurations A and B without the cargo, it appears that the temperature distribution inside the trailer is homogeneous with a near-zero velocity zone near the center of the trailer. This is observed in Figure 3.7 for both configurations and fan directions. Slight inhomogeneity of the temperature distribution is observed due to the recirculation zones at each corner of the trailer with the maximum temperature inside the trailer. Table 3.2 reveals that the difference in the plate location and the operating mode has negligible impact on the temperature inside the trailer for the steady-state simulations, as the maximum difference is 0.5 K for the area-averaged temperature over the cargo loading area (excluding the area occupied by

Thèse accessible à l'adresse : https://theses.insa-lyon.fr/publication/2024ISAL0034/these.pdf © [J. Jeong], [2024], INSA Lyon, tous droits réservés

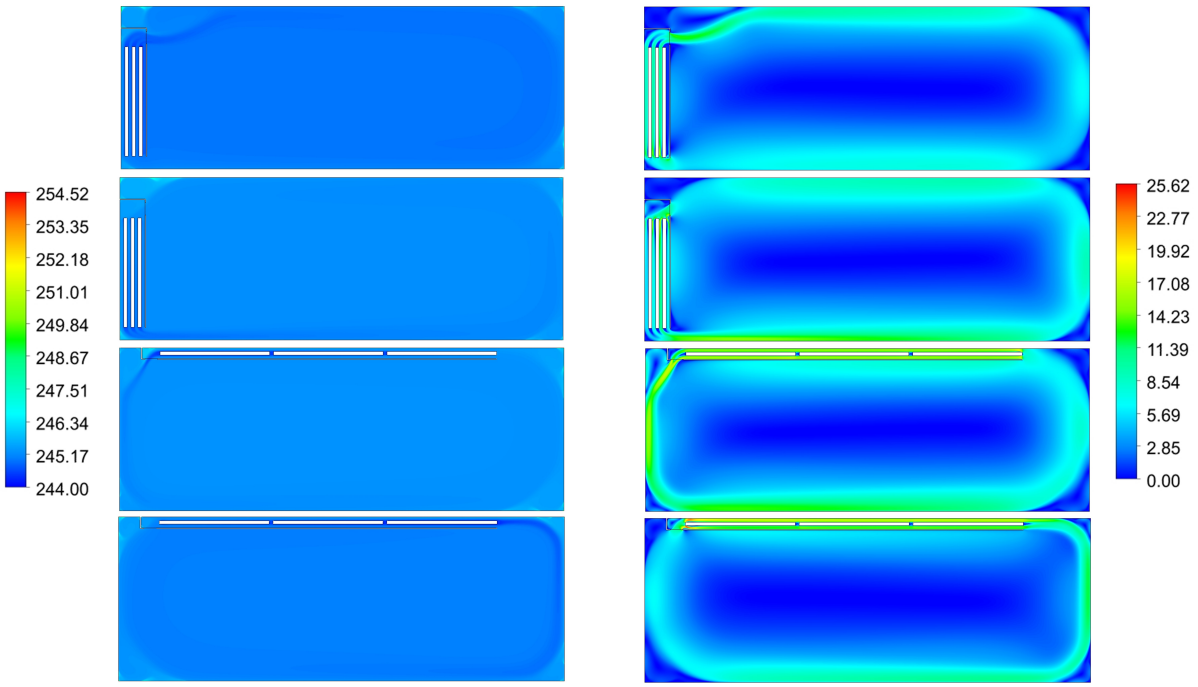

Figure 3.7: (a) Temperature [K] and (b) velocity magnitude [ms^{-1}] contours for Configurations A and B. The blowing mode is always on the top and the suction mode at the bottom.

Configuration	**Maximum temperature** [K]	**Area-averaged temperature** [K]	**Area-averaged velocity** [$\mathrm{m\,s}^{-1}$]
A - blowing	254.5	245.1	3.64
A - suction	252.1	245.6	4.21
B - blowing	253.5	245.4	4.30
B - suction	254.0	245.2	3.33

Table 3.2: Temperature and velocity magnitude obtained from the steady-state simulations.

the eutectic plates). The counterclockwise flow inside the trailer (Configuration A - suction and Configuration B - blowing) results in an overall lower area-averaged temperature and in a higher velocity inside the trailer. For all configurations and operating modes, the maximum temperatures inside the trailer are below the regulated cargo temperature of frozen foodstuffs at 261.15 K and quick (deep) frozen foodstuffs at 255.15 K [2]. Also, the homogeneity of the temperature field inside the cargo loading area respects the regulated maximum temperature difference of 2 K [2].

Also, there are few distinctions that can be observed between each configuration:

1. For Configuration A with the blowing mode (Fig. 3.7), there is no flow between the first plate and the separating wall, effectively reducing the influence of the plate. For Configuration B, all the plates are fully utilized.

2. For Configuration B with the blowing mode, the flow velocity from the plates to

Thèse accessible à l'adresse : https://theses.insa-lyon.fr/publication/2024ISAL0034/these.pdf © [J. Jeong], [2024], INSA Lyon, tous droits réservés

the trailer is reinforced by gravity. On the contrary for the suction mode, the flow being dragged from the bottom of the trailer to the plates is weakened by gravity. Therefore, the highest area-averaged velocity is obtained for Configuration B - blowing mode and the lowest is obtained for Configuration B - suction mode. For Configuration A, gravity similarly reinforces and weakens the strength of the flow for the suction and blowing modes, respectively. However, the influence is weaker as the fans are located closer to the bottom of the trailer.

Door opening period without cargo

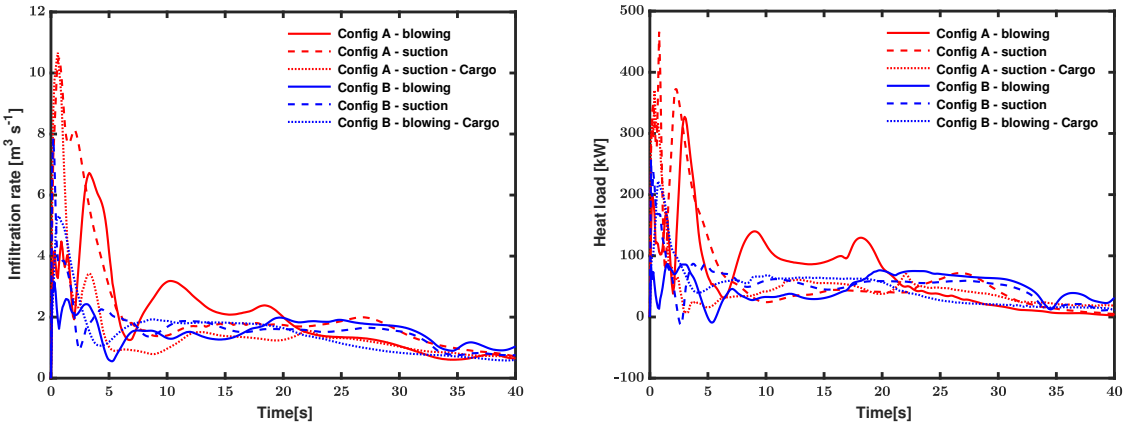

(a) (b)

Figure 3.8: Temporal evolutions of the (a) infiltration rate and (b) heat load through the door for the two configurations and modes.

The infiltration rate ($\dot{I}$) is defined as the volume flow rate of the air infiltrating into the trailer and the heat load ($\dot{Q}$) is defined as the amount of heat exchange occurring through the entire doorway. The calculation of the infiltration rate is defined in Eq. 3.1. The heat load across the doorway is calculated as:

$$\dot{Q} = \iint v_n \frac{P}{RT} c_{p,da}(T - 273)\,\mathrm{d}A_{door} \tag{3.2}$$

where v_n is the velocity normal to the doorway with the positive direction towards the trailer, P the pressure, $R = 287.085\,\mathrm{J\,kg^{-1}\,K^{-1}}$ the specific gas constant of dry air and $c_{p,da} = 1006\,\mathrm{J\,kg^{-1}\,K^{-1}}$ its specific heat. In Eq. 3.2, the reference temperature is chosen as 273 K. Note that the infiltration rate is defined as the volume flow rate into the trailer. However, for the heat load induced through the door, both exfiltration and infiltration through the door are accounted. To obtain the infiltration rate and the heat load across the entire doorway, the 2D values were scaled to that of 2.5 m in width as in Lafaye de Micheaux et *al.* [60] and Croquer et *al.* [4].

The renewal time is defined as the time required by the internal air to be completely renewed [60]. However, it should be noted that the simulations are initialized by a pre-existing flow from the steady-state results before the door opening. Therefore, the infiltration rate does not directly correspond to the amount of pure atmospheric air entering into the trailer. Especially in the first few seconds ($t = 0$ to ≈ 5.0 s) mixing of cold high-velocity air and the hot atmospheric air is prominent near the doorway and can be the

Thèse accessible à l'adresse : https://theses.insa-lyon.fr/publication/2024ISAL0034/these.pdf © [J. Jeong], [2024], INSA Lyon, tous droits réservés

main source of infiltration. For Configuration B (Fig.3.8b) with the blowing and suction modes at $t = 5.3$ s and $t = 2.6$ s respectively, the heat load induced through the door is negative as the exfiltration of high-temperature air occurs due to this interaction. However, it appears that for the majority of the simulation, the heat load induced through the door directly corresponds to the infiltration rate. Therefore, the infiltration rate and the renewal times from Figure 3.8a and Table 3.3 are used as the parameters to determine the performance of the configurations and the operating modes.

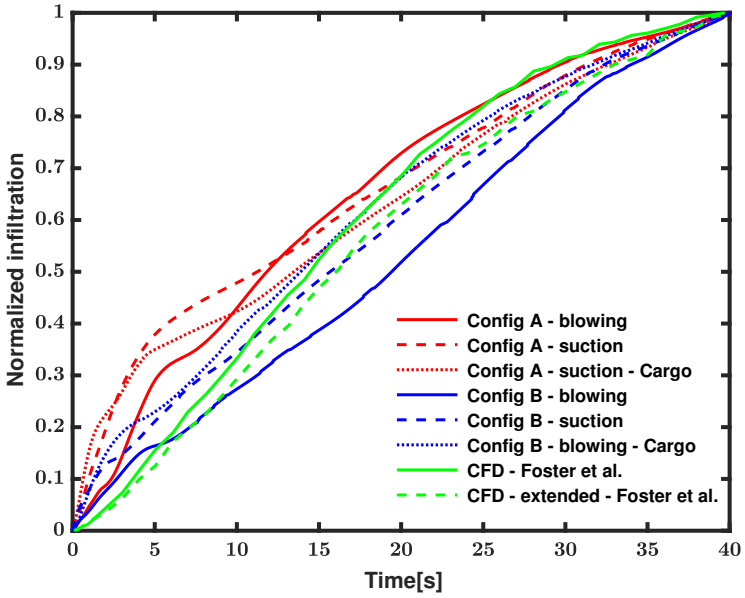

Figure 3.9: Time evolution of the normalized infiltration compared against the CFD results obtained from Foster et *al.* (Extended: extended boundary CFD model) [49].

Foster et *al.* [49] split the infiltration profile into three regions: lag, steady-state, and tail-off regions. The time evolution of the normalized infiltration, normalized by their given values at $t = 40$ s, exhibits comparable profiles (Fig. 3.9). Extended boundary CFD model of Foster et *al.* [49] refers to the model with the extended domain from 3 m to 6 m outside the walls of the modelled cold room [49]. For the lag region, from $t = 0$ to $t = 5$ s, the current model demonstrates higher normalized infiltration gradients at the door vertical centerline as the trailer is initialized with the steady-state results with the pre-existing velocity. In the model of Foster et *al.* [49], the fans were turned off 30 s before the door opening. Otherwise, the current model similarly demonstrates a steady-state region from $t = 5$ to $t = 30$ s with a constant normalized infiltration gradient as the infiltration flow is fully developed. The tail-off region from $t = 30$ to $t = 40$ s demonstrates a decreasing normalized infiltration gradient due to the reduced temperature difference between the air inside the trailer and the outside.

Figure 3.10 shows the temperature at 5 instants and the velocity at $t = 10$ s. At $t = 2.5$ s, the pre-existing flow inside the trailer dominates the flow. Depending on the direction of the rotation of the pre-existing flow inside the trailer, some atmospheric air is dragged into the trailer through the top or bottom regions of the trailer. As infiltration occurs at a relatively high velocity (Fig. 3.8), peak infiltration occurs within this time interval. However, further infiltration and the penetration of the atmospheric air is limited by the exiting flow acting similar to an air curtain investigated by Foster el *al.* [72], Hayes and Stoecker [73], or Tso et *al.* [61].

Thèse accessible à l'adresse : https://theses.insa-lyon.fr/publication/2024ISAL0034/these.pdf © [J. Jeong], [2024], INSA Lyon, tous droits réservés

Configuration	Renewal time [s]	Peak infiltration rate [$m^3\,s^{-1}$]	Peak infiltration time [s]
A - blowing	14.5	6.7	3.3
A - suction	13.0	10.5	0.7
B - blowing	27.7	3.1	0.3
B - suction	24.5	7.9	0.2

Table 3.3: Infiltration data from the transient simulations without cargo.

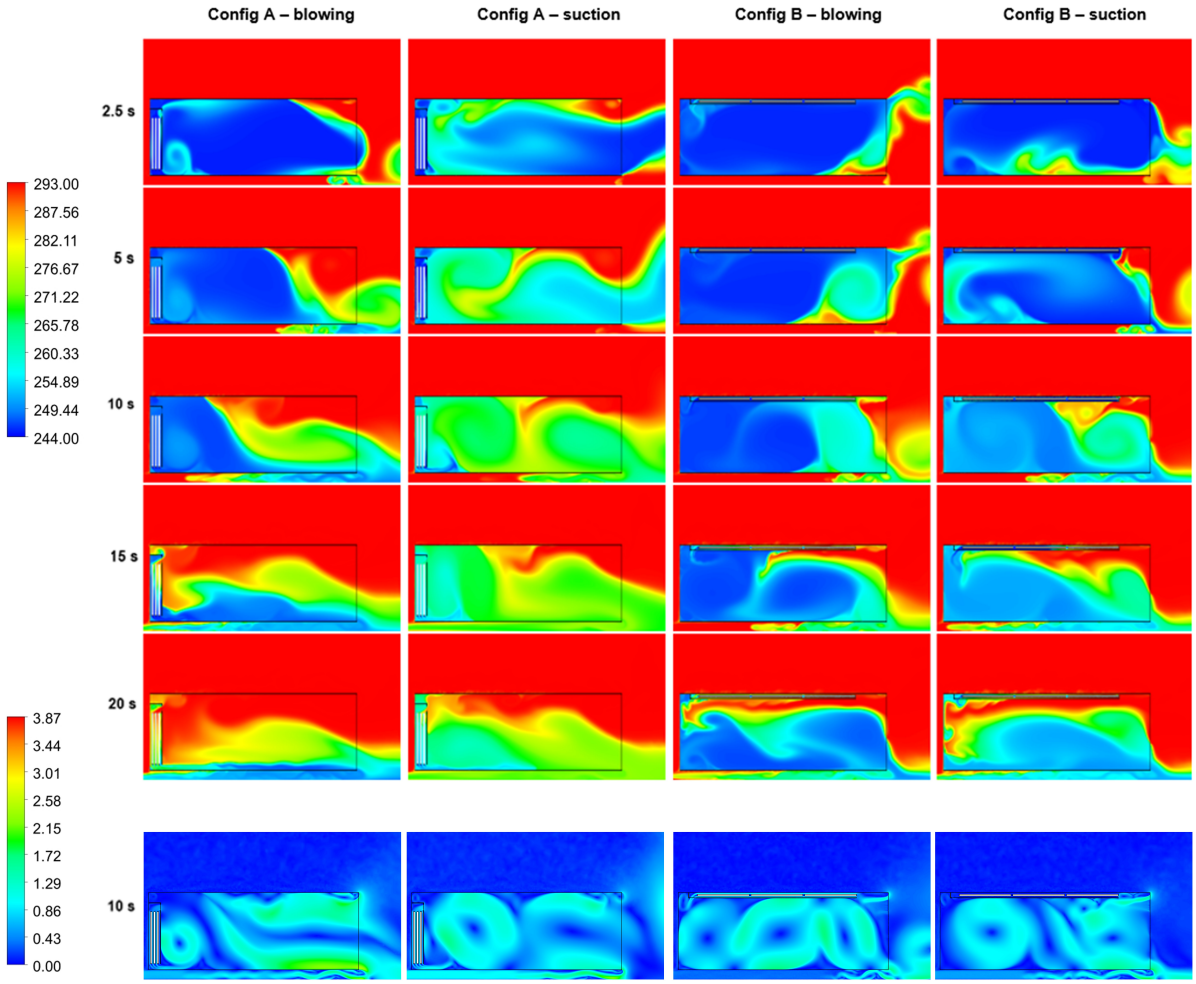

Figure 3.10: (top) Time evolution of the temperature contours [K] for both configurations and fan modes at five instants; (bottom) Corresponding velocity magnitude contours [ms^{-1}] at $t = 10$ s.

At $t = 5$ s, atmospheric air begins to penetrate through the top region of the doorway into the trailer. The flow regime inside the trailer is still largely dominated by the pre-existing flow and its interaction with the incoming atmospheric air. Mixing of hot and cold air is still very prominent near the doorway due to this interaction. For Configuration B with blowing mode, infiltration of the atmospheric air through the top region of the

Thèse accessible à l'adresse : https://theses.insa-lyon.fr/publication/2024ISAL0034/these.pdf © [J. Jeong], [2024], INSA Lyon, tous droits réservés

doorway cannot be observed until $t = 10$ s due to the exfiltration of the cold high-velocity air through the top of the doorway. From $t = 10$ s, further advancement of the hot atmospheric air into the trailer can be observed. However, due to the presence of the recirculation zones created by the pre-existing flow and the atmospheric air dragged into the trailer before $t = 2.5$ s, further advancement of the atmospheric air into the trailer is limited. This effect can be observed until $t = 15$ s and visualized by the velocity contours in Figure 3.10b.

At $t = 20$ s, infiltration of the atmospheric air has reached the back of the trailer as the recirculation zones have diminished. During this time, the flow is mostly driven by buoyancy as the influence of the pre-existing flow progressively diminishes over time. The time evolution of the infiltration rate from Figure 3.8 supports this statement as it is relatively constant until $t = 35$ s. This infiltration dynamics was also observed by Lafaye de Micheaux et *al.* [60] and named "buoyancy driven flow". Moreover, at $t = 35$ s, the infiltration rate decreases slightly as the trailer is now completely filled with the atmospheric air and the infiltration rate is caused solely by the temperature difference in the plate region. This was also observed by Lafaye de Micheaux et *al.* [60] and named as "bounday layer flow."

Table 3.3 and Figure 3.10 show that for either configuration, the operating mode has a minor effect on the renewal time. The blowing mode only takes 11.5% and 13.1% more time to reach the renewal time compared to the suction mode for Configurations A and B, respectively.

However, significant differences are observed between Configurations A and B both from the temperature contours and the time evolution of the infiltration rate. Table 3.10 shows that Configuration B takes 91.0% and 88.5% longer to reach the renewal time compared to Configuration A with the blowing and suction modes, respectively. The main cause of these differences can be seen from the temperature contours in Figure 3.10 from $t = 0$ s to $t = 15$ s. For both operating modes, for Configuration B, infiltration of the atmospheric air is mainly due to the highest velocity of the cold air near the door, where an air curtain behavior is observed. This limit infiltration and significantly increase the renewal times for Configuration B.

3.3.2 Influence of the cargo

Similar simulations are performed for the closed and open situations with the presence of cargo.

Closed configurations with cargo

To identify the influence of the cargo loads on the flow development and infiltration, 5 boxes full of frozen meats are placed in the trailer. The first cargo box is located 0.2 m away from the separating wall and 0.15 m above the floor of the trailer to allow for the flow to pass through between the cargo and the floor of the trailer. Proceeding boxes are separated by 0.1 m from each other. The thermophysical properties of the cargo consisting of frozen meat and cardboard packaging are extracted from Paquette et *al.* [74] and displayed in Table 3.4. Each box is 1 m long and 1.2 m high. Conduction through the boxes is accounted for in the simulations and the initial temperature of the cargo is set to 258 K, as the maximum temperature of the frozen foodstuffs is regulated to be below 260.15 K [2].

Thèse accessible à l'adresse : https://theses.insa-lyon.fr/publication/2024ISAL0034/these.pdf © [J. Jeong], [2024], INSA Lyon, tous droits réservés

Material	Density	Specific heat	Thermal conductivity
	$[\mathrm{kg\,m^{-3}}]$	$[\mathrm{J\,kg^{-1}\,K^{-1}}]$	$[\mathrm{W\,m^{-1}\,K^{-1}}]$
Frozen meat	1050	3000	0.25
Cardboard packaging	276	1700	0.058

Table 3.4: Thermophysical properties of the cargo.

For the transient simulations with cargo, Configuration B - blowing mode was chosen for its better performance in terms of the renewal time and Configuration A - suction mode as a comparison to keep the direction of the pre-existing flow consistent.

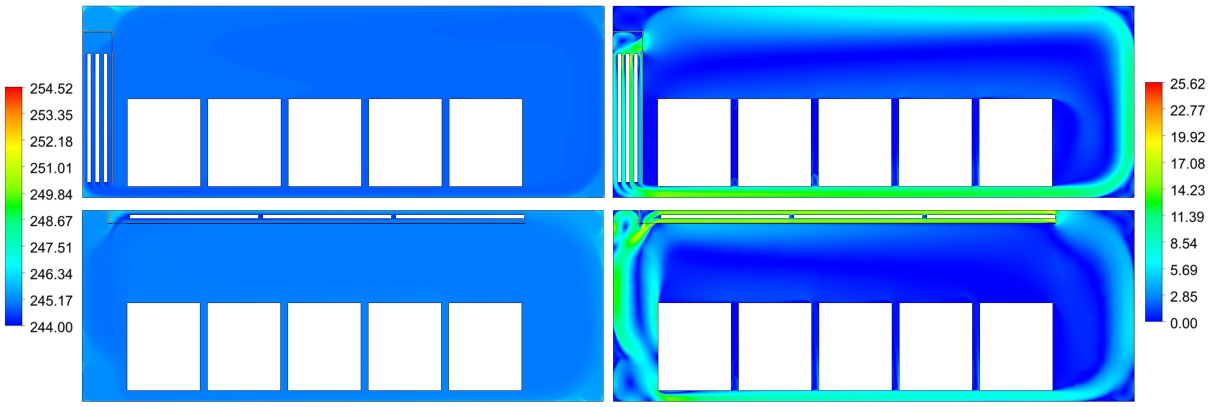

Figure 3.11: (a) Temperature [K] and (b) velocity magnitude $[\mathrm{ms^{-1}}]$ contours of Configuration A with cargo (top) and Configuration B with cargo (bottom).

Similar to Section 3.3.1, the temperature distribution inside the trailer remains relatively homogeneous throughout the entire trailer (Fig. 3.11a). However, the main difference is that for Configuration B, due to the presence of the cargo, the main flow is blocked by the narrow passage between the cargo and the bottom of the trailer. Due to this blockage, a deflection of the flow and a strengthened recirculation zone at the back of the trailer can be observed on Figure 3.11b. Also, the area-averaged velocity for Configuration B is 31.7 % lower than Configuration A. Consequently, the area-averaged temperature inside the trailer for Configuration B is higher than Configuration A by 0.2 K. On the contrary, for Configuration A, the flow from the fan is directly guided into the passage between the floor of the trailer and the cargo boxes, resulting in neither flow blockage nor strengthened recirculation zones. The homogeneity of the temperature distributions and the maximum temperatures observed inside the trailer similarly meets the regulation criteria discussed in Section 3.3.1.

As shown in Table 3.5, temperature inside the cargo is nearly homogeneous with a difference of less than 0.1 K. Similarly, the maximum temperature observed inside the cargo for Configuration A is 0.3 K lower than Configuration B.

Door opening period with cargo

The doors are opened at $t = 0$ s for the delivery of the frozen meat and Configurations A and B are compared in terms of infiltration rate.

Thèse accessible à l'adresse : https://theses.insa-lyon.fr/publication/2024ISAL0034/these.pdf © [J. Jeong], [2024], INSA Lyon, tous droits réservés

Configuration	Area-averaged temperature [K]	Area averaged velocity [$\mathrm{m\,s^{-1}}$]	Maximum cargo temperature [K]	Minimum cargo temperature [K]
A - suction	244.9	3.24	244.9	244.8
B - blowing	245.1	2.46	245.2	245.1

Table 3.5: Temperature and velocity magnitude data from the steady-state simulations with cargo.

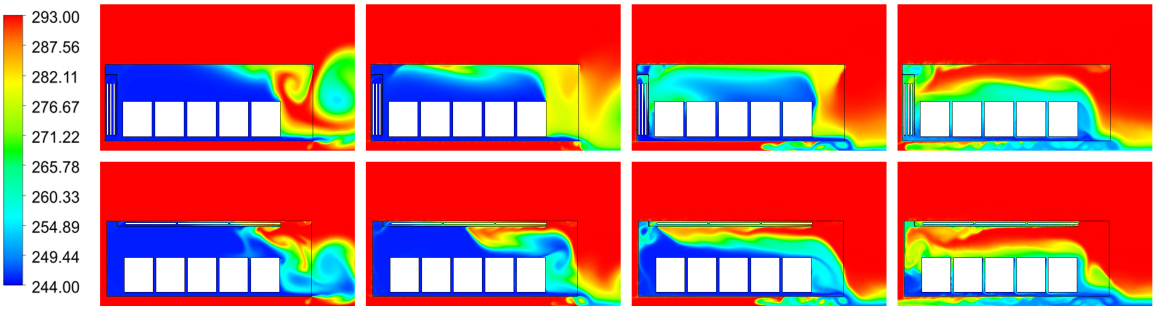

Figure 3.12: Temperature contours [K] for Configurations A - suction (top) and B - blowing (bottom) at $t = 2.5$, 5, 10 and 20 s (from left to right).

Configuration	Renewal time [s]	Peak infiltration rate [$\mathrm{m^3\,s^{-1}}$]	Peak infiltration time [s]
A - suction - no cargo	13.0	10.5	0.7
A- suction - cargo	25.5	10.7	0.6
B - blowing -no cargo	27.7	3.1	0.3
B - blowing - cargo	25.4	5.3	0.7

Table 3.6: Infiltration data for Configurations A and B with and without cargo.

The presence of the cargo results in an increase of the renewal time for Configuration A by 96.2% (Table 3.6) compared to Configuration A without cargo. However, for Configuration B, the renewal time decreases by 8.3% with an increase of 71.0% in the peak infiltration rate. As shown in Figure 3.8, the time evolutions of the infiltration rate and the heat load induced through the door exhibit similar profiles for Configurations A and B with cargo. Peak infiltration occurs at $t = 0.6 \sim 0.7$ s with a near constant infiltration rate from $t \sim 7.5$ s.

Due to the presence of the cargo, recirculation zones seen without the cargo in Figure 3.10b are no longer observed. As shown in Figure 3.12, During the first few seconds after the door opening, the cold high-velocity air near the doorway exits the trailer. Then the infiltration of the atmospheric air occurs along the top region of the trailer with the

Thèse accessible à l'adresse : https://theses.insa-lyon.fr/publication/2024ISAL0034/these.pdf © [J. Jeong], [2024], INSA Lyon, tous droits réservés

exfiltration of the cold air above the cargo. The area of the infiltration progressively increases before the trailer is completely filled with the atmospheric air. For Configuration A, the renewal time increases due to the infiltration of the atmospheric air being limited by the exiting cold air on top of the cargo. However, for Configuration B, the renewal time decreases as the cargo prevents the formation of the recirculation zones. From the temperature contours on Figure 3.12, the cargo limits the variation of flow structures that can form inside the trailer and therefore both configurations demonstrate similar flow pattern throughout the simulation. Due to minor temperature changes within the cargo compared to the air inside the trailer, temperature contours of the cargo are excluded from Figure 3.12.

However, there are minor differences that can be observed between Configurations A and B with cargo. At $t = 2.5$ s, the exiting cold high-velocity air causes stronger mixing to occur for Configuration A. This mixing limits the infiltration of pure atmospheric air into the trailer until $t \sim 10$ s. This is due to the velocity of the pre-existing flow being higher than that of Configuration B as discussed in Section 3.3.2 (Table 3.5).

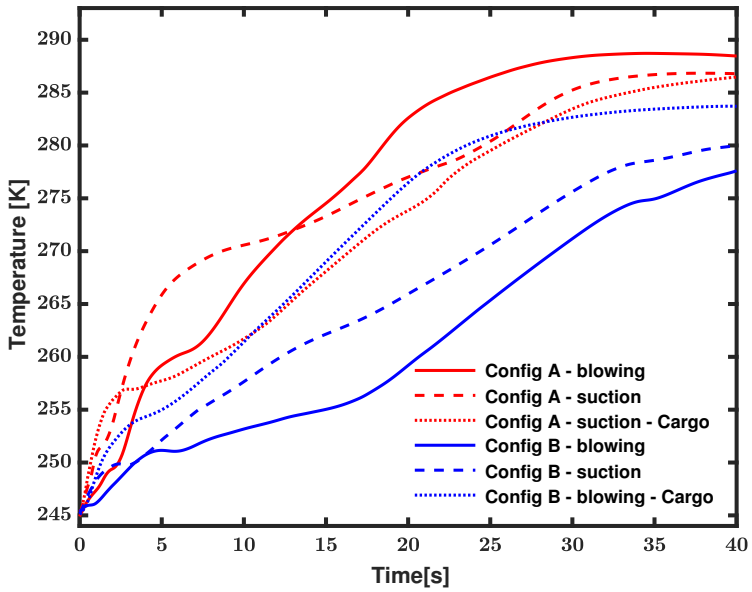

Figure 3.13: Time evolution of the area averaged temperature inside the trailer.

From Figure 3.13, the temperature inside the trailer for Configuration B with cargo is higher than Configuration A with cargo for the time interval $t \sim 15$ s to $t \sim 25$ s. As the exiting cold high-velocity air mixing with the atmospheric air limits the infiltration of pure atmospheric air for Configuration A. Regardless, the temperature change of the air inside the trailer for all configurations and operating modes exhibits similar profile to the temperature change observed by Rai et *al.* [65].

Configuration	Cargo 1	Cargo 2	Cargo 3	Cargo 4	Cargo 5
A - suction	246.7	247.3	247.4	247.6	247.9
B - blowing	247.5	249.1	249.9	249.8	249.8

Table 3.7: Maximum temperature [K] of the cargo at $t = 40$ s.

Thèse accessible à l'adresse : https://theses.insa-lyon.fr/publication/2024ISAL0034/these.pdf © [J. Jeong], [2024], INSA Lyon, tous droits réservés

As the temperature change is higher for Configuration B after the cold high-velocity air exits the trailer, from Table 3.7, the maximum temperature observed at each cargo box after 40 seconds is significantly higher for Configuration B (locations of each cargo box described in Section 3.3.2). The temperature difference is greater than the initial maximum temperature difference of 0.3 K (Table 3.5). A maximum temperature difference of 2.5 K for Cargo 3 and a minimum temperature difference of 0.8 K is observed for the inner-most cargo (Cargo 1) between Configurations A and B, respectively. For Configuration B, the highest cargo temperature is observed on Cargo 3 as the exiting cold air on top of the cargo and the recirculation zones at the back of the trailer mixing with the infiltrated atmospheric air limits other cargo boxes from making contact with the hot air. For Configuration A, the highest cargo temperature is observed at the outer-most cargo (Cargo 5), as the exiting cold air mixed with the atmospheric air makes the earliest contact and increases its temperature. The maximum cargo temperatures observed are still below the regulated temperature for quick (deep) frozen foodstuffs at 255.15 K [2].

3.4 Conclusion

To analyze the feasibility of the eutectic system, a numerical model has been developed by employing the $k-\omega$ SST turbulence model to predict the thermoaeraulic behavior of the air during the infiltration period for a refrigerated truck trailer equipped with eutectic plates. The numerical model has been validated against the published experimental results of Lafaye de Micheaux et *al.* [60]. During the validation, it was identified that while the 3D approach showed a better agreement with the experimental data, it does not bring a significant improvement over the results obtained with the 2D models. Therefore, 2D model with the heat conduction across the container walls was chosen for modelling the refrigerated truck trailer with the eutectic plates.

With the numerical model, two different configurations were tested with the eutectic plates placed in parallel at the back of the trailer (Configuration A) and in series located along the roof of the trailer (Configuration B). Without the presence of the cargo, Configuration B took 91.0 % and 88.5 % longer to reach the renewal time compared to Configuration A with the blowing and suction modes respectively. For both fan operating modes, Configuration B exhibits an air curtain behavior and significantly limits the infiltration of the hot atmospheric air. For both configurations, recirculation zones created by the pre-existing flows within the truck trailer also limits the infiltration rate and its advancement. However, when the cargo is introduced, recirculation zones are no longer observed and both configurations demonstrate similar flow patterns throughout the simulation with similar renewal times. During the simulation, maximum cargo temperatures observed for either configurations are still below the regulated temperature for quick (deep) frozen food stuff at 255.15 K [2]. Therefore, infiltration analysis validates the viability of the eutectic system for the transport of frozen foodstuff. However, as the eutectic plates were modelled as constant temperature plates without the phase change of the eutectic mixture and the formation of the frost on top of the plates, further analysis with the incorporation of the aforementioned phenomena is required.

Thèse accessible à l'adresse : https://theses.insa-lyon.fr/publication/2024ISAL0034/these.pdf © [J. Jeong], [2024], INSA Lyon, tous droits réservés

Thèse accessible à l'adresse : https://theses.insa-lyon.fr/publication/2024ISAL0034/these.pdf © [J. Jeong], [2024], INSA Lyon, tous droits réservés

Chapter 4

Frost Model

For the transport of the frozen foodstuff, temperature is regulated to be below 255.15 K for the duration of the transport [2]. To ensure the regulatory requirements are satisfied, cold plates with the constant temperature of 244 K was employed for the infiltration model in Chapter 3. Given the duration of the door opening period of less than two minutes with the initial cold plate temperature of 244 K, desublimation process was assumed to be the sole phase change phenomena occurring on top of the plate. Therefore, a numerical model capable of accurately predicting the development of frost on top of a cold plate was developed. This chapter presents the obtained results presented during the 7^{th} *IIR International Conference on Sustainability and the Cold Chain* held in United Kingdom.

4.1 Geometrical modeling

In the following section, the geometrical configuration is first described in detail. The numerical methodology (algorithms, numerical schemes) as well as the numerical parameters, including the mesh grid, the boundary conditions and the time step are then presented.

Figure 4.1 depicts the domain of the numerical simulation with the boundary conditions developed for the frost formation on a cold flat plate. Since the validation was performed against a number of published experimental results, readers are referred to the published dimensions of each experimental setup. For each validation case, an adiabatic wall of length L_1 is added to the leading edge of the cold aluminum plate for the flow to better resolve before interacting with the plate. For the validation against the results of Nascimento et *al*. [75], a cold plate is also located on the top surface of the channel at the same horizontal location as the bottom plate. Symmetry condition is imposed on the top surface of the channel for the validation cases against the experimental results of Cheng and Wu [76], Hermes et *al*. [77], and Wang et *al*. [78]. Heights of the experimental setup for these authors are significantly greater than the frost thickness, ranging from 150 mm to 300 mm. Therefore, to reduce the computational cost, appropriate height with symmetry condition is adopted for the simulation. Frost simulated at the opposite side of the symmetry condition is not of importance, symmetry is solely utilized to simulate the accurate air flow far away from the frost layer. As a matter of a fact, a channel with 50 mm in height with symmetric boundary condition applied on the top surface was tested and showed negligible difference to the results obtained from the complete 150 mm height channel.

Thèse accessible à l'adresse : https://theses.insa-lyon.fr/publication/2024ISAL0034/these.pdf © [J. Jeong], [2024], INSA Lyon, tous droits réservés

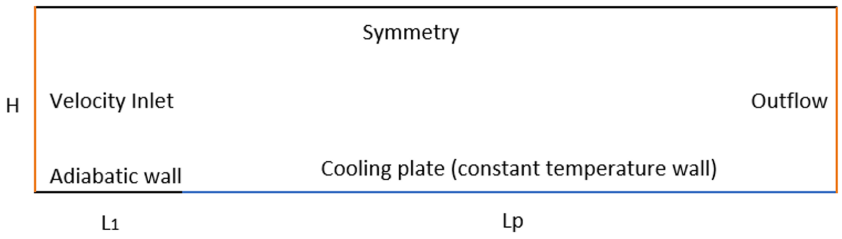

Figure 4.1: Numerical domain for the frost formation on a cold plate.

4.2 Numerical modeling

For the validation of the frost model, the air channel is initially assumed to be full of humid air at rest with the inlet temperature and water vapour mass fraction, as shown in Equations 4.1 and 4.2.

$$u_{a_0} = 0,\ v_{a_0} = 0,\ T_{a_0} = 0,\ w_{va} = w_{in} \tag{4.1}$$

$$u_{c_0} = 0,\ v_{c_0} = 0,\ T_{c_0} = 0,\ w_{c_0} = 0 \tag{4.2}$$

where u, v are the horizontal and vertical velocitiy components of the humid air, T is the temperature, w is the mass fraction, α the volume fraction, va the water vapour, a the humid air, c the ice, and subscript 0 refers to the initial condition.

For the boundary conditions, all walls of the air channels are modelled as adiabatic walls. Velocity inlet is applied to the inlet of the channel. Outflow condition is applied at the outlet of the channel as shown in Equation 4.3 and Equation 4.4. Pressure outlet boundary condition provided similar results as the outflow condition in terms of obtained frost thickness and density. However, outflow boundary condition provided better numerical stability of the solver.

$$\frac{\partial u_a}{\partial x} = 0,\ \frac{\partial v_a}{\partial x} = 0,\ \frac{\partial T_a}{\partial x} = 0,\ \frac{\partial w_{va}}{\partial x} = 0 \tag{4.3}$$

$$\frac{\partial u_a}{\partial x} = 0,\ \frac{\partial v_a}{\partial x} = 0,\ \frac{\partial T_a}{\partial x} = 0,\ \frac{\partial \alpha_c}{\partial x} = 0 \tag{4.4}$$

4.2.1 Numerical method

The Eulerian-Eulerian granular multiphase model in ANSYS FLUENT 2020R2 is adopted. The ice is formed directly from the water vapour desublimation and all other phase change processes such as condensation are neglected. The primary phase is set to be the humid air, aluminum and the secondary phase is set to be the ice droplets with the diameter of 10^{-5}m.

All the physical properties of the humid air are taken as the weighted averages of the dry air and water vapour properties, except for the thermal conductivity. As the concentration of the water vapour is relatively low, the thermal conductivity of the humid air is assumed to be the value of the dry air. For the ice and the aluminium, the physical properties within the FLUENT database is employed.

The conservation equations for mass, momentum and energy are solved using the finite-volume method. A second-order Backward-Euler scheme with implicit time-stepping is used for the temporal discretization. The pressure-velocity coupling is overcome using SIMPLE phase-coupled scheme. PRESTO! scheme was used for the pressure while

Thèse accessible à l'adresse : https://theses.insa-lyon.fr/publication/2024ISAL0034/these.pdf © [J. Jeong], [2024], INSA Lyon, tous droits réservés

QUICK scheme was used for the momentum, volume fraction, energy and species conservation. All the under-relaxation factors were set to be 0.2.

Depending on the Reynolds number, the $k-\omega$ Shear Stress Transport (SST) model is adopted with second-order upwind discretization schemes for the turbulence kinetic energy and specific dissipation rate. Otherwise, the flow is considered to be laminar. The convergence criteria for all variables were chosen to be a relative error of 10^{-5} Simulations are performed using the HPC facilities of Compute Canada or Calcul Québec's networks using 4 CPU nodes with 32 *2 × Intel E5-2683 v4 Broadwell @ 2.1GHz* cores per node.

Due to the nature of the Eulerian-Eulerian multiphase model, it is difficult to define the boundary of the frost by an arbitrary limit of the ice volume fraction for each cell. Therefore, thenumerical values of the frost thickness are determined by the MATLAB Image Processing Tool. The Sobel gradient operator function ('Imgradient') is applied to the normalized greyscale image ('rgb2gray') of the frost to define the outline of the frost layer. The frost thickness is calculated as an average over the plate length. For the validation against the results of Cheng and Wu [76], the frost thickness is measured 30 mm from the leading edge of the plate, as specified.

4.2.2 Governing equations

The governing equations include the mass, momentum, and energy conservation equations with the species conservation equation for the water vapour. As only the water vapour desublimation is being simulated, the mass transfer from the humid air to the ice governs the frosting process. Based on the mass transfer, the momentum and energy transfers from the water vapour to ice can occur and are reflected as the momentum and energy sources of the governing equation. To account for the water diffusion driven by the concentration gradient from the humid air to the frost layer, a source term is included in the species conservation equation. Interested readers are referred to the works of Wu et *al.* [5; 46] for the detailed description of the frost model.

Source terms

The source terms in the governing equations correspond to the mass transfer rate from the humid air to the ice, $\dot{m}_{ac}$, As only the desublimation is taken into consideration, the mass transfer rate from the ice to the humid air, $\dot{m}_{ca}$, is assumed to be zero. Therefore, the source terms in the mass, momentum, energy and species conservation governing equations are shown in Equations 4.5 to 4.8, respectively.

$$S_{mc} = \dot{m}_{ac},\ S_{ma} = -\dot{m}_{ac} \tag{4.5}$$

$$S_{uc} = \dot{m}_{ac}u_c,\ S_{ua} = -\dot{m}_{ac}u_a \tag{4.6}$$

$$S_{hc} = \dot{m}_{ac}(h_{va} + h_{l,va}),\ S_{ha} = -\dot{m}_{ac}h_{va} \tag{4.7}$$

$$S_{va} = -\dot{m}_{ac} \tag{4.8}$$

where h is enthalpy, h_l the released latent heat per unit mass of water vapour during the desublimation process. Subscripts m, u and h refers to mass, u to momentum, and h to energy, respectively.

Thèse accessible à l'adresse : https://theses.insa-lyon.fr/publication/2024ISAL0034/these.pdf © [J. Jeong], [2024], INSA Lyon, tous droits réservés

Interphase Transfer

For the interphase momentum exchange, Wen-Yu's model for the fluid-solid momentum exchange coefficient is adopted [79; 46]. The momentum exchange coefficient K between two phases K is defined as:

$$K = \frac{18\rho_a\alpha_a v_a\alpha_c f}{d_c^2} \tag{4.9}$$

where f is the drag function from the Wen-Yu's experimental correlation:

$$f = (1 + 0.15Re_c^{0.687})\alpha_a^{-2.65} \tag{4.10}$$

For the interphase heat exchange, the Ranz-Marshall correlation is preferred to identify the Nusselt number Nu_{ca} [80; 46]. The intensity of heat exchange is defined by the temperature difference between the two phases:

$$\vec{q}_{ca} = -\vec{q}_{ac} = E_{ca}(T_c - T_a) \tag{4.11}$$

where F_{ca} is the heat transfer coefficients between the two phases defined as:

$$E_{ca} = \frac{6\lambda_a\alpha_a\alpha_c Nu_{ca}}{d_c^2} \tag{4.12}$$

where λ_a is the thermal conductivity of the humdid air and the Nusselt number Nu_{ca} is defined by the Ranz-Marshall correlation as:

$$Nu_{ca} = 2.0 + 0.6Re_c^{1/2}Pr_a^{1/3} \tag{4.13}$$

Mass transfer rate

The mass transfer rate from the humid air to the ice $\dot{m}_{ac}$, governs the frosting process as the governing equations and the source terms are defined by it. Wu et *al.* [5; 46] defined the mass transfer rate by a non-dimensional phase change driving force based on Gibbs free energy as shown in Equation 2.23. Then Afrasiabian et *al.* [47] separated the frosting condition in Equation 2.23 by two independent physical parameters as shown in Equation 2.24. As the authors noted the modification of the frosting condition leading to the results being less sensitive to the non-dimensional coefficient B, Equation 2.24 with the modified frosting condition is employed.

While the numerical results obtained by Wu et *al.* [46] and Afrasiabian et *al.* [47] demonstrated a good agreement with the experimental data, their models and the definition of the non-dimensional coefficients were limited to the inlet air velocities between 0.31 and $0.92\,\mathrm{m\,s^{-1}}$, inlet air temperatures between -5 and $22\,^{\circ}\mathrm{C}$, relative humidities between 38 and 85 % and cooling surface temperatures between -20 and $-4\,^{\circ}\mathrm{C}$. Therefore, while adopting the mass transfer rate defined by Afrasiabian et *al.* [47] with the separated frosting condition for the velocity and the water vapour concentration, equation for the non-dimensional coefficient B was identified to minimize the difference between the numerical results and the published experimental data [78; 77; 75; 76], as to be valid in their extended range of operating conditions.

The modified non-dimensional coefficient for the frosting condition is defined as shown in Equation 4.14.

$$\begin{aligned} B = (&0.0000005328T_w^4 - 0.0005446910T_w^3 + 0.2085719116T_w^2 - 35.4547217993T_w \\ &+2257.4626692424) \times (-0.0282087u_{in}^2 + 0.868663u_{in} + 0.4363793) \end{aligned} \tag{4.14}$$

Thèse accessible à l'adresse : https://theses.insa-lyon.fr/publication/2024ISAL0034/these.pdf © [J. Jeong], [2024], INSA Lyon, tous droits réservés

This definition of the modified non-dimensional coefficient does not apply for the validation cases against Nascimento et *al*. [75], as it involves a parallel cold plate configuration and does not follow the configuration of the other validation cases. While the validation against Nascimento et *al*. [75] demonstrates the applicability of the current model to the parallel cold plate configuration, it would require further validations against similar configurations for the adjustment of the non-dimensional coefficient B. Furthermore, definition has changed from the previous work of Jeong et *al*. [81] after larger sample size of the non-dimensional coefficient values were tested against the published results via trial-and-error.

4.3 Grid independence and time sensitivity analysis

For the air channel, rectangular meshes with a cell size of Δx =0.1 mm and Δy =0.5 mm is used for all validation cases. Wu et *al*. [46] observed grid independence with a mesh of same cell sizes with the inlet air velocities ranging from 0.31 to 0.92 $\mathrm{m\,s^{-1}}$, with a time step of Δt =1.0 s. For the extreme conditions of Cheng and Wu [76] with the air velocity of 10 $\mathrm{m\,s^{-1}}$, grid independence analysis showed that a finer mesh of $\Delta x \times \Delta y$ = 0.05 mm $\times$ 0.025 mm resulted in a negligible difference to the mesh used in the validation cases. Through the time sensitivity analysis, time-step independent results were observed for Δt = 0.05 s, 0.01 s, 0.005 s for the cases with u_{in} = 1, 5 and 10 $\mathrm{m\,s^{-1}}$, respectively.

4.4 Validation of the Frost model

The numerical model is validated for a wide range of operating conditions against the published experimental results of Lee et *al*. [38], Cheng and Wu [76], Hermes et *al*. [77], Wang et *al*. [78] and Nascimento et *al*. [75]. The operating conditions of each validation case are summarized in Table 4.1.

Figure 4.2 illustrates an example of the numerical results obtained from the frost model. Figure 4.2(a) and Figure 4.2(b) presents the obtained numerical volume fraction of ice and temperature distributions for case No.12, thick condensed layer of frost with the same temperature as the cold plate at 262.6 K has been formed near the plate with the layers of the frost on top with increasing temperature. Figure 4.2(c) shows the humid air velocity distributions at various times. As the velocity of the humid air near the frost surface was small enough at the bottom of the velocity boundary layer of the humid air flow, frosting condition of Equation 2.23 was satisfied for the mass transfer from the water vapour in the humid air to the ice. Therefore, frost thickness increased over time as the ice formed by the phase change deposited on the frost layer [46]. Also, the local increase of the air velocity caused by the deflection of the air flow due to the frost can be observed, demonstrating the capability of the current model to predict the interaction between the humid air flow field changes and the frost growth.

Figure 4.3 displays the time evolution of the frost thickness for the validation cases (as presented in Table 1) both obtained numerically and experimentally. It also presents the experimental and numerical frost densities at$t$ = 3600 s. From t = 1800 s to t = 3600 s (t = 900 s to t = 1800 s for cases No.15 and No.16), numerically obtained frost thicknesses exhibit a maximum deviation of $\pm$18.3 % against the experimental values. As the frost thickness is relatively small for lower time intervals, percentage differences are not shown.

Numerically obtained frost densities are compared against the experimental results of

Thèse accessible à l'adresse : https://theses.insa-lyon.fr/publication/2024ISAL0034/these.pdf © [J. Jeong], [2024], INSA Lyon, tous droits réservés

Authors	No.	Cooling Surface Temperature T_w (°C)	Inlet Air Temperature T_{in} (°C)	Water Content Level w $\left(\frac{\text{kg}}{\text{kg}_{\text{air}}}\right)$	Inlet Air Velocity u_{in} (m s^{-1})
Hermes	1	-4	16	0.009	0.7
et $al.$ [77]	2	-8	16	0.09	0.7
	3	-12	16	0.09	0.7
	4	-16	16	0.09	0.7
Nascimento	5	-10.3	11.8	0.006	0.9
et $al.$ [75]	6	-24.5	11.7	0.0058	1
	7	-24.8	6	0.0038	1
	8	-10.3	5.7	0.0037	1
Lee	9	-15	25	0.0157	1
et $al.$ [38]	10	-15	25	0.0098	1
Wang	11	-10.5	16.5	0.093	5
et $al.$[78]	12	-10.5	19	0.0109	5
	13	-10.5	10.5	0.0063	5
	14	-16	10.5	0.0063	5
Cheng	15	-8.2	28.6	0.0178	10
and Wu [76]	16	-8.2	28.6	0.0098	10

Table 4.1: Frosting conditions used to validate the frost model.

Hermes et $al.$ [77], Wang et $al.$ [78] and Nascimento et $al.$ [75]. Experimental densities for the other cases were not available. At $t = 3600\,\text{s}$, the model predicts the frost densities within 25.0 % of their experimental values except for case No.13 with 29.4 % difference.

A density difference of 29.4 % observed for case No.13 is suspected to be due to the low temperature difference between the plate and the air at 22 K. Conventionally, frost models are seen to have difficulty for the cases with low temperature difference between the air and the plate [78]. For such a temperature difference, condensation could affect the frosting process, which is not considered by the current model. However, such density difference between the numerical results and the experimental data is not observed for the low velocity cases with low temperature difference between the air and the plate. Due to the high velocity of the air for case 13, the effect of condensation affecting the frosting process might have been exacerbated. As the results of Wu et $al.$ [46] reported absolute deviation of 30 % and 25 % for the averaged frost thickness and the weight, maximum deviation of $\sqrt{(30\%)^2 + (25\%)^2} \approx 39\%$ is approximated for the frost density. All the obtained results fall within the deviations observed by Wu et $al.$ [46]. The current model with the modified frosting criterion coefficient provides improved results with an absolute deviation of 18.3 % and 29.4 % for the frost thickness and density, respectively.

Thèse accessible à l'adresse : https://theses.insa-lyon.fr/publication/2024ISAL0034/these.pdf © [J. Jeong], [2024], INSA Lyon, tous droits réservés

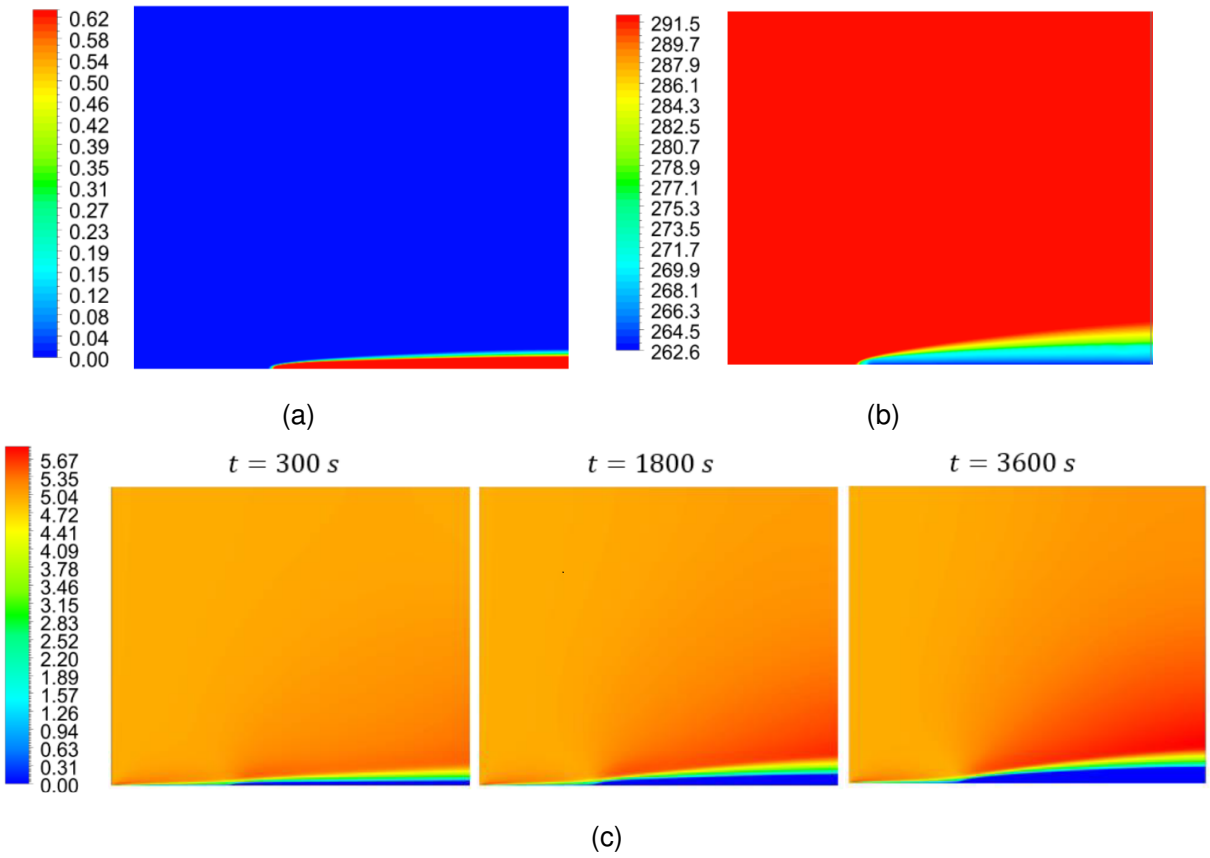

Figure 4.2: Numerical results for Case No.12: (a) Volume fraction of ice at $t = 3600\,\mathrm{s}$, (b) Temperature distribution (K) at $t = 3600\,\mathrm{s}$, and (c) Air velocity distribution(ms^{-1}).

Figure 4.4 displays the comparison between the experimental data and the numerical results for both the frost thickness and the frost density. Generally, numerically obtained results for both the frost thickness and the frost density exhibit a good agreement with the experimental data. While the numerical results for case 13 provide inadequate frost density with a 29.4 % difference compared to the experimental data, Figure 4.4 suggests that the difference is still within an acceptable range.

By extending the models of Wu et *al.* [5; 46], and Afrasiabian et *al.* [47] a new numerical frosting condition was developed for a wider range of operating conditions. The modification was performed to the non-dimensional frosting criterion coefficient, B, and $k-\omega$ SST turbulence model was applied. The present model was favorably validated in terms of frost thickness and density against the experimental results of e et *al.* [38], Cheng and Wu [76], Hermes et *al.* [77], Wang et *al.* [78] and Nascimento et *al.* [75]. However, the model showed difficulty when the temperature difference between the air and the cold plate was below 25 K for the tested operating conditions. The model can be further improved by optimizing the equation of the non-dimensional frosting criterion coefficient, B. However, significant efforts are required to repeat the simulations with varying coefficient values. It would also require many validation cases with various operating conditions and configurations to be applied as a generalized model for the frosting process. Furthermore, identifying the exact range of Reynolds number for the application of the $k-\omega$ SST turbulence model will be a difficult task.

While there are still improvements to be made to the frost model, it was deemed that the validated frost model above is applicable to be used for the combined frost and

Thèse accessible à l'adresse : https://theses.insa-lyon.fr/publication/2024ISAL0034/these.pdf © [J. Jeong], [2024], INSA Lyon, tous droits réservés

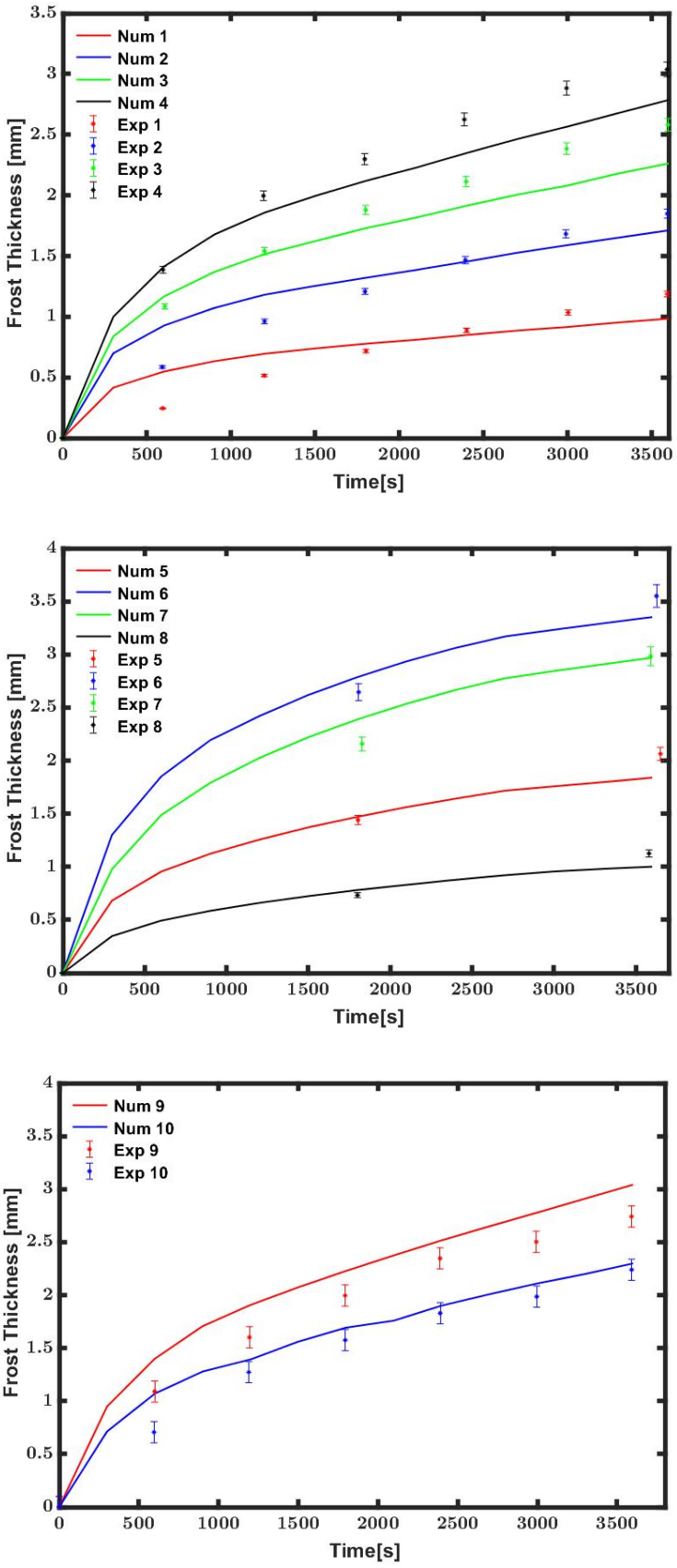

Figure 4.3: Results for the frost thickness and density at $t = 3600\,\mathrm{s}$.

Thèse accessible à l'adresse : https://theses.insa-lyon.fr/publication/2024ISAL0034/these.pdf © [J. Jeong], [2024], INSA Lyon, tous droits réservés

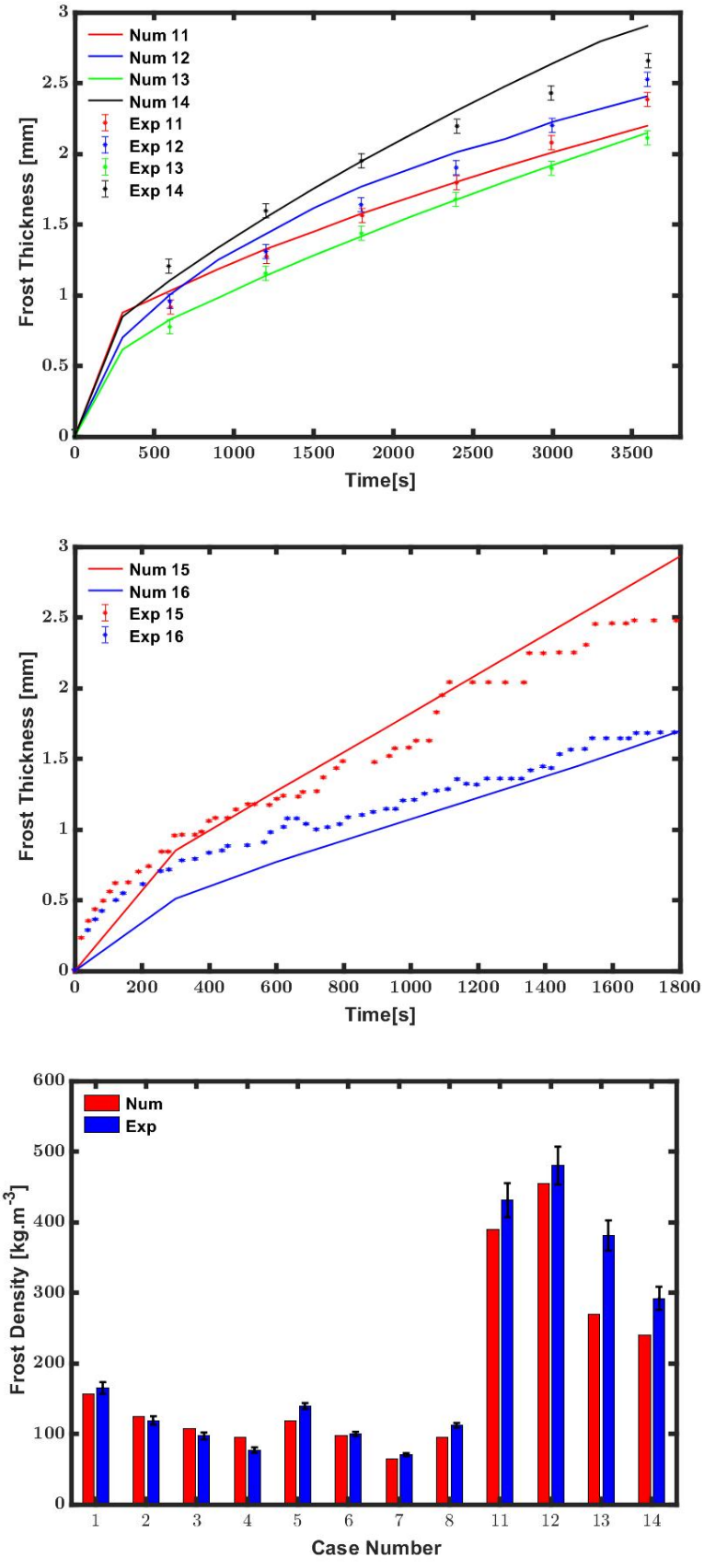

Figure 4.3: Results for the frost thickness and density at $t = 3600\,\mathrm{s}$ (cont.).

Thèse accessible à l'adresse : https://theses.insa-lyon.fr/publication/2024ISAL0034/these.pdf © [J. Jeong], [2024], INSA Lyon, tous droits réservés

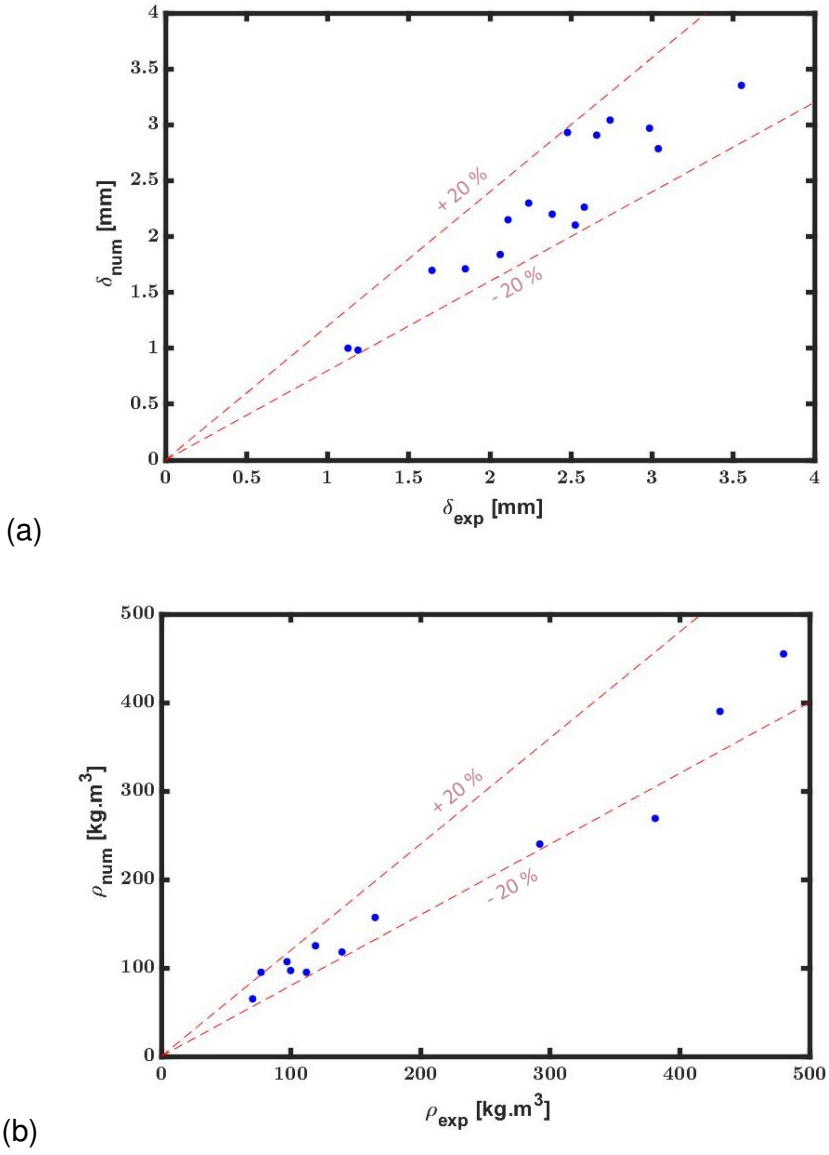

Figure 4.4: Comparison between experimental data and numerical results for the (a) Frost thickness and (b) frost density.

solidification and melting model for the system. However, it should be noted that the numerical errors from the frost model will be applied to the combined model as the frost thickness and density both contribute towards the formation of heat transferred to the surrounding air inside the air channel and to the PCM below the plate.

4.5 Conclusion

Eulerian-Eulerian granular multiphase model was developed based on the mass transfer source term from the works of Wu et *al.* [5] and Afrasiabian et *al.*[47]. The numerical model has been validated against the published numerical and experimental results. While the numerical results obtained by Wu et *al.* [5] and Afrasiabian et *al.* [47] demonstrated a good agreement with the experimental data, their models were limited to the specific

Thèse accessible à l'adresse : https://theses.insa-lyon.fr/publication/2024ISAL0034/these.pdf © [J. Jeong], [2024], INSA Lyon, tous droits réservés

ranges of initial and boundary conditions. Especially, their models were limited to the inlet air velocities below $1\,\mathrm{m\,s^{-1}}$, far below the air velocities observed around the eutectic plates from the infiltration model in Chapter 3. To extend the ranges of applicable initial and boundary conditions, $k-\omega$ SST turbulence model introduced in the infiltration model in Chapter 3 was applied along with the refinement of the non-dimensional frosting condition coefficient B via trial-and-error against the published results. The validated ranges of the operating parameters presented in this chapter are well within the close proximity to the operating conditions of the refrigerated truck trailer equipped with eutectic plates with the inlet air temperature of $21.6\,^{\circ}\mathrm{C}$, inlet air velocity of $10\,\mathrm{m\,s^{-1}}$, relative humidity of 69 %, and the initial plate temperature of $-30\,^{\circ}\mathrm{C}$.

Thèse accessible à l'adresse : https://theses.insa-lyon.fr/publication/2024ISAL0034/these.pdf © [J. Jeong], [2024], INSA Lyon, tous droits réservés

Thèse accessible à l'adresse : https://theses.insa-lyon.fr/publication/2024ISAL0034/these.pdf © [J. Jeong], [2024], INSA Lyon, tous droits réservés

Chapter 5

Consolidated Model

The main objective of this chapter is to consolidate the infiltration and frost models presented in Chapter 3 and Chapter 4, respectively, with the solidification and melting model for the eutectic mixture inside the eutectic plates. As the Eulerian-Eulerian granular frost model presented in Chapter 4 incorporates the $k-\omega$ SST turbulence model introduced in Chapter 3, it is capable of simulating the infiltration behavior of the air and the frost formation along the eutectic plates for a truck trailer equipped with eutectic plates. However, as the heat transferred to the eutectic plates from the frost formation and the infiltrating hot atmospheric air is not uniform throughout the plate, melting of the eutectic mixture is also assumed to be inhomogeneous. Therefore, solidification and melting model to predict the phase change of the eutectic mixture inside the eutectic plates must be incorporated. In this chapter, a consolidated numerical model will be presented incorporating the infiltration model presented in Chapter 3, frost model presented in Chapter 4, and the solidification and the melting model. As the solidification and melting model might behave unpredictably due to its interaction with the other numerical models, the incorporated solidification and melting model is validated against the published experimental and numerical results. Then the consolidated numerical model is applied to the experimental test-bench and validated against the obtained experimental results presented in this Chapter.

5.1 Numerical modeling

5.1.1 Geometrical modeling

The computational domain is an aluminum encasing containing the PCM with the length of 16 in.(406.4 mm)and height of 2.0625 in.(52.3875 mm) with the inner dimension of 1.5 in. by 14 in.(38.1 mm by 355.6 mm). The inner volume is located 0.1875 in.(4.7625 mm) away from the air channel with the 0.375 in.(9.525 mm) thickness at the top. The air channel is located at the bottom of the aluminum encasing containing the PCM with the length of 19.5 in.(495.3 mm) and width of 0.4 in.(10.16 mm). It should be noted that the Figure shown in Figure 5.1 is not to scale to extenuate the PCM and the encasing.

The properties of the aluminum are taken from the ANSYS FLUENT database. The properties of the PCM (Rubitherm SP-28, Rubitherm GmbH) are summarized in Table 5.1.

For validation of the consolidated model, the air channel is initially assumed to be full of humid air at rest with the inlet temperature and water vapour mass fraction, as shown

Thèse accessible à l'adresse : https://theses.insa-lyon.fr/publication/2024ISAL0034/these.pdf © [J. Jeong], [2024], INSA Lyon, tous droits réservés

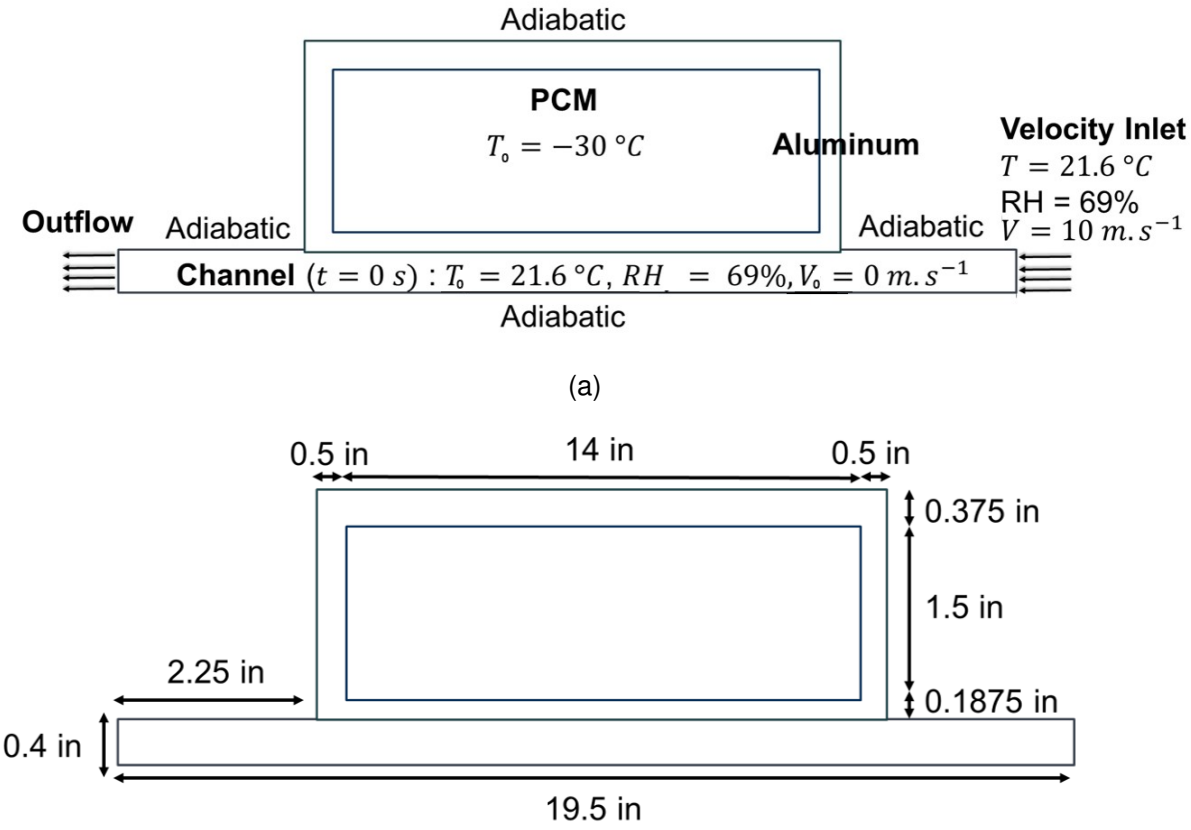

Figure 5.1: (a) Numerical/experimental schematic of the aluminum plate containing the PCM and the air channel below; (b) Dimensions of the experimental/numerical domain.

Density, ρ	$1250\,\mathrm{kg\,m^{-3}}$ (liquid/solid)
Heat capacity, C_p	$2000\,\mathrm{J\,kg^{-1}\,K^{-1}}$
Thermal expansion coefficient, CTE	$0.002\,\mathrm{K^{-1}}$
Solidus temperature, T_s	$-30\,°\mathrm{C}$
Liquidus temperature, T_l	$-28\,°\mathrm{C}$
Thermal conductivity, λ	$0.6\,\mathrm{W\,m^{-1}\,K^{-1}}$
Dynamic viscosity, μ	$0.12\,\mathrm{kg\,m^{-1}\,s^{-1}}$

Table 5.1: Properties of Rubiterm SP-28 (PCM).

in Equation 4.1 and Equation 4.2.

For the boundary conditions, all walls of the air channels are modelled as adiabatic walls. Velocity inlet is applied to the inlet of the channel. Outflow condition is applied at the outlet of the channel as shown in Equation 4.3 and Equation 4.4. Pressure outlet boundary condition provided similar results as the outflow condition in terms of obtained frost thickness and density. However, outflow boundary condition provided better numerical stability of the solver.

Thèse accessible à l'adresse : https://theses.insa-lyon.fr/publication/2024ISAL0034/these.pdf © [J. Jeong], [2024], INSA Lyon, tous droits réservés

5.1.2 Numerical method

The Eulerian-Eulerian granular multiphase model in ANSYS FLUENT 2020R2 from Chapter 4 is adopted. For the phase change of the phase change material, as the Eulerian-Eulerian multiphase model in ANSYS FLUENT 2020R2 does not allow for the existing solidification and melting model to be enabled, it was applied via User-Defined Function (UDF). The primary phase is set to be the humid air, aluminum, and the PCM and the secondary phase is set to be the ice droplets with the diameter of 10^{-5}m. The solidification and melting UDF solely functions within the primary phase of the model between the solidus and liquidus temperatures of the PCM. It should be noted that this was only possible due to the significant temperature difference between the humid air and the ice compared to the liquidus and solidus temperature of the PCM.

5.1.3 Governing equations

The governing equations are identical to the frost model described in Section 4.2.2, the source terms are listed in Equation 4.5, Equation 4.6, Equation 4.7, and Equation 4.8. An additional source term is applied in the momentum equation to describe the flow of the PCM due to the solidification and melting process as shown in Equation 5.1.

$$S_{sm} = -A(\phi)v \tag{5.1}$$

where $A(\phi)$ is the porosity function [12]. The source term S_{sm} is used to describe the flow of the PCM in the porous medium in the momentum equation. It is zero in the liquid phase to allow for the free motion while it is arbitrarily large value in the solid phase to force the velocity values to be approximately zero. To achieve this requirement, Carman-Kozeny equation derived from the Darcy law for fluid flow in porous media in a modified form is used as shown in Equation 5.2 [11; 12].

$$A(\phi) = \frac{A_{mush}(1-\phi)^2}{\phi^3 + \chi} \tag{5.2}$$

$$\phi = \begin{cases} 0, & \text{if } T < T_s \\ \frac{T-T_s}{T_l-T_s}, & \text{if } T_s < T < T_l \\ 1, & \text{if } T > T_l \end{cases} \tag{5.3}$$

where T_s and T_l are solidus and liquidus temperatures, χ is a small computational constant to prevent division by zero ($\chi = 0.001$ for this study), A_{mush} is the mushy zone constant to measure how fast the fluid velocity approaches zero as it solidifies ($A_{mush} = 10^6$ for this study [11]), and ϕ is the liquid fraction as shown in Equation 5.3.

5.1.4 Solidification and melting

For the primary phase of the numerical model, solidification and melting of the PCM is applied via a UDF. A source term, S_{sm}, is introduced in the momentum equation as shown in Equation 5.1, and the energy equation is defined as shown in Equation 5.4. The specific enthalpy (H) is the sum of the sensible enthalpy (h) and the latent heat (ΔH).

$$H = h + \Delta h = (h_{ref} + \int_{T_{ref}}^{T} C_p dT) + (\phi L) \tag{5.4}$$

Thèse accessible à l'adresse : https://theses.insa-lyon.fr/publication/2024ISAL0034/these.pdf © [J. Jeong], [2024], INSA Lyon, tous droits réservés

where h_{ref} is the reference enthalpy at the reference temperature T_{ref}, C_p is the specific heat, and L the latent heat.

5.2 Grid independence and time sensitivity analysis

For the aluminium encasing and the PCM, rectangular meshes with a cell size of $\Delta x = 1\,\text{mm}$ and $\Delta y = 1.5\,\text{mm}$ is used for all validation cases [11]. Higher mesh density resulted in a negligible difference in the melt front location and the average melt fraction. For the time step, while the time independent results were obtained for $\Delta t = 0.1\,\text{s}$, time steps for the air channel was applied as the overall system requires the smaller of the time steps to observe time-step independent results.

5.3 Validation of the UDF solidification and melting model

Since ANSYS FLUENT v2020 R2 is incapable of applying the existing solidification and melting model with the Eulerian-Eulerian multiphase model used for the frost model, the solidification and melting model is applied via a UDF as described in Section 5.1.4.

For the validation of the UDF solidification and melting model, the obtained numerical results are compared against the experimental and numerical results of Fadl and Eames [11] and Kamkari and Shokouhmand [82]. For the details regarding the experimental setup, readers are referred to the works of Fadl and Eames [11]. Conventionally within the solidification and melting model present in the ANSYS FLUENT v2020 R2, the thermophysical properties are based on the Boussinesq model for the natural convection modeling with mean property values between liquidus and solidus temperature applied. While the application of the mean property values is reasonable, it completely neglects the possible unique profiles of the thermophysical properties between the liquidus and solidus temperature of a given fluid and could lead to the significant differences between the numerical and experimental results.

Figure 5.2 displays the predicted melt front locations for the ANSYS FLUENT version of the solidification and melting model denoted as Model 1 in the legend of this figure with the thermophysical properties based on the Boussinesq model for the natural convection modeling. For the varying values of A_{mush} ranging from 10^6 to 10^7, the number of peaks and troughs of the melt front varies. Locations of the peaks and troughs are inaccurately predicted both from the ANSYS FLUENT model applied and the simulated results of Fadl and Eams [11]. However, the value of $A_{mush} = 10^6$ presents the most accurately melt front location and hence the most accurate melt fraction of the PCM.

For the UDF version of the solidification and melting model, the Boussinesq model for the natural convection modeling previous applied to the ANSYS FLUENT version of the solidification and melting model cannot be applied as the ANSYS FLUENT does not allow for the existing solidification and melting model to be enabled with the Eulerian-Eulerian multiphase model. Therefore, a more simple approach is applied where the density is linearly interpolated between the liquidus and solidus temperature and the viscosity is assumed to be constant except a significantly large number when the PCM is solid. Furthermore the specific enthalpy of the PCM varies according to section 5.1.4 to incorporate the solidification and melting of the PCM as a UDF by varying specific heat of the PCM.

Thèse accessible à l'adresse : https://theses.insa-lyon.fr/publication/2024ISAL0034/these.pdf © [J. Jeong], [2024], INSA Lyon, tous droits réservés

Figure 5.3 compares the melt front locations between the UDF and the ANSYS FLUENT versions of the solidification and melting model. The UDF version of the solidification and melting model is denoted as Model 2. For t = 600 s to t = 2400 s, negligible difference is observed between the ANSYS FLUENT model and the UDF solidification and melting model. While the locations of the peaks and troughs of the melt front are different, average y location of the melt front and the number of peaks and troughs of the melt front are nearly identical. At t = 3600 s, the accuracy of the UDF model slightly decreases as it predicts the average y location of the melt front 13.1 % and 7.6 % higher than that of the experimental value and the Boussinesq model, respectively. However, the average y location of the melt front and the melt fraction is still within the acceptable range with 4.2 % to 13.1 % difference compared to the experimental results, respectively.

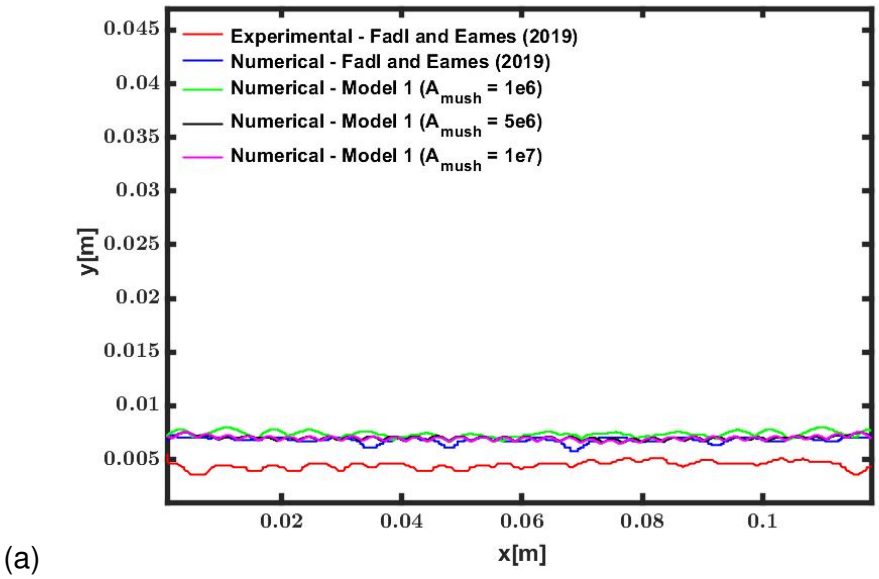

(a)

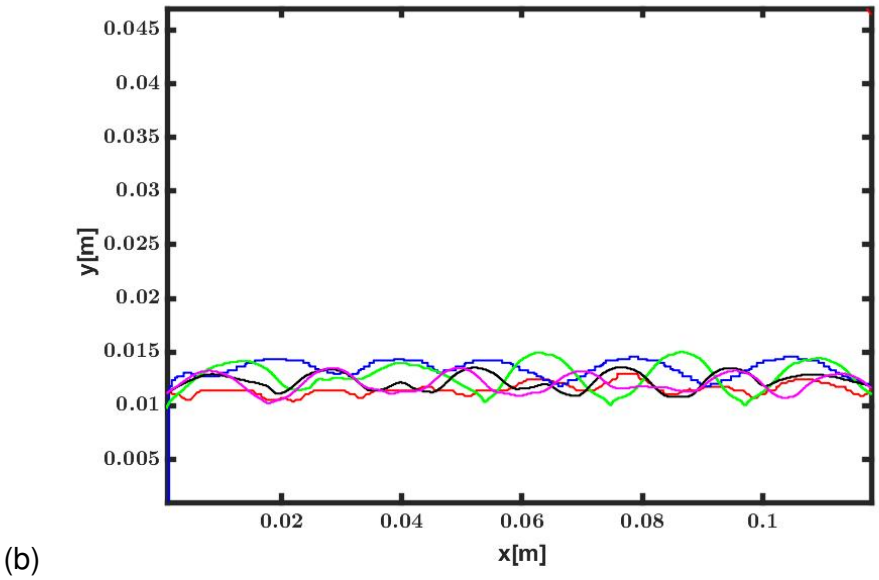

(b)

Figure 5.2: Melt front of the Solidification and Melting model for A_{mush} = 10^6, 5×10^6 and 10^7 at (a) t = 600 s, (b) t = 1200 s, (c) t = 2400 s, (d) t = 3600 s.

Thèse accessible à l'adresse : https://theses.insa-lyon.fr/publication/2024ISAL0034/these.pdf © [J. Jeong], [2024], INSA Lyon, tous droits réservés

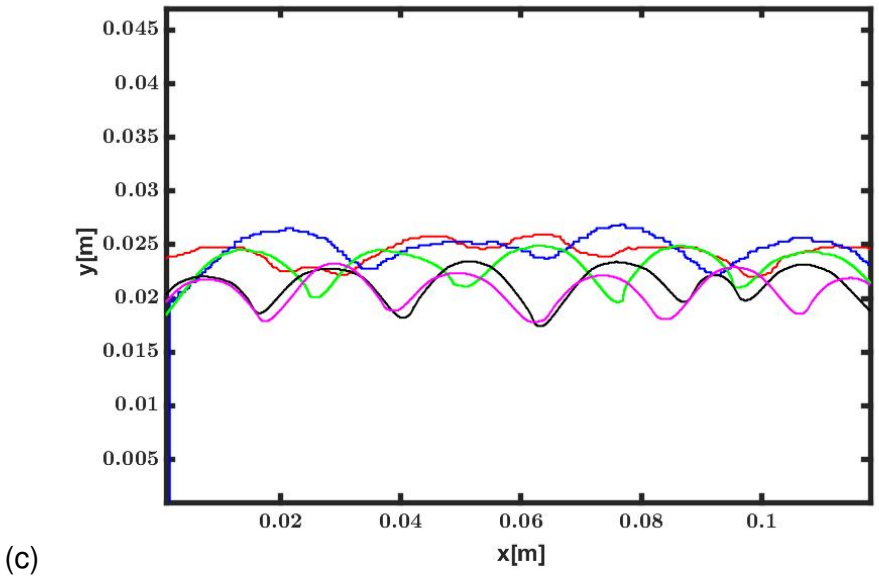

(c)

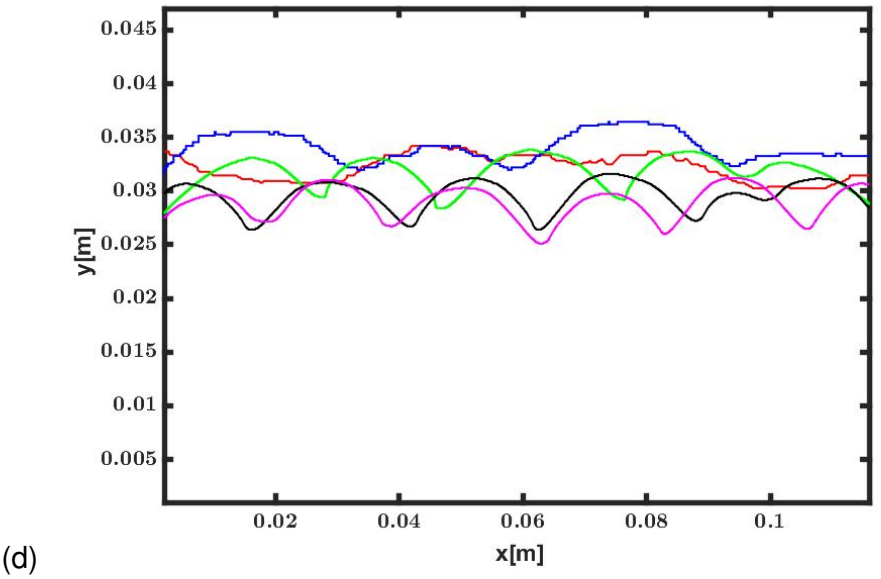

(d)

Figure 5.2: Melt front of the Solidification and Melting model for A_{mush} = 10^6, 5×10^6 and 10^7 at (a) t = 600 s, (b) t = 1200 s, (c) t = 2400 s, (d) t = 3600 s (cont.).

It should be noted that greater differences arises for the average melt front y location at t = 600 s for all simulated results compared to the experimental result.

The peaks and troughs of the melt front are formed due to the formation of the Rayleigh-Bénard convection cells as shown in Figure 5.5. As the bottom of the experimental setup is exposed to the high temperature while the rest of the sides are adiabatic (covered via plexiglass and insulators), Rayleigh-Bénard convection cells are created. From both the Boussinesq model and the UDF model, accurate prediction of the locations of the peaks and troughs of the melt front could not be obtained. This indicates that for an accurate prediction of the locations of the peaks and troughs of the melt front, more accurate approach in modelling the thermophysical properties and evaluation of the appropriate A_{mush} value is required. However, as shown in Figure 5.4, the average y location of the melt front and the melt fraction values are within the satisfactory range, the UDF

Thèse accessible à l'adresse : https://theses.insa-lyon.fr/publication/2024ISAL0034/these.pdf © [J. Jeong], [2024], INSA Lyon, tous droits réservés

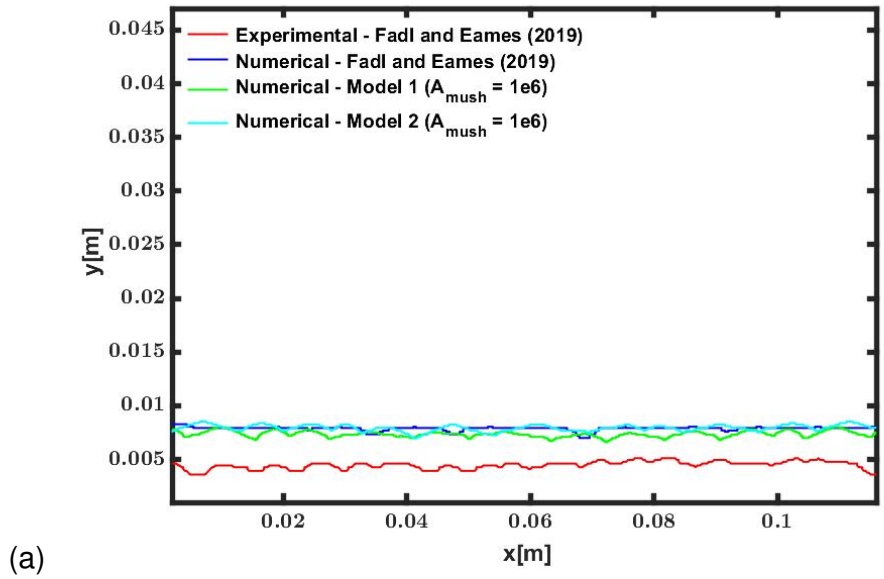

(a)

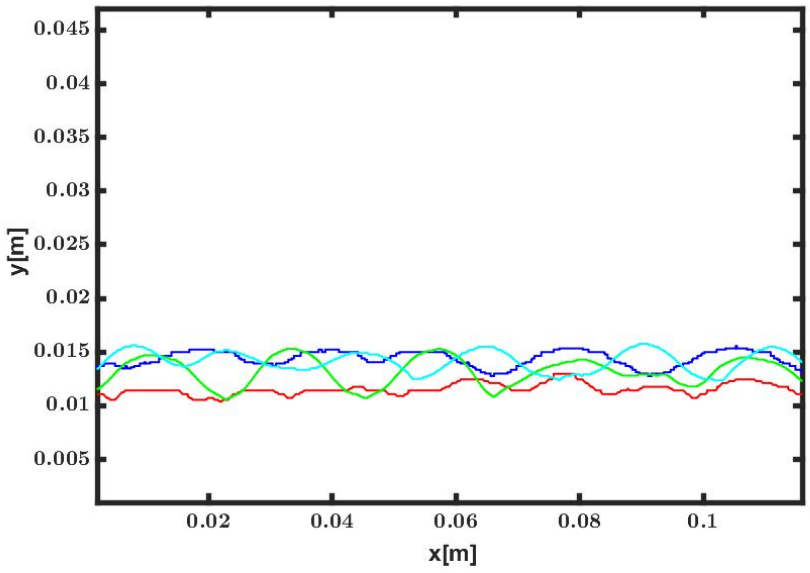

(b)

Figure 5.3: Melt front of the UDF Solidification and Melting model for $A_{mush} = 10^6$ at (a) t = 600 s, (b) t = 1200 s, (c) t = 2400 s, (d) t = 3600 s.

solidification and melting model is applied for the complete model.

5.4 Consolidated Model Validation

5.4.1 Experimental setup

For the experimental validation of the consolidated numerical model, the experimental setup of Rahal [83] was used. The 2D schematic of the experimental setup can bee seen in Figure 5.1. For more detailed information regarding the experimental setup, readers are referred to the works of Rahal [83].

The experimental investigation has been performed by a set up primarily composed

Thèse accessible à l'adresse : https://theses.insa-lyon.fr/publication/2024ISAL0034/these.pdf © [J. Jeong], [2024], INSA Lyon, tous droits réservés

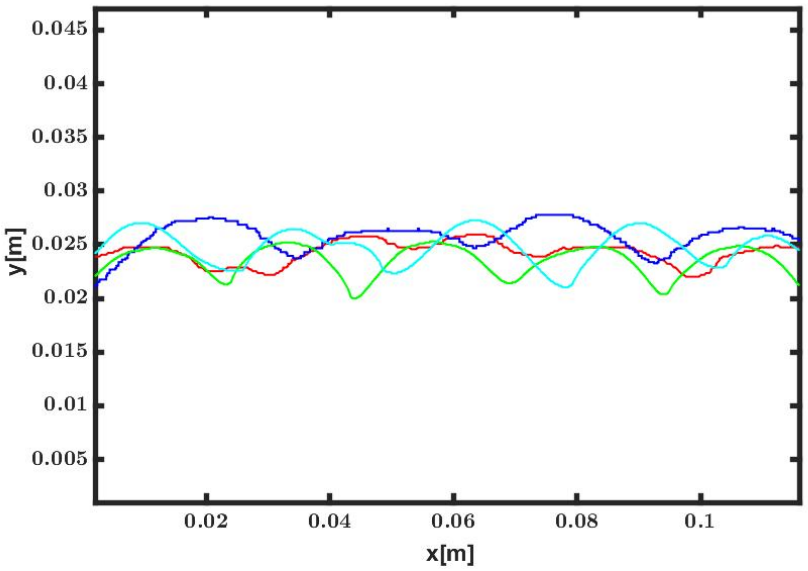

(c)

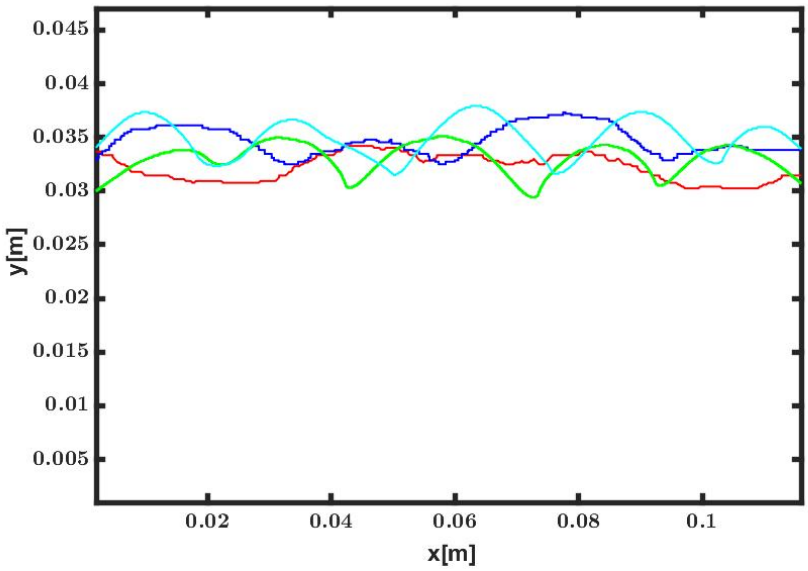

(d))

Figure 5.3: Melt front of the UDF Solidification and Melting model for $A_{mush} = 10^6$ at (a) t = 600 s, (b) t = 1200 s, (c) t = 2400 s, (d) t = 3600 s. (cont.)

of two components:

1. An air channel with the converging air inlet and diverging outlet made out of plastic resin by additive manufacturing.

2. A container for the PCM made out of aluminum that is connected to the test section of the air channel. Aluminum panels of varying sizes covers the upper portion of the PCM container as shown in Figure 5.6(d).

The aluminum encasing containing the PCM is connected to the air channel test section, where the upper portion of the aluminum encasing acts as the floor of the test section of the air channel. Then a plexiglass cover acts as the upper and the side walls of the test section as show in Figure 5.6 for the observation and measurement of the frost.

Thèse accessible à l'adresse : https://theses.insa-lyon.fr/publication/2024ISAL0034/these.pdf © [J. Jeong], [2024], INSA Lyon, tous droits réservés

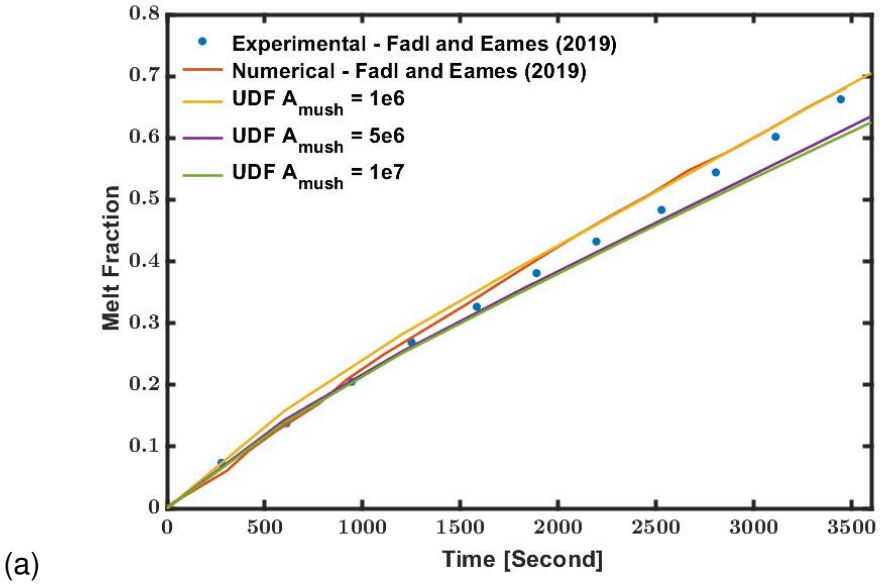

(a)

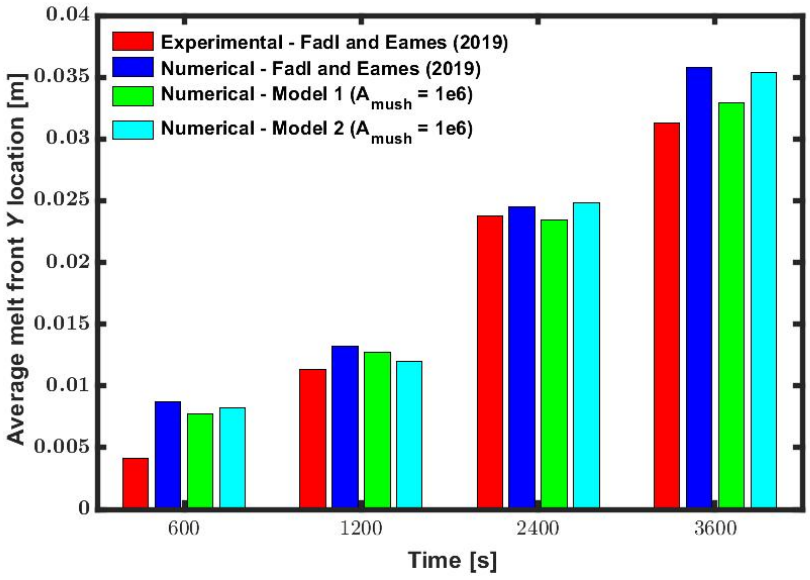

(b)

Figure 5.4: (a) Melt fraction for different values of A_{mush} using the UDF model; (b)Average melt front y location for two applied solidification and melting schemes and $A_{mush} = 10^6$.

The aluminum PCM encasing is 355 mmin length, 304 mm in width and 34 mm in depth. It is divided into four identical compartments as shown in Figure 5.6(b). As displayed in Figure 5.6(c) for one of the divided compartments, total of 16 type T thermocouples (Omega Engineering TT-T-36-25) separated into four groups of four thermocouples placed equidistant to each other are placed within the compartment to measure the temperature of the PCM. The coil pipe system within the encasing is connected to the Thermo Bath (Thermo Haake ARCTIC AC200 A40 Immersion Bath) with 900 W cooling capacity at 20 °C. For the thermofluid, silicone oil SIL180 with the thermal conductivity of $0.12\,\mathrm{W\,m^{-1}K^{-1}}$ and dynamic viscosity of $0.041\,\mathrm{kg\,m^{-1}\,s^{-1}}$ from Thermofischer is used to transfer the heat away from the PCM during the solidification phase. Two surface thermocouples (SA 1XL-T-SRTC, Omega Engineering) are also attached to the inlet and outlet

Thèse accessible à l'adresse : https://theses.insa-lyon.fr/publication/2024ISAL0034/these.pdf © [J. Jeong], [2024], INSA Lyon, tous droits réservés

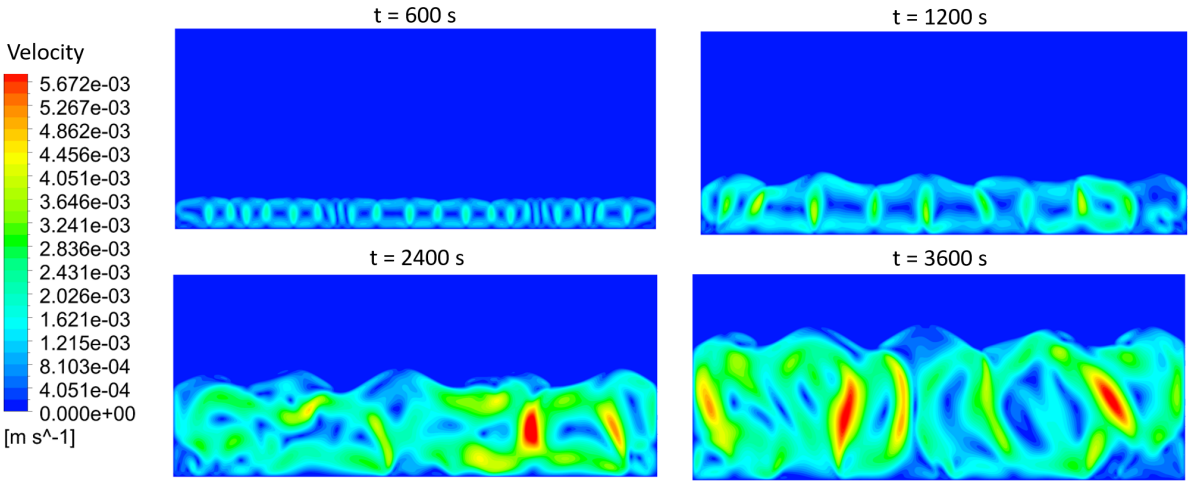

Figure 5.5: Velocity magnitude of the melted PCM for $A_{mush} = 10^6$ at four different times.

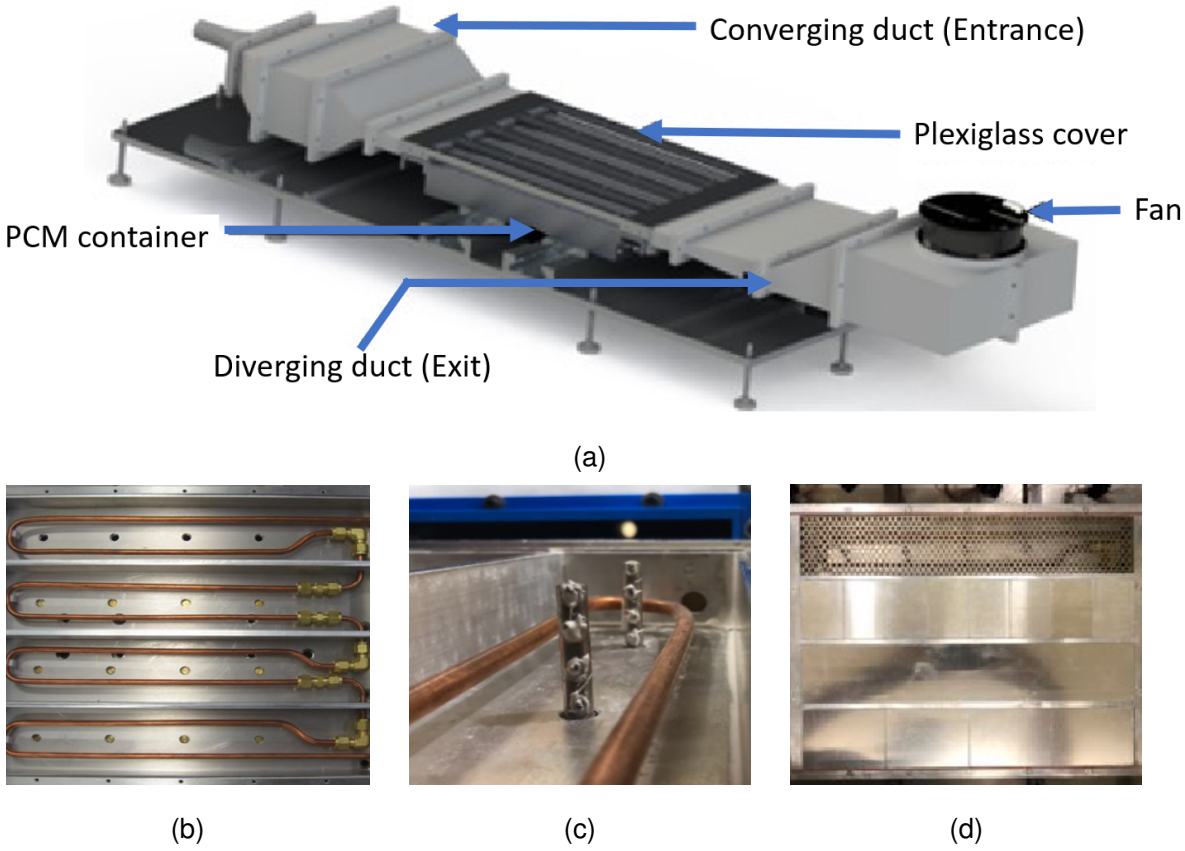

Figure 5.6: (a) CAD view of the experimental setup, and zooms on the (b) aluminum encasing, (c) thermocouples locations inside the aluminium encasing, (d) aluminum panels of varying sizes for measuring the frost weight.

of the coil pipes. The walls of the aluminium encasing are covered with the polyurethane foam (McMaster-Carr, ref. 9385K21) with the thermal conductivity of $0.022\,\mathrm{W\,m^{-1}\,K^{-1}}$ for insulation.

The inlet of the experimental setup is connected to the climatic chamber HSH27C at the PIMUS laboratory of Université de Sherbrooke to control the relative humidity and

Thèse accessible à l'adresse : https://theses.insa-lyon.fr/publication/2024ISAL0034/these.pdf © [J. Jeong], [2024], INSA Lyon, tous droits réservés

Measurement	Provider	Model Number	Range	Uncertainty
Frost thickness	HSI		1280×1080 pixels	$0.1mm$
PCM Temperature	Omega	TT-T-36-25	$-40\,°C$ to $30\,°C$	$\pm 0.2\,°C$
Surface Temperature	Omega	SA 1XL-T-SRTC	$-29\,°C$ to $260\,°C$	$\pm 0.05\,°C$

Table 5.2: Uncertainty of the equipment.

the temperature of the air. For the velocity of the air, Vortex Powerfan S-1000 with the duct diameter of 10 in. is used to control the velocity from $0.1\,\mathrm{m\,s^{-1}}$ to $0.5\,\mathrm{m\,s^{-1}}$. A RDT camera from HSI with the resolution of 1280×1080 pixels are used to measure the thickness of the frost. The acquisition of the photos are carried out with MIDAS image processing software. The uncertainties of the equipment used in the experiment are listed in Table 5.2.

For the validation of the numerical model, eutectic mixture of potassium bicarbonate solution with the phase change temperature of $-5.4\,°C$ and the latent heat of fusion of $268.54\,\mathrm{kJ\,kg^{-1}}$ was used [84]. Due to the limitation of the experimental setup, PCM with the lower phase change temperature could not be explored.

5.4.2 Experimental setup adjustment

As the air channel is located on the upper portion of the PCM container for the experimental setup of Rahal [83], it resulted in no observable amount of frost formed during the experiment. Results of the numerical simulation of the experimental setup with the initial condition of Figure 5.1 (a) are shown in Figure 5.7 and Figure 5.8. From the melt fraction of the PCM shown in Figure 5.7, melting of the PCM is shown to be focused primarily in the upper portion of the PCM. As the high temperature air flow is above the plate, heat is primarily transferred from the air through the plate to the upper portion of the PCM. Therefore, highly localized melting of the PCM in the upper region of the PCM can be observed. From t =600 s to t =1800 s, melting of the sides of the PCM can also be observed due to the heat transferred through the aluminum encasing, but it is difficult to conclude that the PCM is being fully utilized as the heat transfer is primarily via conduction alone within the PCM.

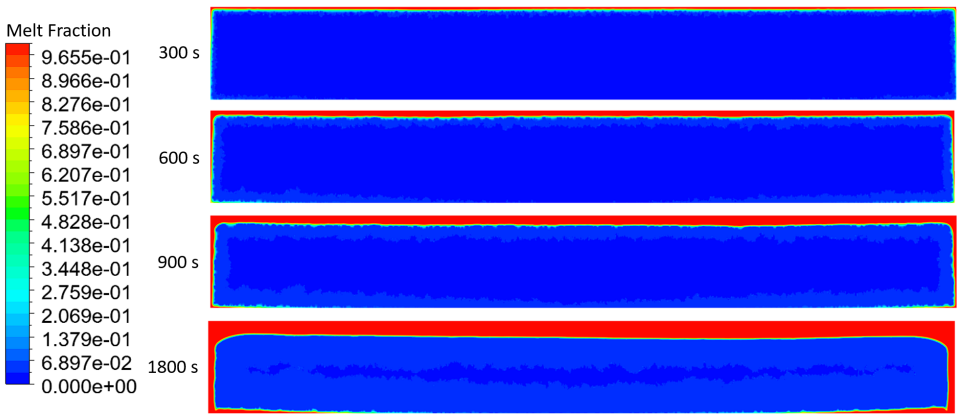

Figure 5.7: 2D contours of the PCM melt fraction at four different times.

Thèse accessible à l'adresse : https://theses.insa-lyon.fr/publication/2024ISAL0034/these.pdf © [J. Jeong], [2024], INSA Lyon, tous droits réservés

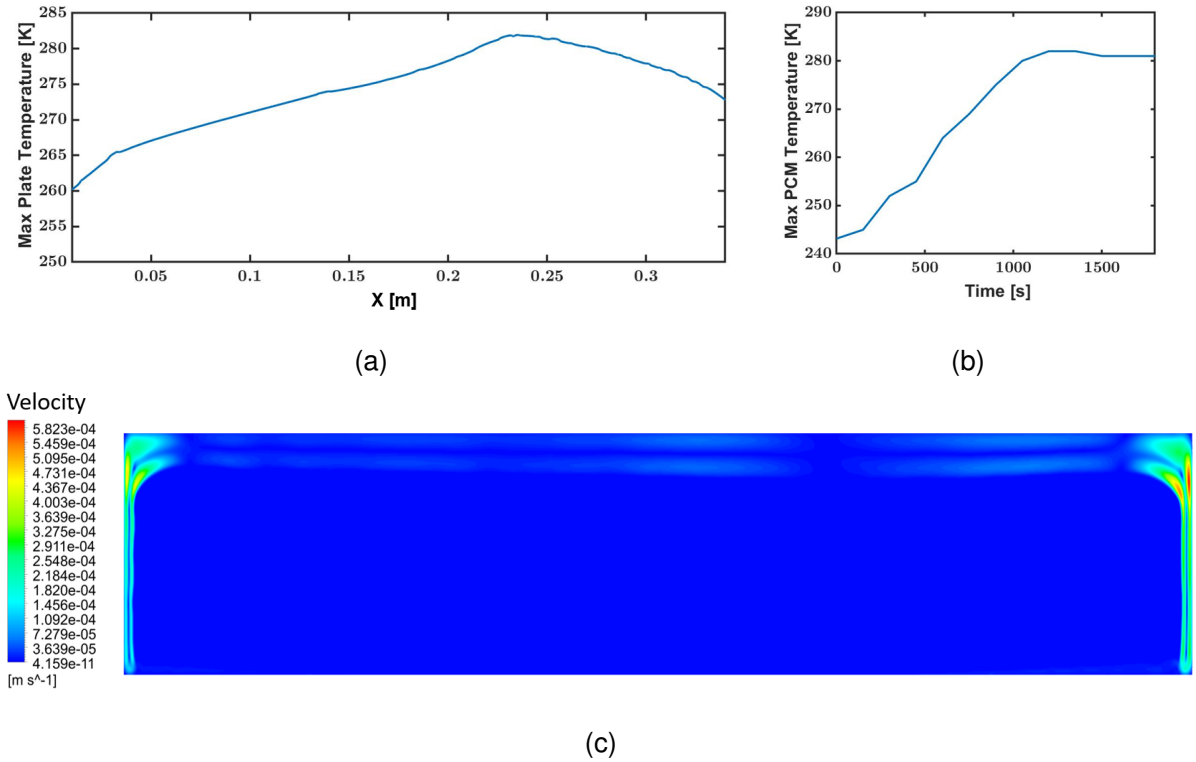

Figure 5.8: Numerical results for the (a) maximum plate temperature at $t = 1800\,\mathrm{s}$, (b) maximum PCM temperature over time and (c) velocity magnitude contours of the PCM at $t = 1800\,\mathrm{s}$.

Furthermore, maximum plate temperature at t =1800 s shown in Figure 5.8 (a) indicate a temperature difference of the plate being up to 22 K. This indicates the existence of highly localized high temperature region within the plate (at $x \approx 0.23\,\mathrm{m}$) caused by the localized melting of the PCM. From Figure 5.8(b), after $t = 800\,\mathrm{s}$, maximum PCM temperature of over 273.15 K is observed, effectively nullifying the conditions for the frost to be formed on top of the plate. Additionally, velocity contour of the PCM at $t = 1800\,\mathrm{s}$ shown in Figure 5.8(c) demonstrate no movement of the melted PCM in the upper region of the PCM, concluding that the heat transfer is primarily via conduction with the current setup. There is slight buoyancy driven movement of the melted PCM on the sides caused by the temperature-driven density difference. However, it is localized to the sides of the PCM and does not influence the upper portion of the melted PCM, where the majority of the heat transfer from the air to the PCM occurs.

From the experiment, it was also observed that as the PCM melts, there is a loss of contact between the PCM and the aluminum plate on top of the PCM due to the volumetric change. With the highly localized melting of the PCM in the upper region of the PCM, contact between the PCM and the plate is immediately lost, effectively limiting the influence of the PCM. Therefore, the experimental setup of Rahal [83] was flipped. The aluminum plates of varying sizes originally covering the PCM was replaced with a single aluminium panel with the same thickness. For the new experimental setup, the air channel is located at the bottom of the PCM container. Due to the nature of the setup, mass of the frost cannot be measured as it was originally planned with the aluminum plates of varying sizes of Rahal [83]. Therefore the validation will primarily focus on the thickness of the frost and the temperature of the PCM.

Thèse accessible à l'adresse : https://theses.insa-lyon.fr/publication/2024ISAL0034/these.pdf © [J. Jeong], [2024], INSA Lyon, tous droits réservés

5.5 Experimental results

The initial temperature of the PCM containment system was set to be at $T = -7\,^{\circ}\mathrm{C}$ to ensure the complete solidification of the eutectic solution of potassium bicarbonate PCM for the experiment. Then two different inlet conditions were tested with temperatures at $T_{inlet} = 5\,^{\circ}\mathrm{C}$ and $0\,^{\circ}\mathrm{C}$, where the relative humidity and velocity of the inlet was fixed to be 70 % and $0.1\,\mathrm{m\,s^{-1}}$, respectively. Due to the adjusted experimental setup with the air channel located below the eutectic plate, only temperature of the PCM and the frost thickness were validated.

Table 5.3 and Table 5.4 displays the comparison between the numerical and experimental results for the frost thickness and PCM temperature, respectively. Obtained experimental frost thicknesses for both inlet temperatures of $T = 5\,^{\circ}\mathrm{C}$ and $0\,^{\circ}\mathrm{C}$ agrees with the numerical results accounting for the uncertainty of the camera being 0.1 mm. However, as the maximum frost thickness obtained during the experiment is 0.15 mm with 0.1 mm uncertainty, it is difficult to conclude on the accuracy of the experimental results and its comparison against the numerical results.

	$T_{in} = 5\,^{\circ}\mathrm{C}$		$T_{in} = 0\,^{\circ}\mathrm{C}$	
Time	Experimental	Numerical	Experimental	Numerical
[min]	[mm]	[mm]	[mm]	[mm]
0	0	0	0	0
5	0	0	0.08	0
10	0.06	0.04	0.08	0.07
15	0.06	0.07	0.13	0.09
20	0.15	0.08	0.13	0.09
25	0.12	0.09	0.14	0.09
30	0.12	0.09	0.13	0.09

Table 5.3: Experimental and numerical frost thickness for $T_{in} = 5\,^{\circ}\mathrm{C}$ and $T_{in} = 0\,^{\circ}\mathrm{C}$.

	$T_{in} = 5\,^{\circ}\mathrm{C}$		$T_{in} = 0\,^{\circ}\mathrm{C}$	
Time	Experimental	Numerical	Experimental	Numerical
[min]	[°C]	[°C	[°C]	[°C]
0	-7.3	-7.3	-7.3	-7.3
15	-6.0	-6.8	-6.1	-7.0
30	-5.8	-6.9	-5.9	-6.9
45	-5.4	-6.9	-5.2	-6.9
60	-5.3	-6.8	-5.2	-6.9

Table 5.4: Experimental and numerical PCM temperature from the thermocouple placed closest to the plate inside the PCM for $T_{in} = 5\,^{\circ}\mathrm{C}$ and $T_{in} = 0\,^{\circ}\mathrm{C}$.

Thèse accessible à l'adresse : https://theses.insa-lyon.fr/publication/2024ISAL0034/these.pdf © [J. Jeong], [2024], INSA Lyon, tous droits réservés

For the PCM temperature, temperature difference of up to 1.7 K is observed at t =3600 s with the uncertainty of the thermocouples for the PCM temperature being 0.2 K. The temperature difference is assumed to be attributed by the condensation and melting of the frost observed during the experimentation. As the numerical model was designed for a significantly lower initial PCM temperature of $-30\,^{\circ}$C, it accounted solely for the desublimation as the phase change phenomena within the air channel. Condensation is an exothermic process while melting of the frost is an endothermic process. Therefore, higher experimental PCM temperature indicates that heat was released from the air channel into the PCM, attributing condensation as the main cause for the temperature difference between the experimental and numerical results. This also indicate that melting of the frost observed during the experiment is most likely to be condensation and seeping of the water vapours into the frost layers than the melting of the frost itself.

5.6 Results and discussion

As the continuation of the works of Jeong et *al.* [85] with the numerical simulation of the thermoaeraulic behaviour of the air during the opening of the door of a refrigerated truck trailer equipped with cold plates, frost formation on top of the eutectic plates and the solidification and melting of the eutectic plates with the same initial PCM temperature of $-30\,^{\circ}$C has been simulated. The inlet conditions and the dimensions of the numerical domain are displayed in Figure 5.1. Additionally, inlet temperature of $T_{inlet} = 26.6\,^{\circ}$C with identical relative humidity and velocity was simulated to compare the results. For both cases, air channel is located to be below the PCM to promote the formation of the Rayleigh-Bénard convection cells during the melting of the PCM, as observed from the experiment in Section 5.4.

Figure 5.9(a) displays the average frost thickness of the numerical simulations. For the inlet temperature of $T_{inlet} = 21.6\,^{\circ}$C, sharp increase of the frost thickness between $t = 0$ s to 60 s can be observed. Then the frost thickness steadily increases until $t = 240$ s and demonstrate minimal increase afterwards. In contrast for the inlet temperature of $T_{inlet} = 26.6\,^{\circ}$C, rather a gradual increase in the frost thickness is observed until $t = 180$ s. Then a sharp increase in the frost thickness between $t = 180$ s to 240 s is observed with a linear profile increase afterwards. Until $t = 480$ s, frost thickness for the inlet temperature of $T_{inlet} = 26.6\,^{\circ}$C is lower than that of $T_{inlet} = 21.6\,^{\circ}$C. From Figure 4.3, same behavior was observed between case 11 and case 12. While case 12 had 2.5 K higher inlet temperature, until $t = 600$ s, numerically it showed lower frost thickness than that of case 11. This behavior might be due to the higher initial temperature of the humid air increasing the amount of time and energy it requires to cool the air to reach the supersaturated state for the frost to form, as the relative humidity is the same. While this difference is minimal, as the air velocity is high at $u_{in} = 10\,\mathrm{m\,s^{-1}}$, the influence might be exaggerated, especially during the early period of the frost formation. Additionally, as displayed in Figure 5.9(b), the frost thickness increase rate between the two cases demonstrate similar profiles.

Due to the nature of the setup, melting of the PCM is focused on the lower region of the PCM containment as shown in Figure 5.10. At $t = 540$ s, formation of the Rayleigh-Bénard convection cells in the melted region of the PCM is clearly depicted. Furthermore, sides of the PCM has been melted by the heat conducted through the surrounding aluminum encasing. The rightmost side of the PCM has higher region of melted PCM than the leftmost side as the airflow is from the right to the left. Figure 5.9(c) displays the linear relationship between the melt fraction and time for both cases.

Thèse accessible à l'adresse : https://theses.insa-lyon.fr/publication/2024ISAL0034/these.pdf © [J. Jeong], [2024], INSA Lyon, tous droits réservés

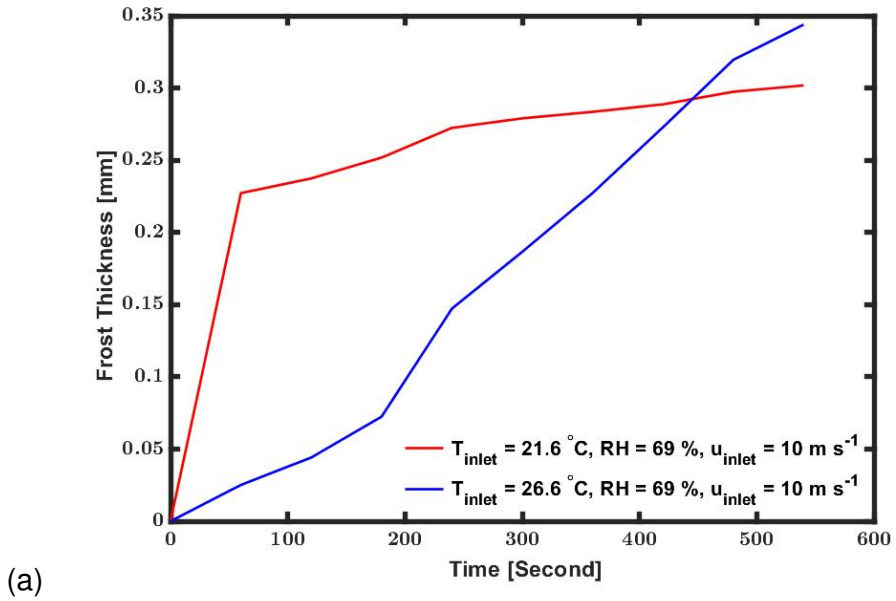

(a)

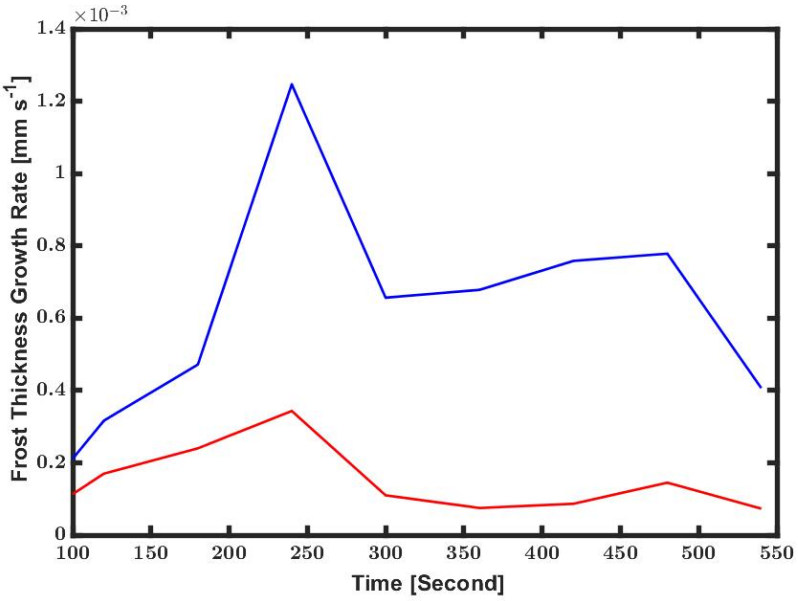

(b)

Figure 5.9: Numerical results for the (a) frost thickness, (b) rate of increase in frost thickness, (c) PCM temperature, (d) melt fraction, and (e) outlet temperature.

For T_{inlet} = 21.6 °C, it exhibited overall higher melt fraction and maximum PCM temperature observed. For a typical door opening time of 900 s [65; 86], 16.34% of the PCM would have melted from the linear approximation of the numerical results. Even for delivery cycles with short door openings of between t =120 s to 180 s, 2.3 % to 3.4 % of the PCM melt can be observed. From the maximum PCM temperature shown in Figure 5.9(d), maximum PCM temperature of T =−17.99 °C at t =180 s is observed. As the maximum regulated temperature for quick deep frozen foodstuff is also at T =−18 °C, ineffectiveness of certain regions of the PCM to meet the regulated temperature requirements due to the inhomogeneous melting of the PCM can be expected even for a short door opening period [2].

Thèse accessible à l'adresse : https://theses.insa-lyon.fr/publication/2024ISAL0034/these.pdf © [J. Jeong], [2024], INSA Lyon, tous droits réservés

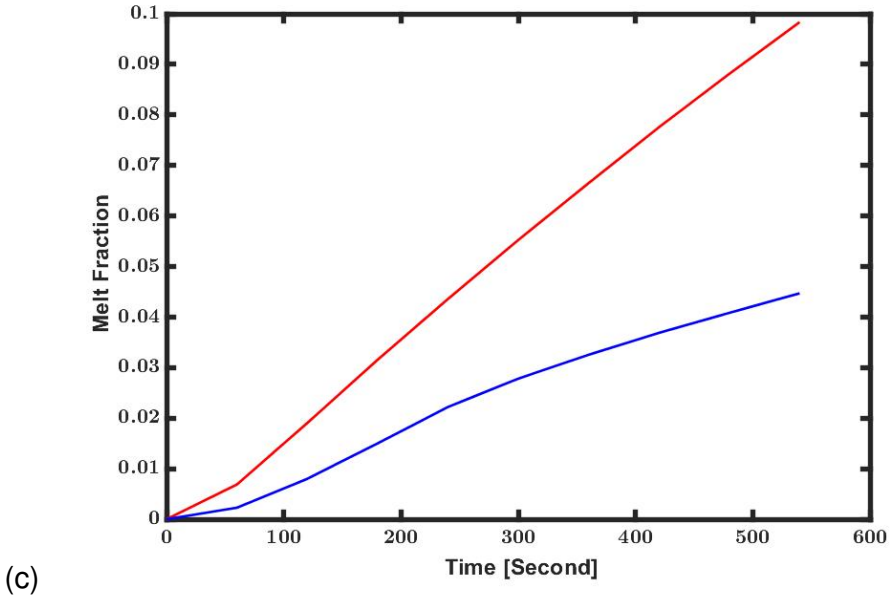

(c)

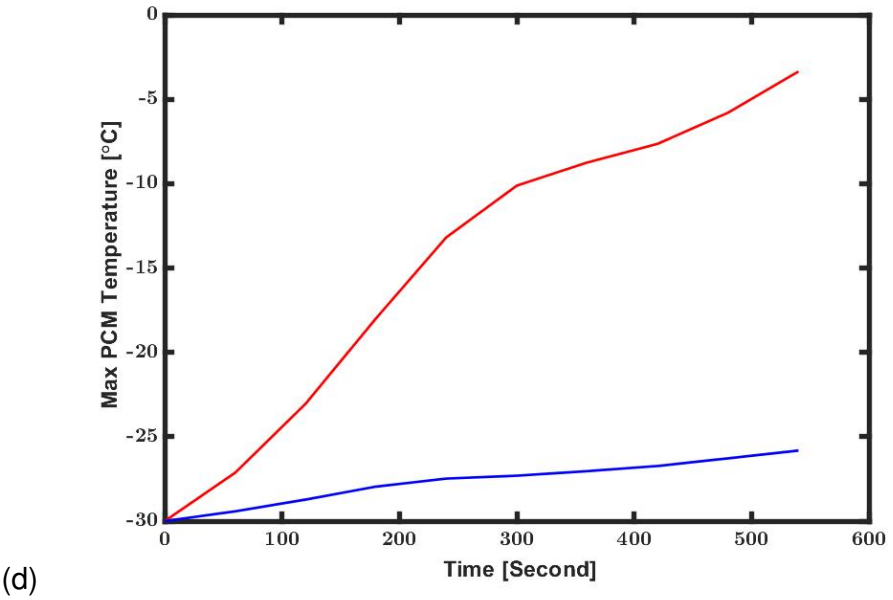

(d)

Figure 5.9: Numerical results for the (a) frost thickness, (b) rate of increase in frost thickness, (c) PCM temperature, (d) melt fraction, and (e) outlet temperature (cont.).

For $T_{inlet} = 26.6\,°C$, lower melt fraction and maximum PCM temperature were observed. At $t = 540\,s$, only approximately 4 % of the PCM melted. Also from $t = 0\,s$ to $540\,s$, mere $3\,K$ increase in the maximum PCM temperature was observed. Figure 5.9(e) displays the outlet temperature for $T_{inlet} = 26.6\,°C$ being lower than that of $T_{inlet} = 21.6\,°C$ after $t = 120\,s$. Additionally, at $t = 540\,s$, density of the frost was measured to be $574.53\,kg\,m^{-3}$ and $324.33\,kg\,m^{-3}$ for the cases with inlet temperature of $T_{inlet} = 21.6\,°C$ and $T_{inlet} = 26.6\,°C$, respectively. Therefore from the average frost thickness, $T_{inlet} = 26.6\,°C$ reported lower frost mass of $0.04\,kg$ than for $T_{inlet} = 21.6\,°C$ with $0.06\,kg$ at $t = 540\,s$ for unit meter of width. This demonstrate that for $T_{inlet} = 21.6\,°C$, majority of the PCM melt was due to the frost formation, observed by higher frost

Thèse accessible à l'adresse : https://theses.insa-lyon.fr/publication/2024ISAL0034/these.pdf © [J. Jeong], [2024], INSA Lyon, tous droits réservés

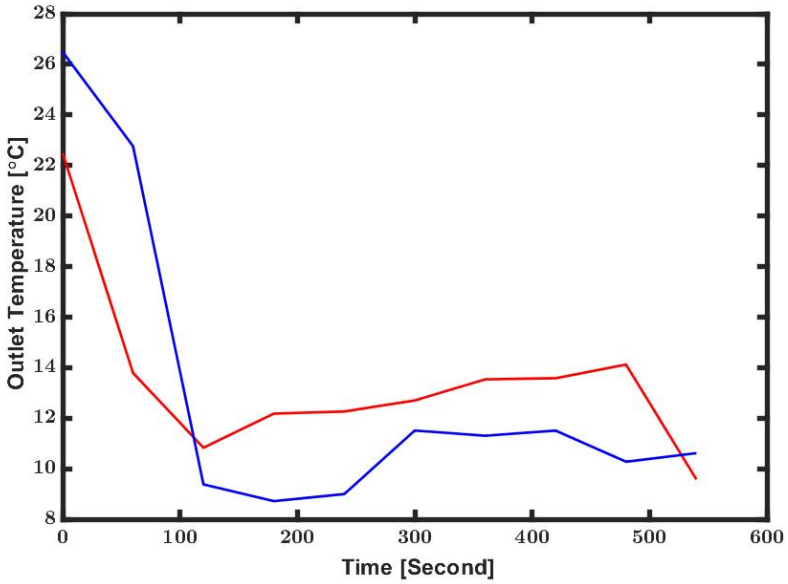

(e)

Figure 5.9: Numerical results for the (a) frost thickness, (b) rate of increase in frost thickness, (c) PCM temperature, (d) melt fraction, and (e) outlet temperature (cont.).

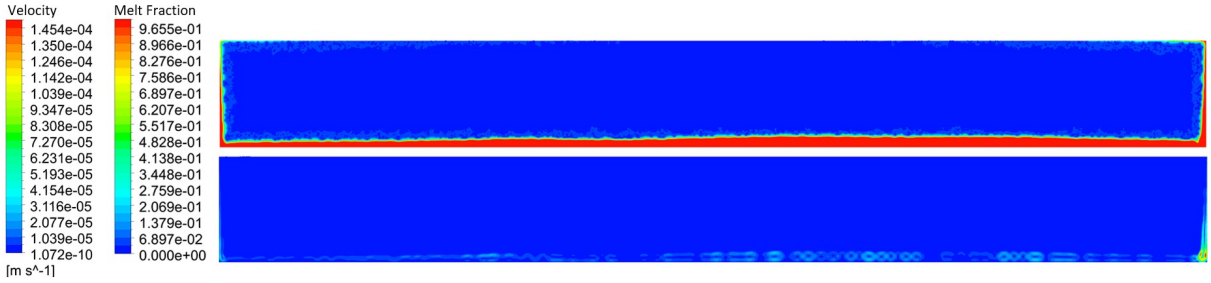

Figure 5.10: 2D contours of the melt fraction (top), and velocity magnitude (bot) at $t = 540\,\mathrm{s}$.

mass, higher outlet temperature and maximum PCM temperature. In contrast, for $T_{inlet} = 26.6\,^{\circ}\mathrm{C}$ as the frost formed on top of the PCM is lower until $t = 480\,\mathrm{s}$, most of the PCM melt was due to the cooling of the air. As the outlet temperature for $T_{inlet} = 26.6\,^{\circ}\mathrm{C}$ is lower than for $T_{inlet} = 21.6\,^{\circ}\mathrm{C}$ with $5\,\mathrm{K}$ higher inlet temperature and significantly less PCM melt, the adverse outcome of the frost formation is exemplified.

5.7 Conclusion

In this chapter, the infiltration model and the frost model presented in Chapter 3 and Chapter 4 were consolidated with the solidification and melting model applied as a UDF. As the existing solidification and melting model within ANSYS FLUENT could not be enabled with the Eulerian-Eulerian multiphase model used for the frost model, the solidification and melting model was applied via a UDF. Since the UDF version of the solidification and melting model incorporated with the infiltration and the frost models might behave inaccurately, it has been favorably validated against the published experimental and numerical results in terms of melt front location and melt fraction.

Additionally, experiment performed at the Université de Sherbrooke was presented

Thèse accessible à l'adresse : https://theses.insa-lyon.fr/publication/2024ISAL0034/these.pdf © [J. Jeong], [2024], INSA Lyon, tous droits réservés

in this chapter. The experimental setup of Rahal [83] was adopted. However, with the given initial and boundary conditions of the experimental setup, frost formation could not be observed neither experimentally nor numerically. As the air channel is located on the upper portion of the PCM container, it was numerically concluded that it results in a highly localized high temperature region near the upper region of the PCM. Furthermore, there is little to no heat diffusion that occurs via convection apart from the minor convection that occurs along the side walls of the PCM due to the temperature-driven density difference caused by the heat transferred by the aluminum encasing. Experimentally, a loss of contact between the PCM and the plate was observed, as the upper region of the PCM melts and lead to the volumetric change associated with the phase change of the PCM. Therefore, the experimental setup of Rahal [83] was adjusted so that the air channel is located at the bottom of the PCM container. The obtained experimental frost thickness was in agreement with the numerical results. However, as the maximum frost thickness obtained during the experiment is 0.15 mm with 0.1 mm uncertainty, it is difficult to conclude on the accuracy of the experimental results and its validation against the numerical results. For the PCM temperature, experimental results showed maximum temperature difference of up to 1.7 K after 3600 s. This temperature difference is assumed to be attributed by the condensation observed during the experimentation. Numerically, as the given initial temperature of the given eutectic system is $-29\,^{\circ}\mathrm{C}$ with the time of the exposure to the infiltrating hot atmospheric typically being less than $t = 120\,\mathrm{s}$, condensation was neglected. Due to the limitation of the experimental setup, initial temperature of the experimental setup could only be lowered to $t = -10\,^{\circ}\mathrm{C}$ and resulted in the occurrence of condensation.

Finally, the consolidated numerical model was applied to the typical initial and boundary conditions experienced by a refrigerated truck trailer during humid summer. Two different inlet temperature were simulated with $T_{inlet} = 26.6\,^{\circ}\mathrm{C}$ and $T_{inlet} = 21.6\,^{\circ}\mathrm{C}$ with identical inlet relative humidity and velocity (69 % and $10\,\mathrm{m\,s^{-1}}$, respectively). The results showed that until $t = 480\,\mathrm{s}$, frost thickness observed on top of the eutectic system for $T_{inlet} = 26.6\,^{\circ}\mathrm{C}$ being lower than that of $T_{inlet} = 21.6\,^{\circ}\mathrm{C}$. This is assumed to be due to the higher inlet temperature requiring longer time and higher energy to reach the supersaturated state, exaggerated by the high inlet velocity during the early period of the frost formation. Due to the lower amount of frost formed on top of the plate, $T_{inlet} = 26.6\,^{\circ}\mathrm{C}$ exhibited significantly less PCM melt and lower maximum PCM temperature observed. Furthermore, the outlet temperature for $T_{inlet} = 26.6\,^{\circ}\mathrm{C}$ was lower than that of $T_{inlet} = 21.6\,^{\circ}\mathrm{C}$ between $t = 120\,\mathrm{s}$ to $480\,\mathrm{s}$. Therefore, the numerical results exemplified the adverse outcome of the frost formation for the eutectic system.

Thèse accessible à l'adresse : https://theses.insa-lyon.fr/publication/2024ISAL0034/these.pdf © [J. Jeong], [2024], INSA Lyon, tous droits réservés

Chapter 6

Conclusions and future views

6.1 Conclusions

The main objective of this manuscript was to analyze the feasibility of the eutectic refrigeration system to replace the conventional refrigeration units operated by fossil fuels for a refrigerated truck trailer for the transportation of the frozen foodstuff. Therefore, to analyze the feasibility, a numerical model capable of accurately predicting the flow field, temperature distributions, infiltration heat load into the system, formation of frost on top of the plates, and the phase change of the eutectic mixture during the door opening period for a truck trailer refrigerated with eutectic plate system was required. Firstly, an infiltration model was developed to predict the thermoaeraulic behavior of the air during the infiltration period for a refrigerated truck trailer. Then Eulerian-Eulerian granular multiphase model was used to develop a frost model capable of predicting the growth of the frost on top of a cold plate in terms of the frost thickness and density. The Eulerian-Eulerian granular multiphase frost model incorporated the $k-\omega$ SST turbulence model presented in the infiltration model to widen its applicable range of inlet air velocities. Finally, the solidification and melting model was consolidated with the Eulerian-Eulerian multiphase model as a UDF to predict the phase change of the eutectic mixture due to the heat transferred to the PCM by the energy released during the frost formation and the energy transferred from the infiltrating hot atmospheric air.

First, a numerical model has been developed and validated to predict the turbulent flow and heat transfer inside a refrigerated truck trailer equipped with eutectic plates. The model has been validated against the experimental data of Lafaye de Micheaux et *al*. [60]. It was shown that the 3D effects did not influence significantly the velocity and temperature distributions at the midplane of the doorway. The $k-\omega$ SST model slightly improved the predictions of the realizable $k-\epsilon$ model of Lafaye de Micheaux et *al*. [60]. Based on the developed model, a 2D model was adapted to optimize the configuration of the refrigeration system with the eutectic plates in terms of trailer and cargo temperatures by analyzing the air flow and the infiltration heat load into the refrigerated truck trailer during the door opening period. Without cargo, the configuration with the plates placed in series on the roof of the trailer noticeably improved the performance in terms of trailer temperature with respect to the configuration with the plates in series placed at the back. However, the presence of a cargo eliminates the recirculation zones that prevented the infiltration of the atmospheric air. Also, for the configuration with the plates placed on the roof, a lower initial velocity of the pre-existing flow inside the trailer was observed caused by the blockage of the flow due to the cargo. Therefore, the atmospheric air was

Thèse accessible à l'adresse : https://theses.insa-lyon.fr/publication/2024ISAL0034/these.pdf © [J. Jeong], [2024], INSA Lyon, tous droits réservés

able to infiltrate and increase the temperature of the trailer quicker and resulted in a higher maximum temperature observed for the cargo.

As the number of cargo boxes will progressively decrease during the delivery cycle, it is plausible that the configuration with the plates placed on the roof could improve the performance as the influence of the pre-existing flow seen without the cargo will progressively emerge. The influence of the cargo parameters such as cargo locations, dimensions, arrangements, etc, should be investigated into more details as it has a significant influence over the development of the pre-existing flow inside the trailer. Further development should include a multiphase model to account for both the humidity of air and the melting of the phase change material inside the plates. Another major concern is that the formation of frost along the plates could interfere with the heat transfer between the plates and the surrounding air.

Then as a second step, a numerical model has been developed and validated to predict the frost formation and the melting and solidification of the sub-zero eutectic plate. The Eulerian-Eulerian multiphase frost model has been validated against published experimental results [77; 75; 38; 78; 76]. As the solidification and melting model within the ANSYS FLUENT cannot be activated with the Eulerian-Eulerian multiphase model, the solidification and melting model has been incorporated into the specific heat equation by a UDF into the multiphase model and validated against published numerical and experimental results [11; 82]. Then the combined model was experimentally validated for the frost thickness and the PCM temperature.

From both the numerical and experimental results, the key findings are as follows:

- If the airflow is above the PCM, heat is conducted to the PCM solely by conduction, apart from the minor buoyancy driven convection at the sides of the PCM caused by the temperature driven density difference by the heat transferred to the sides of the PCM by the surrounding aluminum encasing. This results in a highly localized high temperature zone at the upper region of the PCM, effectively nullifying its effect. Furthermore, due to the volumetric change during the phase change of the PCM, loss of contact between the PCM and the plate is observed. This would require an additional mechanical system to address the issue and add onto the cost of the system. To effectively diffuse the heat and utilize the PCM system, air flow should be at the sides or beneath the PCM in order to promote the convection caused by the temperature-driven density difference or by the formation of the Rayleigh-Bénard convection cells.

- For the sub-zero eutectic plates at initial temperature of $T = -30\,^{\circ}\mathrm{C}$, for typical summer delivery temperature of $T = 21.6\,^{\circ}\mathrm{C}$, relative humidity of 69 %, and velocity of $10\,\mathrm{m\,s^{-1}}$ caused by the buoyancy effect of the infiltration and the remaining influence of the air fans, linear relationship between the PCM liquid fraction and time can be observed. For typical door opening period of $t = 900\,\mathrm{s}$ [65; 86], liquid fraction of up to 0.1634 can be expected. Even for a short door opening period of $t = 120\,\mathrm{s}$, 2.3% of liquid fraction can be expected. Additionally, at $t = 180\,\mathrm{s}$, maximum PCM temperature of $T = -18\,^{\circ}\mathrm{C}$ is observed. As the maximum regulated temperature for quick (deep) frozen foodstuffs is $T = -18\,^{\circ}\mathrm{C}$ [2], ineffectiveness of certain regions of the plate to meet the regulated temperature requirements due to the inhomogeneous melting of the PCM can be expected. This addresses the importance of short door opening times for the delivery of the refrigerated frozen goods and employment of heat-infiltration deterrence mechanisms such as air curtains.

Thèse accessible à l'adresse : https://theses.insa-lyon.fr/publication/2024ISAL0034/these.pdf © [J. Jeong], [2024], INSA Lyon, tous droits réservés

- From the comparison of the results between the inlet temperatures of $T_{inlet} = 21.6\,°C$ and $T_{inlet} = 26.6\,°C$, it was demonstrated that the majority of the PCM melting was due to frost formation. For $T_{inlet} = 21.6\,°C$ higher frost mass and outlet temperature were observed until $t = 540\,s$, resulting in higher melting of the PCM than that for $T_{inlet} = 26.6\,°C$. For $T_{inlet} = 26.6\,°C$, due to the higher time and energy required to cool the air to reach the supersaturated state caused by the higher initial temperature of the air, less frost was formed on top of the eutectic system than for $T_{inlet} = 21.6\,°C$ until $t = 480\,s$. Therefore, most of the PCM melting was due to the cooling of air, resulting in a lower outlet temperature than that of $T_{inlet} = 21.6\,°C$ even with the 5 K higher inlet temperature. Additionally, only 4 % of PCM was melt for $T_{inlet} = 26.6\,°C$. Therefore, the adverse outcomes of the frost formation on the eutectic system were exemplified.

Additionally, the Eulerian-Eulerian frost model showed difficulty when the temperature difference between the air and the cold plate was below $25K$ for the tested operating conditions. The model can be further improved by optimizing the equation of the non-dimensional frosting criterion coefficient, B. However, significant efforts are required to repeat the simulations with varying coefficient values. It would also require many validation cases with various operating conditions and configurations to be applied as a generalized model for the frosting process. Furthermore, identifying the exact range of Reynolds number for the application of the $k-\omega$ SST turbulence model will be a difficult task.

In conclusion, eutectic system is capable of replacing the conventional refrigeration systems operated by consuming fossil-fuels for the refrigerated truck trailers for the transportation of frozen foodstuff. However, as the results indicated, there are number of constraints. Primarily, the door opening period must be strictly controlled and be less than t =180 s for the simulated conditions to meet the regulated temperature. This can be further increased by the application of the infiltration deterrence mechanisms such as air curtains. Secondly, eutectic plates places in parallel at the back of the trailer (Configuration A in Chapter 3) is more suitable than the plates places in series along the roof of the trailer (Configuration B in Chapter 3). While Configuration B performed slightly better than Configuration A in terms of the renewal time without the cargo, the infiltration model in Chapter 3 assumed the plate to be a constant temperature plate. From Chapter 5 it was shown that without convection, heat transfer between the PCM and the surrounding system is primarily via conduction. For Configuration B, convection will only occur along the bottom and sides of the eutectic plates. For the upper portion of the plate, heat transfer will be solely due to conduction. Additionally, if a mechanism accounting for the volumetric change of the PCM due to the phase change is not incorporated, there will be a loss of contact between the PCM and the top wall of the eutectic plate. Therefore, upper portion of the eutectic plates in any configuration can be seen as ineffective. As for the Configuration A, eutectic plates are placed in parallel at the back of the trailer with the length of the upper portion of the plate being minimal. Therefore, heat transfer between the PCM and the surrounding system will be far more effective for the Configuration A.

Thèse accessible à l'adresse : https://theses.insa-lyon.fr/publication/2024ISAL0034/these.pdf © [J. Jeong], [2024], INSA Lyon, tous droits réservés

6.2 Future Works and Challenges

The numerical model for the frost formation developed in this work currently relies on the non-dimensional frosting criterion coefficient, B. This coefficient has been determined through an iterative process of trial-and-error against the published experimental results. Therefore, the accuracy of the numerical model heavily relies on the validity of the non-dimensional frosting criterion coefficient. To improve the model, larger dataset containing the frost thickness and density for a wide range of variation of input parameters, such as inlet velocity, relative humidity, inlet air temperature, cold plate temperature, etc., are required. Given such dataset, the non-dimensional frosting criterion coefficient can be further refined for a model with better accuracy and wider applicability. However, feasibility of such task is subjected by the quantity of the available published experimental results and the computational time and cost associated with the trial-and-error process.

Furthermore, the numerical model for the frost formation only considers desublimation as the sole phase change phenomena occurring during the simulation. As the scope of this research was for the transport of frozen foodstuff with the temperature of the refrigerated truck trailer set to be approximately $-30\,^{\circ}\mathrm{C}$ according to the ATP requirement [2], condensation was neglected. However, given the temperature range shown during the experimentation, condensation inevitably occurs. This is further hindered by the lowered accuracy of the frost model with the lower difference between the plate temperature and the air. Therefore, condensation could also be incorporated into the model. However, as the interaction between the condensed water droplets and the frost has to be accounted for, the complexity and the computational cost of the numerical model will significantly increase.

Finally, for the numerical model, the infiltration model developed to predict the thermoaeraulic behavior of air during the door opening period of a refrigerated truck trailer and the frost formation and the solidification and melting model can be amalgamated to create a complete numerical model of a refrigerated truck trailer equipped with eutectic plates. This was the ultimate goal of the given research. However, there are several difficulties that must be overcome. Majorly, the grid size required for the frost formation model and the infiltration is significantly different. While for the infiltration model, the size of the grid cell must be sufficiently small enough to satisfy $y+ < 1$ for the $k-\omega$ SST turbulence model, the grid size is required to be significantly smaller for the frost formation model to be accurate in terms of the frost thickness and density. For the 2D infiltration model, 9.0×10^5 elements were required for the gird-independent results. Therefore, the complete model will be significantly limited by the computational time and resources available. As a solution, dynamic mesh could be incorporated to satisfy the cell size conditions and reduce the computational cost. Alternatively, the numerical model can be separated by the eutectic system and the refrigerated truck trailer, with a coupled iterations and solutions from each time step. However, the computational time and the complexities associated with either of the solutions still remains significantly high. Furthermore, the inner walls of the trailer and the cargo will also accumulate frost. However, the existing frost model only considers the average temperature of the eutectic plate. Thus, it is necessary to separately incorporate the frost model for the walls and cargo. This implementation will incur additional computational cost, as the cell size requirements also apply to the areas adjacent to the walls and cargo.

Experimentally, equipment acquisition and availability will the be major concern. Initially, investigation of the humidity diffusion during the door opening period of a refriger-

Thèse accessible à l'adresse : https://theses.insa-lyon.fr/publication/2024ISAL0034/these.pdf © [J. Jeong], [2024], INSA Lyon, tous droits réservés

ated truck trailer was planned for the research at INSA Lyon. However, the time-response of the humidity sensor was a major concern. As the infiltration phenomena occurs within the first five to ten seconds of the door opening, humidity sensor with the response time of less than one second was required. While such humidity sensors were acquired, major challenge was developing a data acquisition system with the given humidity sensors. The acquisition system needed to communicate with each sensor and relay the acquired data in a time frame much less than the response time of the humidity sensor in order to have no-delay in the acquired data. Developing aforementioned data acquisition system was outside the realm of this research, and required speciality of the professionals in electrical engineering. But given the availability of the personnel, cost of the equipment, etc., the experiment was postponed for the future researcher.

For the frost formation experiment performed at the Université de Sherbrooke, the major challenge was the thermal capability of the Thermo Bath required to completely freeze the PCM. Thermo Bath (Thermo Haake ARCTIC AC200 A40 Immersion Bath) with 900 W cooling capacity at 20 °C used the during the experiment was incapable of freezing any PCM below the phase change temperature of $T = -10\,^{\circ}\mathrm{C}$. Initially, Rubitherm SP-28 with the phase change temperature of $T = -28\,^{\circ}\mathrm{C}$ was planned to be used for the experiment. However, eutectic mixture of potassium bicarbonate was adopted due to the limitation of the Thermo Bath. As the initial plate temperature is at minimum $T = -10\,^{\circ}\mathrm{C}$, temperature difference between the plate and the air was limited. Due to this, condensation was observed during the experimentation and it effected the validation process between the numerical model and the experiment as the numerical model did incorporate the condensation effect. Ideally, Rubitherm SP-28 with the phase change temperature of $T = -28\,^{\circ}\mathrm{C}$ would have been used for the experiment, where no condensation would assumed to have occurred. As a solution, a smaller version of the experimental setup with the Peltier elements as a cooling mechanism was proposed. If the Peltier elements are used as the cooling mechanism, it does not require a coil-pipe system within the PCM container unlike Thermo Bath. Therefore, the size of the PCM container will not be limited. With the lowered volume of the PCM, required amount of heat to be removed from the system will also be reduced. However, the acquirement of the Peltier elements, development of the control systems, etc., would take significant amount of time.

Thèse accessible à l'adresse : https://theses.insa-lyon.fr/publication/2024ISAL0034/these.pdf © [J. Jeong], [2024], INSA Lyon, tous droits réservés

Thèse accessible à l'adresse : https://theses.insa-lyon.fr/publication/2024ISAL0034/these.pdf © [J. Jeong], [2024], INSA Lyon, tous droits réservés

Chapter 7

Conclusions et perspectives (Version Française)

7.1 Conclusions

L'objectif principal de ce manuscrit était d'analyser la faisabilité d'un système de réfrigération à base de plaques eutectiques pour remplacer les unités de réfrigération conventionnelles fonctionnant aux combustibles fossiles dans une remorque de camion réfrigérée pour le transport de produits alimentaires surgelés. Pour cela, un modèle numérique capable de prédire avec précision le champ d'écoulement, la distribution de température, la charge thermique due aux infiltrations, la formation de givre sur les plaques et le changement de phase du mélange eutectique pendant la période d'ouverture des portes a été développé. Un nouveau banc expérimental de plaque eutectique a également été construit à l'Université de Sherbrooke afin de valider les modèles numériques de formation de givre et de fusion du matériau à changement de phase.

Dans un premier temps, un modèle d'infiltration a été développé pour prédire le comportement thermoaéraulique de l'air pendant les périodes d'ouverture de la remorque. Il a été soigneusement validé par rapport aux données expérimentales de Lafaye de Micheaux et *al*. [60]. Il a été démontré que les effets 3D n'influencent pas de manière significative les distributions de vitesse et de température au niveau du plan médian de la porte. Le modèle $k-\omega$ SST a légèrement amélioré les prédictions du modèle réalisable $k-\epsilon$ de Lafaye de Micheaux et *al*. [60]. Sur la base du modèle développé, un modèle 2D a été adapté pour optimiser la configuration du système de réfrigération avec les plaques eutectiques en termes de températures à l'intérieur de la remorque et de la cargaison en analysant le flux d'air et la charge thermique d'infiltration dans la remorque frigorifique du camion pendant la période d'ouverture des portes. Sans chargement, la configuration avec les plaques placées horizontalement en série au plafond de la remorque a sensiblement amélioré les performances en termes de température de la remorque par rapport à la configuration avec les plaques en série placées verticalement à l'arrière. Cependant, la présence d'une cargaison élimine les zones de recirculation qui empêchent l'infiltration de l'air atmosphérique lors des périodes d'ouverture. De plus, pour la configuration avec les plaques placées au plafond, une vitesse initiale plus faible du flux préexistant à l'intérieur de la remorque a été observée, causée par la présence la cargaison. Par conséquent, l'air atmosphérique a pu s'infiltrer et augmenter la température de la remorque plus rapidement, ce qui a entraîné une température maximale plus élevée pour la cargaison. Comme le nombre de caisses diminuera progressivement au cours du cycle de livraison, il est plausible que la

Thèse accessible à l'adresse : https://theses.insa-lyon.fr/publication/2024ISAL0034/these.pdf © [J. Jeong], [2024], INSA Lyon, tous droits réservés

configuration avec les plaques placées au plafond puisse améliorer les performances au fur et à mesure que l'influence du flux préexistant sans la cargaison émerge progressivement.

Dans un deuxième temps, un second modèle numérique a été développé et validé pour prédire la formation de givre au-dessus des plaques eutectiques ainsi que la fusion et la solidification du matériau à changement de phase au sein de la plaque. Le modèle de givre de type eulérien-eulérien a été validé par rapport à des résultats expérimentaux disponibles dans la littérature [77; 75; 38; 78; 76] pour une large gamme de conditions d'opération. Comme le modèle de solidification et de fusion d'ANSYS FLUENT n'est pas compatible avec le modèle eulérien-eulérien, le modèle de solidification et de fusion a été incorporé dans l'équation de la chaleur spécifique via une fonction utilisateur (UDF). Il a ensuite été validé par rapport à d'autres données numériques et expérimentales de la littérature [11; 82]. Enfin, le modèle combiné a été validé en termes d'épaisseur du givre et de température du matériau à changement de phase par des données expérimentales issues d'un nouveau banc expérimental construit spécifiquement à l'Université de Sherbrooke. Les principales conclusions de cette seconde phase sont les suivantes:

- Si le flux d'air est au-dessus du MCP, la chaleur est conduite vers le MCP essentiellement par conduction, à l'exception de la convection mineure générée sur les côtés de la boîte. Il en résulte une zone de température élevée très localisée dans la région supérieure du MCP. De plus, en raison du changement de volume induit par le changement de phase du MCP, une perte de contact entre le MCP et la plaque est observée. Pour diffuser efficacement la chaleur et utiliser pleinement le système, le flux d'air doit être sur les côtés ou sous la plaque afin de favoriser les transferts par convection.

- Pour des plaques eutectiques à une température initiale de $T = -30\,^{\circ}\mathrm{C}$ et une température extérieure en été typique de $T = 21.6\,^{\circ}\mathrm{C}$, une humidité relative de 69 % et une vitesse de l'air de $10\,\mathrm{m\,s^{-1}}$, on peut obtenir une relation linéaire entre la fraction de MCP qui a fondu et le temps. Pour une période typique d'ouverture de porte de $t = 900\,\mathrm{s}$[65; 86], on peut s'attendre à une fraction fondue allant jusqu'à 0.163. Même pour une courte période d'ouverture de porte de $t = 120\,\mathrm{s}$, on peut s'attendre à 2.3% de MCP fondu. De plus, à $t = 180\,\mathrm{s}$, une température maximale du MCP de $T = -18\,^{\circ}\mathrm{C}$ est observée. Comme la température maximale acceptable pour les aliments surgelés est de $T = -18\,^{\circ}\mathrm{C}$ [2], les inhomogénéités de température au sein de la plaque peuvent rendre le système inefficace pour garantir cette température au sein de la remorque. Cela démontre l'importance d'avoir des temps d'ouverture des portes courts lors de la livraison des produits surgelés et/ou d'employer des systèmes additionnels pour isoler la remorque de l'extérieur, comme des rideaux en plastique ou des rideaux d'air.

- De la comparaison des résultats entre les températures d'entrée de $T_{inlet} = 21.6\,^{\circ}\mathrm{C}$ et $T_{inlet} = 26.6\,^{\circ}\mathrm{C}$, il a été démontré que la majorité de la fonte du MCP était due à la formation de givre. Pour $T_{inlet} = 21.6\,^{\circ}\mathrm{C}$, une masse de givre et une température de sortie plus élevées ont été observées jusqu'à $t = 540\,\mathrm{s}$, ce qui a entraîné une fusion du MCP plus élevée que celle de $T_{entre} = 26.6\,^{\circ}\mathrm{C}$. Pour $T_{inlet} = 26.6\,^{\circ}\mathrm{C}$, en raison du temps et de l'énergie plus élevés nécessaires pour refroidir l'air afin d'atteindre l'état sursaturé provoqué par la température initiale plus élevée de l'air, du givre s'est formé au-dessus du système eutectique, mais son épaisseur était inférieure à

Thèse accessible à l'adresse : https://theses.insa-lyon.fr/publication/2024ISAL0034/these.pdf © [J. Jeong], [2024], INSA Lyon, tous droits réservés

celle obtenue pour $T_{inlet} = 21.6\,°C$ jusqu'à $t = 480\,s$. Par conséquent, la majeure partie de la fusion du MCP était due au refroidissement de l'air, ce qui faisait que la température de sortie était inférieure à celle de $T_{inlet} = 21.6\,°C$ même avec le $5\,K$ température d'entrée plus élevé. De plus, seulement 4 % du MCP a fondu pour $T_{inlet} = 26.6\,°C$. Ainsi, les conséquences néfastes de la formation de givre sur le système eutectique ont été illustrées.

De plus, le modèle de givre eulérien-eulérien a montré des difficultés à prédire de façon précise l'épaisseur de givre lorsque la différence de température entre l'air et la plaque froide était inférieure à $25K$ pour les conditions de fonctionnement testées. Le modèle peut être encore amélioré en optimisant l'équation du coefficient du critère de givrage adimensionnel, B. Cependant, des efforts importants sont nécessaires pour répéter les simulations avec des valeurs variables de ce coefficient. Cela nécessiterait également de nombreux cas de validation avec diverses conditions de fonctionnement pour être appliqués comme modèle généralisé pour le processus de givrage.

En conclusion, le système eutectique est capable de remplacer les systèmes de réfrigération conventionnels dans les remorques frigorifiques destinées au transport de produits surgelés. Cependant, comme l'indiquent les résultats, il existe un certain nombre de contraintes. Principalement, la période d'ouverture de la porte doit être strictement contrôlée et être inférieure à t =180 s pour respecter la température cible au sein de la remorque. Les infiltrations peuvent être réduites par l'ajout de systèmes comme des rideaux en plastique ou des rideaux d'air. Deuxièmement, les plaques eutectiques placées en parallèle à l'arrière de la remorque (Configuration A au Chapitre 3) sont plus adaptées que les plaques placées en série le long du plafond de la remorque (Configuration B au Chapitre 3). Alors que la configuration B a donné des résultats légèrement meilleurs que la configuration A en termes de temps de renouvellement sans la cargaison, le modèle d'infiltration du Chapitre 3 a supposé que la plaque était une plaque à température constante. Au chapitre 5, il a été montré que sans convection, le transfert de chaleur entre le MCP et le système environnant se fait principalement par conduction. Pour la configuration B, la convection ne se produira que le long du fond et des côtés des plaques eutectiques. Pour la partie supérieure de la plaque, le transfert de chaleur se fera uniquement par conduction. De plus, si un mécanisme prenant en compte le changement volumétrique du MCP dû au changement de phase n'est pas incorporé, il y aura une perte de contact entre le MCP et la paroi supérieure de la plaque eutectique. Par conséquent, la partie supérieure des plaques eutectiques, quelle que soit leur configuration, peut être considérée comme inefficace. Dans la configuration A, les plaques eutectiques sont placées verticalement parallèlement à l'arrière de la remorque. La longueur de la partie supérieure de la plaque étant minimale, le transfert de chaleur entre le MCP et l'air dans la remorque sera beaucoup plus efficace que pour la configuration A.

7.2 Perspectives de travail

Concernant le modèle d'infiltration développé pour prédire le comportement thermoaéraulique de l'air pendant la période d'ouverture des portes de la remorque, l'influence des paramètres liés à la cargaison (emplacement, dimensions, disposition, etc.) devrait être étudiée plus en détail car elle a une influence significative sur le développement du flux préexistant à l'intérieur de la remorque. L'évolution temporelle de la température du chargement reste, de plus, le paramètre principal à prédire pour vérifier qu'elle reste dans une plage

Thèse accessible à l'adresse : https://theses.insa-lyon.fr/publication/2024ISAL0034/these.pdf © [J. Jeong], [2024], INSA Lyon, tous droits réservés

acceptable par rapport aux exigences ATP [2]. Le rayonnement entre surfaces au sein de la remorque, bien qu'à priori faible, pourrait être également intégré au modèle final.

Le modèle numérique de formation de givre développé dans ce travail repose actuellement sur un coefficient de critère de givrage non dimensionnel, B. Ce coefficient a été déterminé par un processus itératif d'essais et erreurs par rapport à une série de résultats expérimentaux. La précision du modèle numérique dépend fortement de la validité de ce coefficient B. Pour améliorer le modèle, un ensemble de données plus grand contenant l'épaisseur et la densité du givre pour une large gamme des paramètres d'opération, comme la vitesse d'entrée, l'humidité relative, la température de l'air d'entrée, la température de la plaque froide, etc, est nécessaire afin d'affiner le coefficient B.

De plus, le présent modèle numérique de formation de givre ne considère que la désublimation comme seul phénomène de changement de phase. Comme le champ de cette recherche concernait le transport de produits alimentaires surgelés avec une température de la remorque du camion réfrigérée fixée à environ $-30\,°C$ selon l'exigence ATP [2], la condensation a été négligée. Cependant, étant donné la plage de température mesurée lors des expériences, de la condensation se produit inévitablement. Ceci est encore entravé par la précision réduite du modèle de givre, avec une différence plus faible entre la température de la plaque et celle de l'air. La condensation pourrait donc également être intégrée au modèle. Cependant, comme les interactions entre les gouttelettes d'eau condensée et le givre doivent être prise en compte, la complexité et le coût de calcul du modèle numérique vont augmenter considérablement.

Enfin, un modèle complet incorporant les différents modèles déjà développés représentait l'objectif principal de cette étude. Cependant, plusieurs difficultés doivent encore être surmontées. La principale est due à la différence d'échelles entre les phénomènes aéroliques à l'échelle de la remorque et la formation de givre à l'échelle millimétrique. Cela nécessite des maillages extrêmement fins et des coûts de calcul prohibitifs.En guise de solution, un maillage dynamique pourrait être incorporé pour satisfaire les conditions de taille de cellule et réduire le coût de calcul. Sinon, le modèle numérique peut être séparé en deux parties, une pour le système eutectique et une pour la remorque, avec des itérations couplées. Cependant, le temps de calcul et les complexités associées à l'une ou l'autre des solutions restent encore significativement élevés. De plus, les parois intérieures de la remorque et de la cargaison vont également accumuler du givre. Cependant, le modèle de givre existant ne considère que la température moyenne de la plaque eutectique. Ainsi, il est nécessaire d'incorporer séparément le modèle de givre pour les parois et la cargaison. Cette mise en œuvre entraînera un coût de calcul supplémentaire, car les exigences de taille de cellule s'appliquent également aux zones adjacentes aux parois de la remorque et de la cargaison.

Expérimentalement, une étude sur la diffusion de l'humidité pendant les périodes d'ouverture des portes de la remorque était prévue initialement à l'INSA de Lyon. Cependant, la réponse temporelle du capteur d'humidité constituait une préoccupation majeure. Étant donné que le phénomène d'infiltration se produit dans les cinq à dix secondes suivant l'ouverture des portes, un capteur d'humidité avec un temps de réponse inférieur à une seconde était nécessaire. Le défi majeur consistait à développer le système d'acquisition de données correspondant. Le système d'acquisition devait communiquer avec chaque capteur et relayer les données acquises dans un laps de temps bien inférieur au temps de réponse des capteurs d'humidité afin de n'avoir aucun retard. Le développement du système d'acquisition de données reste à développer avant d'initier cette étude.

Pour l'expérience sur la formation de givre réalisée à l'Université de Sherbrooke, le

Thèse accessible à l'adresse : https://theses.insa-lyon.fr/publication/2024ISAL0034/these.pdf © [J. Jeong], [2024], INSA Lyon, tous droits réservés

défi majeur était la puissance du bain thermostaté requise pour solidifier complètement le MCP. Le bain d'immersion (Thermo Haake ARCTIC AC200 A40) ayant une capacité de refroidissement de 900 W à 20 °C était incapable de solidifier un MCP en dessous de la température de changement de phase de $T = -10\,°C$. Initialement, il était prévu d'utiliser le Rubitherm SP-28 avec une température de changement de phase de $T = -28\,°C$ pour l'expérience. Cependant, un mélange eutectique de bicarbonate de potassium a été adopté en raison des limites du bain thermique. Comme la température initiale de la plaque est au minimum de $T = -10\,°C$, la différence de température entre la plaque et l'air reste limitée. Pour cette raison, de la condensation a été observée au cours de l'expérimentation. Idéalement, le MCP Rubitherm SP-28 avec une température de changement de phase de $T = -28\,°C$ aurait été utilisé pour l'expérience. Comme solution, une version plus petite du dispositif expérimental avec des éléments Peltier comme mécanisme de refroidissement a été proposée. Si des éléments Peltier sont utilisés, ils ne nécessitent pas de système de serpentin-tuyau dans le conteneur MCP contrairement à la solution avec le bain thermostaté. Par conséquent, la taille du conteneur MCP ne sera pas limitée. Avec le volume réduit du MCP, la quantité de chaleur requise à éliminer du système sera également réduite. Ce nouveau banc expérimental serait intéressant à développer afin d'étendre la campagne de mesures à d'autres conditions d'opération tout en mesurant la masse de givre produite.

Thèse accessible à l'adresse : https://theses.insa-lyon.fr/publication/2024ISAL0034/these.pdf © [J. Jeong], [2024], INSA Lyon, tous droits réservés

Thèse accessible à l'adresse : https://theses.insa-lyon.fr/publication/2024ISAL0034/these.pdf © [J. Jeong], [2024], INSA Lyon, tous droits réservés

Appendix A

List of Publications

Journal Article:

- J. Jeong, A.E. Benchikh Le Hocine, S. Croquer, S. Poncet, B. Michel, J. Bonjour. Numerical analysis of the thermoaeraulic behavior of air during the opening of the door of a refrigerated truck trailer equipped with cold plates. *Applied Thermal Engineering*, **206**, 118057, 2022.

Conferences:

- J. Jeong, S. Poncet, B. Michel, J. Bonjour. Numerical simulation of the frost formation on a flat plate cooled by a phase change material, *26th International Congress of Refrigeration (ICR23)*, Paris, 2023.
- J. Jeong, S. Poncet, B. Michel, J. Bonjour. Eulerian-Eulerian Multiphase Frost Model Based on Phase Change Driving Force. *7th IIR International Conference on Sustainability and the Cold Chain*, Newcastle, 2022.
- J. Jeong, A.E. Benchikh Le Hocine, S. Croquer, S. Poncet, J. Bonjour, B. Michel. Numerical Simulation of the Heat Transfer in a Refrigerated Trailer Equipped with Eutectic Plates for Frozen Food Delivery. *18th International Refrigeration and Air Conditioning Conference*, Lafayette, 2021.

Thèse accessible à l'adresse : https://theses.insa-lyon.fr/publication/2024ISAL0034/these.pdf © [J. Jeong], [2024], INSA Lyon, tous droits réservés

Thèse accessible à l'adresse : https://theses.insa-lyon.fr/publication/2024ISAL0034/these.pdf © [J. Jeong], [2024], INSA Lyon, tous droits réservés

List of figures

Thèse accessible à l'adresse : https://theses.insa-lyon.fr/publication/2024ISAL0034/these.pdf © [J. Jeong], [2024], INSA Lyon, tous droits réservés

Thèse accessible à l'adresse : https://theses.insa-lyon.fr/publication/2024ISAL0034/these.pdf © [J. Jeong], [2024], INSA Lyon, tous droits réservés

Thèse accessible à l'adresse : https://theses.insa-lyon.fr/publication/2024ISAL0034/these.pdf © [J. Jeong], [2024], INSA Lyon, tous droits réservés

Thèse accessible à l'adresse : https://theses.insa-lyon.fr/publication/2024ISAL0034/these.pdf © [J. Jeong], [2024], INSA Lyon, tous droits réservés

List of tables

nomenclature[z-URANS]URANSUnsteady Reynolds-averaged Navier–Stokes

Thèse accessible à l'adresse : https://theses.insa-lyon.fr/publication/2024ISAL0034/these.pdf © [J. Jeong], [2024], INSA Lyon, tous droits réservés

Thèse accessible à l'adresse : https://theses.insa-lyon.fr/publication/2024ISAL0034/these.pdf © [J. Jeong], [2024], INSA Lyon, tous droits réservés

Nomenclature

Roman Symbols

A	Cross sectional area of the door [m^2]
A_{mush}	Mushy zone constant [-]
B	Non-dimensional frosting criterion coefficient [-]
b	Thickness of the door frame [m]
C_p	Specific heat capacity [$J\,kg^{-1}\,K^{-1}$]
d	Diameter [m]
D_{H_2O}	Diffusivity of the water vapour [$m^2\,s^{-1}$]
E	Heat transfer coefficient [$W\,m^{-2}\,K^{-1}$]
f	Drag function [-]
g	Gravitational Acceleration [$9.81\,m\,s^{-2}$]
H	Height [m]
h	Enthalpy [$J\,kg^{-1}$]
I	Infiltration [m^3]
$\dot{I}$	Infiltration rate [$m^3\,s^{-1}$]
K	Momentum transfer coefficient [-]
$K_{f,L}$	Fritsche and Lilienblum correction factor [-]
k	Turbulence kinetic energy [$m^2\,s^{-2}$]
L	Length [m]
m	Mass [kg]
$\dot{m}$	Mass transfer rate [$kg\,s^{-1}$]
Nu	Nusselt number [-]
P	Pressure [Pa]
Pr	Prandtl number [-]
$\bar{Q}$	Interphase heat transfer [$W\,m^{-3}$]
Q	Heat [J]
$\dot{Q}$	Heat load [W]
$\vec{q}$	Heat flux [$W\,m^{-2}$]
R	Specific gas constant [$287\,J\,kg^{-1}\,K^{-1}$]
Re	Reynolds number [-]
$\bar{r}$	Droplet radius [m]
r^*	Kelvin-Helmholtz critical radius [m]
S	Source term
T	Temperature [K]
t	Time [s]
V	Volume [m^3]
v	Velocity [$m\,s^{-1}$]
W	Width [m]
w	Mass fraction [-]
y+	Non-dimensional wall distance [-]

Greek Symbols

α	Volume fraction [-]
δ	Frost thickness [mm]
$\frac{\delta\bar{r}}{\delta t}$	Nucleation growth rate
ϵ	Dissipation rate of k [$m^2\,s^{-3}$]
η	Number of droplets per unit volume [m^{-3}]

Thèse accessible à l'adresse : https://theses.insa-lyon.fr/publication/2024ISAL0034/these.pdf © [J. Jeong], [2024], INSA Lyon, tous droits réservés

λ	Thermal conductivity [$\mathrm{W\,m^{-1}\,K^{-1}}$]
μ	Dynamic viscosity [$\mathrm{Pa\,s^{-1}}$]
ρ	Density [$\mathrm{kg\,m^{-3}}$]
$\bar{\tau}$	Stress-strain tensor [Pa]
τ_v	Time relaxation coefficient [-]
ϕ	Liquid fraction [-]
χ	Small number, 0.001
ω	Specific turbulence dissipation rate [$\mathrm{s^{-1}}$]

Subscripts

0	Initial
a	Air
ac	Air to ice
avg	Average
ca	Ice to air
c	Ice
da	Dry air
h	Energy
i	Inner
in	Inlet
L	Latent
l	Liquid
m	Mass
n	Normal
o	Outer
s	Sensible
total	Total
p	Plate
ref	Reference
sens	Sensible
s	Solid
u	Momentum
va	Water vapour
vs	Saturated water vapour
v	Specie
w	Wall

Acronyms / Abbreviations

ATP	Agreement on the International Carriage of Perishable Foodstuffs and on the Special Equipment to be used for such Carriage
CFD	Computational Fluid Dynamics
COP	Coefficient of Performance
CTE	Coefficient of Thermal Expansion [$\mathrm{K^{-1}}$]
PCM	Phase Change Material
PU	Polyurethane
RH	Relative Humidity
RMS	Root Mean Square
RSM	Reynolds Stress Model
SST	Shear Stress Transport
UDF	User Defined Function
VOF	Volume of Fluid

Thèse accessible à l'adresse : https://theses.insa-lyon.fr/publication/2024ISAL0034/these.pdf © [J. Jeong], [2024], INSA Lyon, tous droits réservés

Bibliography

[1] S. Tassou, J. Lewis, Y. Ge, A. Hadawey, I. Chaer, A review of emerging technologies for food refrigeration applications, Applied Thermal Engineering 30 (4) (2010) 263–276.

[2] UN Economic Commission for Europe – Inland Transport Committee, ATP as amended on 6 January 2018 – Agreement on the International Carriage of Perishable Foodstuff and on the Special Equipment to be used for such Carriage, Tech. rep. (2018).

[3] S. Tassou, G. De-Lille, Y. Ge, Food transport refrigeration–approaches to reduce energy consumption and environmental impacts of road transport, Applied Thermal Engineering 29 (8-9) (2009) 1467–1477.

[4] S. Croquer, A. Benchikh Le Hocine, S. Poncet, Numerical modelling of heat and mass transfer in a refrigerated truck trailer, in: Proc. of the 25th IIR International Congress of Refrigeration, Montreal, 2019, pp. 3574–3581.

[5] X. Wu, Q. Ma, F. Chu, S. Hu, Phase change mass transfer model for frost growth and densification, International Journal of Heat and Mass Transfer 96 (2016) 11–19.

[6] A. Rai, S. Tassou, Environmental impacts of vapour compression and cryogenic transport refrigeration technologies for temperature controlled food distribution, Energy Conversion and Management 150 (2017) 914–923.

[7] T. Goswami, V. Raj, Use of phase change material (PCM) for the improvement of thermal performance of cold storage, MOJ Current Research & Reviews 1 (2018) 49–61.

[8] R. Chaturvedi, A. Islam, K. Sharma, A review on the applications of PCM in thermal storage of solar energy, Materials Today: Proceedings 43 (2021) 293–297.

[9] P. Singh, R. Sharma, A. Ansu, R. Goyal, A. Sari, V. Tyagi, A comprehensive review on development of eutectic organic phase change materials and their composites for low and medium range thermal energy storage applications, Solar Energy Materials and Solar Cells 223 (2021) 110955.

[10] M. Mofijur, T. Mahlia, A. Silitonga, H. Ong, M. Silakhori, M. Hasan, N. Putra, S. Rahman, Phase change materials (PCM) for solar energy usages and storage: an overview, Energies 12 (16) (2019) 3167.

[11] M. Fadl, P. Eames, Numerical investigation of the influence of mushy zone parameter amush on heat transfer characteristics in vertically and horizontally oriented thermal energy storage systems, Applied Thermal Engineering 151 (2019) 90–99.

Thèse accessible à l'adresse : https://theses.insa-lyon.fr/publication/2024ISAL0034/these.pdf © [J. Jeong], [2024], INSA Lyon, tous droits réservés

[12] A. Brent, V. Voller, K. Reid, Enthalpy-porosity technique for modeling convection-diffusion phase change: application to the melting of a pure metal, Numerical Heat Transfer, Part A Applications 13 (3) (1988) 297–318.

[13] ANSYS FLUENT 12.0, Theory Guide (2009) 67.

[14] O. Zarajabad, R. Ahmadi, Numerical investigation of different PCM volume on cold thermal energy storage system, Journal of Energy Storage 17 (2018) 515–524.

[15] J. Gou, J. Lin, Y. Jiang, S. Mei, J. Xia, S. Lin, Q. Shen, X. Zhang, W. Cai, J. Liang, et al., Numerical analysis of cold energy release process of cold storage plate in a container for temperature control, Journal of Energy Storage 71 (2023) 108230.

[16] M. Calati, G. Righetti, C. Zilio, K. Hooman, S. Mancin, CFD analyses for the development of an innovative latent thermal energy storage for food transportation, International Journal of Thermofluids 17 (2023) 100301.

[17] V. Voller, C. Prakash, A fixed grid numerical modelling methodology for convection-diffusion mushy region phase-change problems, International Journal of Heat and Mass Transfer 30 (8) (1987) 1709–1719.

[18] J. Vogel, J. Felbinger, M. Johnson, Natural convection in high temperature flat plate latent heat thermal energy storage systems, Applied Energy 184 (2016) 184–196.

[19] Y. Kim, A. Hossain, S. Kim, Y. Nakamura, A numerical study on time-dependent melting and deformation processes of Phase Change Material (PCM) induced by localized thermal input, INTECH Open Access Publisher, 2011.

[20] R. Oliveski, F. Becker, L. Rocha, C. Biserni, G. Eberhardt, Design of fin structures for phase change material (PCM) melting process in rectangular cavities, Journal of Energy Storage 35 (2021) 102337.

[21] A. Abdulmunem, P. Samin, H. Rahman, H. Hussien, I. Mazali, H. Ghazali, Numerical and experimental analysis of the tilt angle's effects on the characteristics of the melting process of PCM-based as PV cell's backside heat sink, Renewable Energy 173 (2021) 520–530.

[22] H. Shokouhmand, B. Kamkari, Experimental investigation on melting heat transfer characteristics of lauric acid in a rectangular thermal storage unit, Experimental Thermal and Fluid Science 50 (2013) 201–212.

[23] A. Tinti, A. Tarzia, A. Passaro, R. Angiuli, Thermographic analysis of polyurethane foams integrated with phase change materials designed for dynamic thermal insulation in refrigerated transport, Applied Thermal Engineering 70 (1) (2014) 201–210.

[24] B. Copertaro, P. Principi, R. Fioretti, Thermal performance analysis of PCM in refrigerated container envelopes in the Italian context - Numerical modeling and validation, Applied Thermal Engineering 102 (2016) 873–881.

[25] B. Michel, P. Glouannec, A. Fuentes, P. Chauvelon, Experimental and numerical study of insulation walls containing a composite layer of PU-PCM and dedicated to refrigerated vehicle, Applied Thermal Engineering 116 (2017) 382–391.

Thèse accessible à l'adresse : https://theses.insa-lyon.fr/publication/2024ISAL0034/these.pdf © [J. Jeong], [2024], INSA Lyon, tous droits réservés

[26] M. Calati, C. Zilio, G. Righetti, G. Longo, K. Hooman, S. Mancin, A numerical analysis of latent thermal energy storage for refrigerated trucks, in: International Refrigeration and Air Conditioning Conference, Purdue, 2021.

[27] M. Berdja, A. Hamid, O. Sari, Characteristics and thickness effect of phase change material and frost on heat transfer and thermal performance of conventional refrigerator: Theoretical and experimental investigation, International Journal of Refrigeration 97 (2019) 108–123.

[28] Y. Hayashi, A. Aoki, S. Adachi, K. Hori, Study of frost properties correlating with frost formation types, Journal of Heat Transfer 99 (2) (1977) 239–245.

[29] D. Kim, C. Kim, K. Lee, Frosting model for predicting macroscopic and local frost behaviors on a cold plate, International Journal of Heat and Mass Transfer 82 (2015) 135–142.

[30] Y. Tao, R. Besant, K. Rezkallah, A mathematical model for predicting the densification and growth of frost on a flat plate, International Journal of Heat and Mass Transfer 36 (2) (1993) 353–363.

[31] B. Jones, J. Parker, Frost formation with varying environmental parameters, Journal of Heat Transfer 97 (1975) 255–259.

[32] D. O'Neal, D. Tree, Measurement of frost growth and density in a parallel plate geometry, ASHRAE Transactions 90 (2) (1984) 278–290.

[33] B. Na, R. Webb, New model for frost growth rate, International Journal of Heat and Mass Transfer 47 (5) (2004) 925–936.

[34] K. Lee, S. Jhee, D. Yang, Prediction of the frost formation on a cold flat surface, International Journal of heat and Mass Transfer 46 (20) (2003) 3789–3796.

[35] Y. Yao, Y. Jiang, S. Deng, Z. Ma, A study on the performance of the airside heat exchanger under frosting in an air source heat pump water heater/chiller unit, International Journal of Heat and Mass Transfer 47 (17-18) (2004) 3745–3756.

[36] A. Léoni, M. Mondot, F. Durier, R. Revellin, P. Haberschill, State-of-the-art review of frost deposition on flat surfaces, International Journal of Refrigeration 68 (2016) 198–217.

[37] B. Na, R. Webb, Mass transfer on and within a frost layer, International Journal of Heat and Mass Transfer 47 (5) (2004) 899–911.

[38] K.-S. Lee, W.-S. Kim, T.-H. Lee, A one-dimensional model for frost formation on a cold flat surface, International Journal of Heat and Mass Transfer 40 (18) (1997) 4359–4365.

[39] R. Barron, L. Han, Heat and mass transfer to a cryosurface in free convection, Journal of Heat Transfer 87 (4) (1965) 499–506.

[40] K. Lenic, A. Trp, B. Frankovic, Transient two-dimensional model of frost formation on a fin-and-tube heat exchanger, International Journal of Heat and Mass Transfer 52 (1-2) (2009) 22–32.

Thèse accessible à l'adresse : https://theses.insa-lyon.fr/publication/2024ISAL0034/these.pdf © [J. Jeong], [2024], INSA Lyon, tous droits réservés

[41] D. Yang, K. Lee, Modeling of frosting behavior on a cold plate, International Journal of Refrigeration 28 (3) (2005) 396–402.

[42] D. Yang, K. Lee, D. Cha, Frost formation on a cold surface under turbulent flow, International Journal of Refrigeration 29 (2) (2006) 164–169.

[43] J. Cui, W. Li, Y. Liu, Z. Jiang, A new time-and space-dependent model for predicting frost formation, Applied Thermal Engineering 31 (4) (2011) 447–457.

[44] J. Cui, W. Li, Y. Liu, Y. Zhao, A new model for predicting performance of fin-and-tube heat exchanger under frost condition, International Journal of Heat and Fluid Flow 32 (1) (2011) 249–260.

[45] D. Zhuang, G. Ding, H. Hu, H. Fujino, S. Inoue, Condensing droplet behaviors on fin surface under dehumidifying condition: Part I: Numerical model, Applied Thermal Engineering 105 (2016) 336–344.

[46] X. Wu, F. Chu, Q. Ma, Frosting model based on phase change driving force, International Journal of Heat and Mass Transfer 110 (2017) 760–767.

[47] E. Afrasiabian, O. Iliev, S. Lazzari, C. Isetti, Numerical simulation of frost formation on a plate-fin evaporator, in: Proceedings of the 3rd World Congress on Momentum, Heat and Mass Transfer (MHMT'18), Budapest, 2018, pp. 12–14.

[48] A. Sommers, N. Truster, A. Napora, A. Riechman, E. Caraballo, Densification of frost on hydrophilic and hydrophobic substrates–examining the effect of surface wettability, Experimental Thermal and Fluid Science 75 (2016) 25–34.

[49] A. Foster, M. Swain, R. Barrett, S. James, Experimental verification of analytical and CFD predictions of infiltration through cold store entrances, International Journal of Refrigeration 26 (8) (2003) 918–925.

[50] A. Azzouz, J. Gossé, M. Duminil, Détermination expérimentale des pertes de froid occasionnées par l'ouverture d'une porte de chamber froide industrielle, Revue Internationale du Froid 16 (1) (1993) 57—66.

[51] M. Bonaventure, A. Benchikh Le Hocine, S. Croquer, K. Huchtemann, S. Poncet, Heat and mass transfer in a loaded truck trailer equipped with eutectic plates: a comparative numerical study, in: Proc. of the 6th IIR Conference on Sustainability and the Cold Chain (ICCC2020), Nantes, 2020, pp. 494–499.

[52] J. Emswiler, The neutral zone in ventilation, in: Annual Meeting of the American Society of Heating and Ventilation Engineers, Buffalo, 1926, pp. 59–74.

[53] W. Brown, K. Solvason, Natural convection through rectangular openings in partitions—1: Vertical partitions, International Journal of Heat and Mass Transfer 5 (9) (1962) 859–868.

[54] W. Tamm, Kalterveluste durch Kuhlraumoffnungen, Kältetechnik-Klimatisierung 18 (1966) 142–144.

[55] C. Fritzsche, W. Lilienblum, Neue Messungen zur Bestimmung der Kälteverluste an Kühlraumtüren, Kältetechnik-Klimatisierung 20 (1968) 279–286.

Thèse accessible à l'adresse : https://theses.insa-lyon.fr/publication/2024ISAL0034/these.pdf © [J. Jeong], [2024], INSA Lyon, tous droits réservés

[56] W. Gosney, H. Olama, Heat and enthalpy gains through cold rooms doorways, in: Proc. of Institute of Refrigeration, Environmental Science and Technology, The Polytechnic of the South Bank, London, 1976.

[57] Q. Pham, D. Oliver, Infiltration of air into cold stores, in: Proc. of the 16th International Congress of Refrigeration, Vol. 4, West-Lafayette, 1983, pp. 67–72.

[58] W. Hendrix, D. Henderson, H. Jackson, Infiltration heat gains through cold storage room doorways, ASHRAE Transactions 95 (CONF-890609) (1989).

[59] P. Chen, D. Cleland, S. Lovatt, M. Bassett, An empirical model for predicting air infiltration into refrigerated stores through doors, International Journal of Refrigeration 25 (6) (2002) 799–812.

[60] T. Lafaye de Micheaux, M. Ducoulombier, J. Moureh, V. Sartre, J. Bonjour, Experimental and numerical investigation of the infiltration heat load during the opening of a refrigerated truck body, International Journal of Refrigeration 54 (2015) 170–189.

[61] C. Tso, S. Yu, H. Poh, P. Jolly, Experimental study on the heat and mass transfer characteristics in a refrigerated truck, International Journal of Refrigeration 25 (3) (2002) 340–350.

[62] F. Clavier, V. Sartre, J. Bonjour, Infiltration heat load through the doorway of a refrigerated truck protected with an air curtain, in: Proceedings of the 23th International Congress of Refrigeration, Prague, 2011.

[63] J. Moureh, S. Tapsoba, E. Derens, D. Flick, Air velocity characteristics within vented pallets loaded in a refrigerated vehicle with and without air ducts, International Journal of Refrigeration 32 (2) (2009) 220–234.

[64] J. Moureh, M. Tapsoba, D. Flick, Airflow in a slot-ventilated enclosure partially filled with porous boxes: Part II – measurements and simulations within porous boxes, Computers & Fluids 38 (2) (2009) 206–220.

[65] A. Rai, J. Sun, S. Tassou, Numerical investigation of the protective mechanisms of air curtain in a refrigerated truck during door openings, Energy Procedia 161 (2019) 216–223.

[66] A. Rai, J. Sun, S. Tassou, Three-dimensional investigation on the positioning of air curtain on its effectiveness in refrigerated vehicles used for food distribution, Energy Procedia 161 (2019) 224–231.

[67] S. Getahun, A. Ambaw, M. Delele, C. Meyer, U. Opara, Analysis of airflow and heat transfer inside fruit packed refrigerated shipping container: Part I – model development and validation, Journal of Food Engineering 203 (2017) 58–68.

[68] P. Torres Jara, J. Aguirre Rivera, C. Buenano Merino, V. E., G. Abad Farfán, Thermal behavior of a refrigerated vehicle: Process simulation, International Journal of Refrigeration 100 (2019) 124–130.

[69] D. Gray, A. Giorgini, The validity of the Boussinesq approximation for liquids and gases, International Journal of Heat and Mass Transfer 19 (5) (1976) 545–551.

Thèse accessible à l'adresse : https://theses.insa-lyon.fr/publication/2024ISAL0034/these.pdf © [J. Jeong], [2024], INSA Lyon, tous droits réservés

[70] F. Menter, Two-equation eddy-viscosity turbulence models for engineering applications, AIAA Journal 32 (8) (1994) 1598–1605.

[71] M. Hoang, P. Verboven, J. De Baerdemaeker, B. Nicolai, Analysis of the air flow in a cold store by means of computational fluid dynamics, International Journal of Refrigeration 23 (2000) 127–140.

[72] A. Foster, M. Swain, R. Barrett, P. D'Agaro, S. James, Effectiveness and optimum jet velocity for a plane jet air curtain used to restrict cold room infiltration, International Journal of Refrigeration 29 (5) (2006) 692–699.

[73] F. Hayes, W. Stoecker, Design data for air curtains, ASHRAE Transactions 75 (2) (1969) 168–180.

[74] J. Paquette, S. Mercier, B. Marcos, S. Morasse, Modeling the thermal performance of a multilayer box for the transportation of perishable food, Food and Bioproducts Processing 105 (2017) 77–85.

[75] V. Nascimento Jr, F. Loyola, C. Hermes, A study of frost build-up on parallel plate channels, Experimental Thermal and Fluid Science 60 (2015) 328–336.

[76] C.-H. Cheng, K.-H. Wu, Observations of early-stage frost formation on a cold plate in atmospheric air flow, Journal of Heat Transfer 125 (1) (2003) 95–102.

[77] C. Hermes, R. Piucco, J. Barbosa Jr, C. Melo, A study of frost growth and densification on flat surfaces, Experimental Thermal and Fluid Science 33 (2) (2009) 371–379.

[78] W. Wang, Q. Guo, W. Lu, Y. Feng, W. Na, A generalized simple model for predicting frost growth on cold flat plate, International Journal of Refrigeration 35 (2) (2012) 475–486.

[79] C. Wen, Y. Yu, A generalized method for predicting the minimum fluidization velocity, AIChE Journal 12 (3) (1966) 610–612.

[80] W. Ranz, W. Marshall, Evaporation from droplets, Chemical Engineering Progress 48 (3) (1952) 141–146.

[81] J. Jeong, S. Poncet, B. Michel, J. Bonjour, Eulerian-eulerian multiphase frost model based on phase change driving force, in: 7th IIR International Conference on Sustainability and the Cold Chain, Newcastle, 2022.

[82] B. Kamkari, H. Shokouhmand, Experimental investigation of phase change material melting in rectangular enclosures with horizontal partial fins, International Journal of Heat and Mass Transfer 78 (2014) 839–851.

[83] M. Rahal, Effet de revêtements glaciophobes bioinspirés sur la formation du givre sur une plaque froide, Master's thesis, Université de Sherbrooke (2022).

[84] G. Li, Y. Hwang, R. Radermacher, H. Chun, Review of cold storage materials for subzero applications, Energy 51 (2013) 1–17.

Thèse accessible à l'adresse : https://theses.insa-lyon.fr/publication/2024ISAL0034/these.pdf © [J. Jeong], [2024], INSA Lyon, tous droits réservés

[85] J. Jeong, A. Benchikh Le Hocine, S. Croquer, S. Poncet, B. Michel, J. Bonjour, Numerical analysis of the thermoaeraulic behavior of air during the opening of the door of a refrigerated truck trailer equipped with cold plates, Applied Thermal Engineering 206 (2022) 118057.

[86] M. Ben Taher, T. Kousksou, Y. Zeraouli, M. Ahachad, M. Mahdaoui, Thermal performance investigation of door opening and closing processes in a refrigerated truck equipped with different phase change materials, Journal of Energy Storage 42 (2021) 103097.

Thèse accessible à l'adresse : https://theses.insa-lyon.fr/publication/2024ISAL0034/these.pdf © [J. Jeong], [2024], INSA Lyon, tous droits réservés

Thèse accessible à l'adresse : https://theses.insa-lyon.fr/publication/2024ISAL0034/these.pdf © [J. Jeong], [2024], INSA Lyon, tous droits réservés

FOLIO ADMINISTRATIF

THESE DE L'INSA LYON, MEMBRE DE L'UNIVERSITE DE LYON

NOM : JEONG DATE de SOUTENANCE : 24/04/2024

Prénoms : JIHYUK

TITRE : Modélisation CFD du transfert de chaleur et de masse dans une remorque de camion réfrigérée équipée de plaques eutectiques

NATURE : Doctorat Numéro d'ordre : 2024ISAL0034

Ecole doctorale : Mécanique, Énergétique, Génie Civil, Acoustique

Spécialité :Thermique – Énergétique

RÉSUMÉ :
Le système de refroidissement par plaques eutectiques (matériau à changement de phase, MCP) est une possible alternative aux systèmes conventionnels de réfrigération alimentés par des combustibles fossiles pour le transport de produits alimentaires surgelés ou réfrigérés dans des remorques de camions. Des modèles numériques ont été développés pour évaluer sa faisabilité et ont été validés avec succès par rapport à des résultats numériques et expérimentaux issus de la littérature.

Initialement, un modèle d'infiltration d'air dans la remorque a été développé utilisant un modèle de turbulence $k-\omega$ SST pour prédire le comportement thermoaéraulique de l'air pendant les périodes d'ouverture des portes. Différentes configurations des plaques eutectiques et des ventilateurs ont été analysées. Sans cargaison, les plaques disposées en série le long du plafond de la remorque ont montré un temps de renouvellement plus élevé que celles disposées en parallèle à l'arrière, en raison des zones de recirculation. Cependant, une fois la cargaison introduite, les deux configurations offrent des performances similaires car les zones de recirculation n'ont pas pu se former.

Par ailleurs, un modèle multiphasique granulaire eulérien-eulérien a été développé pour prédire la formation et la croissance du givre sur les plaques eutectiques. Le modèle de turbulence $k-\omega$ SST a été intégré pour étendre l'applicabilité du modèle de givre à une gamme plus large de vitesses d'air. Un modèle de solidification et de fusion a également été implémenté et couplé aux modèles précédents. Avec ce modèle combiné, les performances d'un système eutectique ont été étudiées pour des conditions estivales typiques à Montréal, Canada. Environ 2.3 % du MCP change effectivement de phase au cours des 120 premières secondes. Globalement, le système eutectique offre une alternative viable au système conventionnel, bénéficiant des mécanismes de prévention des infiltrations ou de dégivrage.

Mots-clés : Réfrigération, Matériaux à changement de phase, Transfert de chaleur et de masse, Dynamique des fluides numérique.

Laboratoire (s) de recherche : CETHIL – INSA Lyon
LMFTEUS – Université de Sherbrooke (Cotutelle)

Directeur de thèse:
BONJOUR, Jocelyn, Professeur des Universités, INSA Lyon, Directeur de thèse
PONCET, Sébastien, Professeur, Université de Sherbrooke, Co-directeur de thèse

Président de jury : FOURNAISON, Laurence

Composition du jury :
SAFDARI SHADLOO, Mostafa, Maître de Conférences HDR, INSA Rouen, Rapporteur
GOSSELIN, Louis, Professeur, Université Laval (Québec), Rapporteur
FERTEL, Camille, Docteure, Tecnea Canada, Examinatrice
FOURNAISON, Laurence, Directrice de Recherche, INRAE, Examinatrice
MICHEL, Benoît, Maître de Conférences, INSA Lyon, Examinateur
BONJOUR, Jocelyn, Professeur des Universités, INSA Lyon, Directeur de thèse
PONCET, Sébastien, Professeur, Université de Sherbrooke, Co-directeur de thèse

Thèse accessible à l'adresse : https://theses.insa-lyon.fr/publication/2024ISAL0034/these.pdf © [J. Jeong], [2024], INSA Lyon, tous droits réservés